CORA Cork Open Research Archive
Cartlann Taighde Oscailte Chorcaí

Title	Pyramidal quantum dots: single and entangled photon sources and correlation studies
Authors	Juska, Gediminas
Publication date	2013
Original Citation	Juska, G. 2013. Pyramidal quantum dots: single and entangled photon sources and correlation studies. PhD Thesis, University College Cork.
Type of publication	Doctoral thesis
Rights	© 2013, Gediminas Juska. - http://creativecommons.org/licenses/by-nc-nd/3.0/
Download date	2026-11-17 04:56:40
Item downloaded from	https://hdl.handle.net/10468/1389

UCC
University College Cork, Ireland
Coláiste na hOllscoile Corcaigh

PYRAMIDAL QUANTUM DOTS: SINGLE AND ENTANGLED PHOTON SOURCES AND CORRELATION STUDIES

BY

GEDIMINAS JUSKA

A THESIS SUBMITTED TO
THE NATIONAL UNIVERSITY OF IRELAND, CORK
FOR THE DEGREE OF

DOCTOR OF PHILOSOPHY

EPITAXY AND PHYSICS OF NANOSTRUCTURES GROUP
TYNDALL NATIONAL INSTITUTE, DEPARTMENT OF PHYSICS
NATIONAL UNIVERSITY OF IRELAND, CORK
IRELAND



OCTOBER 2013
RESEARCH SUPERVISOR: Dr. EMANUELE PELUCCHI
HEAD OF THE DEPARTMENT: PROF. JOHN McINERNEY

Contents

1 Introduction 1
1.1 Entanglement and entangled particles in general 1
1.2 Application of entangled photons 2
1.3 Sources of entangled photons 3
1.3.1 Nonlinear optical processes 3
1.3.2 Post-selective production of polarization-entangled photons 4
1.3.3 Single atoms 5
1.3.4 Quantum dots 6
1.4 QD - an artificial atom conception 6
1.4.1 Excitonic complexes 7
1.4.2 Single photon emission 8
1.4.3 The fine structure of exciton 8
1.5 Realisation of entangled photons with QDs 11
1.6 Problems and challenges arising 12
1.7 The main QD systems 14
1.7.1 Self-assembled QDs 15
1.7.2 Site-controlled QDs 16
2 Samples, sample preparation and experimental techniques 20
2.1 Substrate preparation 20
2.2 MOVPE 21
2.3 Growth of pyramidal QDs 22
2.3.1 Self-limiting profile 22
2.3.2 Epitaxial layers 23
2.4 Post-growth processing 24
2.4.1 Surface-etching 24
2.4.2 Back-etching 25
2.5 The basic micro-PL set-up, fine-structure splitting measurement 27
2.6 Time-correlated single photon counting set-up 28
2.6.1 Lifetime measurements 29
2.6.2 Photon correlation measurements 30
2.7 Magneto-photoluminescence set-up 31
3 Optical and structural properties of pyramidal recess heterostructures 34
3.1 Heterostructures in pyramidal recesses 34
3.2 Basic characterisation of excitonic complexes 36

3.2.1 Excitation power dependence 36
3.2.2 Photoluminescence lifetime 38
3.2.3 Linewidth 39
3.3 Dependence on the confinement barrier material 40
3.4 Dependence on alloy composition 41
3.5 Biexciton binding energy 42
3.6 QD size effect 44
3.7 The effect of a QD layer exposure to U-DMHy 45
3.8 Growth temperature study 46
3.9 Lateral QD states 50
3.9.1 Characterization by polarization anisotropy 51
3.9.2 LQD indication by FSS measurements 53
3.9.3 Speculation on the origin of LQDs 57
3.10 Summary 57
4 Single and correlated photon emission 61
4.1 Pulsed and continuous-wave modes 61
4.2 Correlations under continuous-wave excitation 62
4.3 Modelling correlation curves 65
4.4 Pulsed excitation mode 67
4.5 Visibility of the biexciton-exciton cascade bunching 69
4.6 Quantum dot feeding 70
4.7 Probing multiexcitonic transitions 73
4.8 Summary 83
5 Polarization-entangled photons 85
5.1 Showing polarization-entanglement 85
5.2 Influence of the FSS 86
5.3 Selection of QDs 88
5.4 Indication of polarization-entanglement 90
5.4.1 Polarization-resolved second-order correlation functions 92
5.4.2 Linear polarization correlations 93
5.5 Quantum-state tomography 94
5.6 Fidelity 98
5.7 High density of emitters 99
5.8 Entangled photon emitters grown at different conditions. 100
5.9 Summary 103
6 Magneto-photoluminescence 105

6.1 Nanostructures in the magnetic field 105
6.2 Probing lateral quantum dots 107
6.3 Probing central QDs 110
6.4 Summary 114

Declaration

This dissertation is the result of work carried out in the Epitaxy and Physics of Nanostructures Group at Tyndall National Institute from October 2009 to September 2013.

Except where otherwise stated this dissertation is the result of my own work and is not substantially the same as any I have already submitted, or that I am in the process of submitting, for any degree either at University College Cork or elsewhere.

Gediminas Juska,
Tyndall National Institute,
University College of Cork,
October 2013

Publications

Publications and proceedings

1. **G. Juska**, V. Dimastrodonato, L.O. Mereni, A. Gocalinska, and E. Pelucchi, *Towards quantum-dot arrays of entangled photon emitters*, Nature Photon. 7, 527 (2013).
2. D. Dufåker, K. F. Karlsson, L. O. Mereni, V. Dimastrodonato, **G. Juska**, E. Pelucchi, and P. O. Holtz, *Quantum dot asymmetry and the nature of excited hole states probed by the doubly positively charged exciton* X^{2+}, Phys. Rev. B 88, 045321 (2013).
3. D. Dufåker, K. F. Karlsson, L. O. Mereni, V. Dimastrodonato, **G. Juska**, E. Pelucchi, and P. O. Holtz, *Evidence of nonadiabatic exciton-phonon interaction probed by second-order LO-phonon replicas of single quantum dots*, Phys. Rev. B 87, 085317 (2013).
4. E. Pelucchi, V. Dimastrodonato, L. O. Mereni, **G. Juska**, and A. Gocalinska, *Semiconductor nanostructures engineering: Pyramidal quantum dots* , Current Opinion in Solid State and Materials Science 16, 45 (2012).
5. **G. Juska**, V. Dimastrodonato, L. O. Mereni, A. Gocalinska and E. Pelucchi, *Developing an Array of Site-Controlled Pyramidal Quantum Dots Emitting Polarization-Entangled Photons*, accepted by AIP Conf. Proc., 2012.
6. **G. Juska**, V. Dimastrodonato, L. O. Mereni, A. Gocalinska and E. Pelucchi, *Tuning the Optical Properties of Dilute Nitride Site Controlled Quantum Dots*, accepted by AIP Conf. Proc., 2012.
7. L.O. Mereni, O. Marquardt, **G. Juska**, V. Dimastrodonato, E.P. O'Reilly, and E. Pelucchi E, *Fine-structure splitting in large-pitch pyramidal quantum dots*, Phys. Rev. B 85, 155453 (2012).
8. **G. Juska**, V. Dimastrodonato, L.O. Mereni, and E. Pelucchi, *Nitrogen Incorporation Effects On Site Controlled Quantum Dots*, AIP Conf. Proc. 1399, 407 (2011).
9. **G. Juska**, V. Dimastrodonato, L.O. Mereni, A. Gocalinska, and E. Pelucchi, *A study of nitrogen incorporation in pyramidal site-controlled quantum dots,* Nanoscale Research Letters 6, 567 (2011).
10. E. Pelucchi, V. Dimastrodonato, L.O. Mereni, **G. Juska** and A. Gocalinska, *Semiconductor nanostructures engineering: Pyramidal Quantum Dots*, Curr. Opin. Solid State Mater. Sci. (2011), doi:10.1016/j.cossms.2011.09.002.
11. Gocalinska, K. Gradkowski, V. Dimastrodonato, L.O. Mereni, **G. Juska**, G. Huyet, and E. Pelucchi, *Wettability and "petal effect" of GaAs native oxides*, J. Appl. Phys. 110, 034319 (2011) .
12. D. Dufåker, L.O. Mereni, K.F. Karlsson, V. Dimastrodonato, **G.Juska**, P.O. Holtz and E. Pelucchi, *Exciton -phonon coupling in single quantum dots with different barriers*, Appl. Phys. Lett. 98, 251911 (2011).

13. L.O. Mereni, V. Dimastrodonato, **G. Juska**, and E. Pelucchi, *Physical properties of highly uniform InGaAs Pyramidal Quantum Dots with GaAs barriers: fine structure splitting in pre-patterned substrates,* Superlattices and Microstructures 49, 279 (2011).
14. V. Dimastrodonato, L.O. Mereni, **G. Juska**, and E. Pelucchi, *Impact of Nitrogen incorporation on the excitonic properties of site-controlled, pseudomorphic InGaAsN QDs grown by MetalOrganic Vapour Phase Epitaxy,* Appl. Phys. Lett 97, 072115 (2010).
15. **G. Juska**, V. Dimastrodonato, T. H. Chung, A. Gocalinska and E. Pelucchi, *Entangled photon emission from (111)B site-controlled Pyramidal quantum dots: the role of the excitonic pattern for pre-selection*, to be submitted Phys. Rev. B
16. **G. Juska**, V. Dimastrodonato, L. O. Mereni, T. H. Chung, A. Gocalinska, E. Pelucchi, B. Van Hattem, M. Ediger, and R. T. Phillips, *Quantum dot nanostructure formation in inverted pyramidal recesses*, to be submitted Phys. Rev. B

Conferences

Oral presentations

1. **G. Juska**, V. Dimastrodonato, T. H. Chung, A. Gocalinska and E. Pelucchi, *Polarization-entangled photons from site controlled pyramidal quantum dots*, CLEO 2013, San Jose, CA, United States, 7/9/13.
2. **G. Juska**, V. Dimastrodonato, L. O. Mereni, T. H. Chung, A. Gocalinska and E. Pelucchi, *Polarization entangled photon emission from site controlled pyramidal quantum dots*, QD Day 2013, Nottingham, UK, 10/1/2013.
3. **G. Juska**, V. Dimastrodonato, L.O. Mereni, A. Gocalinska, and E. Pelucchi, *High density of site-controlled pyramidal quantum dots emitting polarization-entangled photons*, CMD-24, Edinburgh, UK, 6/9/2012.
4. **G. Juska**, V. Dimastrodonato, L.O. Mereni, A. Gocalinska, and E. Pelucchi, *Controlling the properties of dilute nitride site controlled quantum dots*, ESPS-NIS 9th International Workshop, Eindhoven, Holland, 7/5/2012.
5. **G. Juska**, L.O. Mereni, V. Dimastrodonato, A. Gocalinska, and E. Pelucchi, *Variety of excitonic features in pyrmadal site-controlled quantum dots,* Photonics Ireland, Malahide, Dublin, 7/9/2011**.**

Poster presentations

1. **G. Juska**, V. Dimastrodonato, L. Mereni, A. Gocalinska, and E. Pelucchi, *Tuning the Optical Properties of Dilute Nitride Site Controlled Quantum Dots*, ICPS 31, Zurich, Switzerland, 29/7/2012

2. **G. Juska**, V. Dimastrodonato, L.O. Mereni, A. Gocalinska, and E. Pelucchi, *Entangled photons from site-controlled pyramidal quantum dots grown on (111)B oriented GaAs substrate,* QD2012, Santa-Fe, New Mexico, USA, 13/5/2012.
3. **G. Juska**, V. Dimastrodonato, L.O. Mereni, A. Gocalinska, and E. Pelucchi, *Expanding the limits of tuneable properties of pyramidal site-controlled quantum dot system*, QD2012, Santa-Fe, New Mexico, USA, 13/5/2012.
4. **G. Juska**, V. Dimastrodonato, L.O. Mereni, and E. Pelucchi, *Extremely long photoluminescence lifetime in single InGaAs site-controlled quantum dots,* OECS12, Paris, France, 12/9/2011.
5. **G. Juska**, V. Dimastrodonato, L.O. Mereni, and E. Pelucchi, *Long-lived Photoluminescence Dynamics of Single InGaAs Site-Controlled Quantum Dots,* Physics of Light-Matter Coupling in Nanostructures, Berlin, Germany, 06/4/2011.
6. **G. Juska**, V. Dimastrodonato, L.O. Mereni, and E. Pelucchi, *Fine Structure Splitting Reduction and Modification of Excitonic Properties by Nitrogen "Incorporation" in Site-Controlled Quantum Dots*, Physics of Light-Matter Coupling in Nanostructures, Berlin, Germany, 4/4/2011.
7. **G. Juska**, V. Dimastrodonato, L.O. Mereni, and E. Pelucchi, *Modification of the Excitonic Properties by Nitrogen "Incorporation" in Site-Controlled Quantum Dots,* IOP One-Day Quantum Dot Meeting, Bristol, UK, 10/1/2011.

Abstract

Practical realisation of quantum information science is a challenge being addressed by researchers employing various technologies. One of them is based on quantum dots (QD), usually referred to as 'artificial atoms'. Being capable to emit single and polarization-entangled photons, they are attractive as sources of quantum bits (qubits) which can be relatively easily integrated into photonic circuits using conventional semiconductor technologies. However, many challenges related also to the intrinsic properties of QDs still have to be overcome. The main problem of the absolute majority of QD systems is the fine-structure splitting (FSS) – the degeneracy lifting of the exciton level. It compromises entanglement detection which, in general, resides in the polarization of photons emitted in the biexciton recombination cascade through an intermediate exciton level. The origins of the FSS are related to a low carrier confinement potential symmetry (e.g., physical QD elongation, strain, piezoelectric fields, alloy disorder). Particular tuning strategies (magnetic field, electric field, strain), indeed, can rectify this issue, however they complicate the set-up and typically can be applied to a single QD at a time, while an array of symmetrical QDs is needed for complicated quantum information processing tasks.

In this work, site-controlled InGaAs QDs grown on (111)B oriented GaAs substrates pre-patterned with 7.5 μm pitch tetrahedrons were studied. Intrinsically with high rotational symmetry, deterministic control of spatial, structural and spectral properties make this system an attractive option. Most of the published studies of pyramidal QDs were carried out with InGaAs QDs confined by AlGaAs alloy prior this work. Switching to GaAs confinement has some dramatic effects on the structural and the optical properties. They were studied herein in deep detail using conventional micro-photoluminescence, photon correlation spectroscopy and magneto-optical micro-photoluminescence techniques.

Chapter 3 is dedicated to the characterization of general properties: for example, an optical spectrum with a specific order of excitonic transitions (namely a biexciton being at higher energy than an exciton) is shown as a characteristic property of the system; resolution limited linewidth (<20 μeV) was measured showing very high optical quality. Moreover, the study is expanded to the other

heterostructures which form in the pyramidal recess next to the main QD. The formation of a formerly unidentified type of InGaAs nanostructures (three lateral quantum dots) is found and some previous inaccurate interpretations of the results are corrected. Finally, the composition of the confinement barrier material (e.g., GaAs) and its growth temperature are shown as ones of the key parameters that determine quantum dot properties, such as the nontrivial emission energy dependence, the excitonic pattern and the photoluminescence energetic ordering of the InGaAs ensemble nanostructures.

In Chapter 4, pyramidal QDs are studied by photon correlation spectroscopy. Pyramidal QDs are shown as single photon sources. By using experimentally obtained second-order correlation functions and three-level system rate equations describing QD population, charge carrier dynamics is probed and the study of a non-trivial QD feeding mechanism is presented. Finally, a particular excitonic pattern relevant to entangled photon emitters is studied and a possible recombination scenario is proposed.

Chapter 5 shows pyramidal QDs as polarization-entangled photon emitters – for the first time in site-controlled QD systems. A particular attention is dedicated to QDs exposed to unsymmetrical dimethylhydrazine (UDMHy), a precursor of nitrogen atoms, during the growth. These QDs showed the best results in the distribution of fidelity values of the maximally entangled state and high density of good emitters. The measured density of ~15% of entangled photon emitters in some sample areas is a huge improvement comparing to the other state-of-the-art QD systems. Moreover, entanglement was measured from QDs unexposed to UDMHy, as well. Finally, an important correlation between the excitonic pattern and entangled photon emitters is found – a reliable criterion for the pre-selection of entangled photon emitters with the success probability as high as 0.75.

In Chapter 6, magneto-optical properties are studied using a set-up of Cambridge Cavendish Laboratory which enables probing an optical response to a magnetic field which crosses the sample at arbitrary angles and, in principle, allows reconstructing the excitonic wavefunctions. In the first part, the presence of lateral QDs is confirmed by this method. In the second part, highly symmetric QDs emitting

entangled photons are studied. Unusual, however theoretically expected response to the magnetic field is observed and discussed.

Chapter 1

1 Introduction

1.1 Entanglement and entangled particles in general

Quantum entanglement is the phenomenon which links the properties of two or more particles which are generated or interact in such a way that they cannot be described individually anymore: they exist as an inseparable system with a single wavefunction. Measurement of an entangled property of a single particle alters the wavefunction and the state of the rest constituent particles, and instantly becomes determined disregarding the physical separation between them ('spooky action at a distance' in Einstein's words). Such correlations are stronger than the ones allowed by local and realistic theories[1].

One of the simplest examples of entangled states are the Bell states:

$$\begin{aligned} \left|\psi^{\pm}\right\rangle &= \tfrac{1}{\sqrt{2}}\left(\left|0\right\rangle_A\left|1\right\rangle_B \pm \left|1\right\rangle_A\left|0\right\rangle_B\right) \\ \left|\Phi^{\pm}\right\rangle &= \tfrac{1}{\sqrt{2}}\left(\left|0\right\rangle_A\left|0\right\rangle_B \pm \left|1\right\rangle_A\left|1\right\rangle_B\right), \end{aligned} \tag{1.1}$$

where $\left|0\right\rangle_A, \left|1\right\rangle_A$ and $\left|0\right\rangle_B, \left|1\right\rangle_B$ are orthogonal bases (e.g., spin orientation, polarization) of the two two-level systems (qubits) A and B. If the state of either single qubit is measured, the outcome is perfectly random: there is a probability of a half to be in the state $\left|0\right\rangle$ or $\left|1\right\rangle$. However, the measurement of the state of either qubit immediately determines the state of the remaining one.

Such states can be created as a consequence of the indistinguishability of identical quantum particles. Identical particles are inherently indistinguishable at the space point where their wavefunctions strongly overlap, as there is no way to track each particle by its trajectory or other intrinsic properties. The states of such particles are treated by the symmetrization postulate[2]. The individual states can only be arbitrary labeled for the mathematical description and, according to the postulate, the states of the systems composed of identical particles are only either symmetric or antisymmetric under the permutations of particle labels. For example, the states $\left|\varphi\right\rangle$ and $\left|\chi\right\rangle$ are treated in the following way:

$$\left|\psi_{1,2}\right\rangle = \tfrac{1}{\sqrt{2}}\left(\left|\varphi\right\rangle_1\left|\chi\right\rangle_2 + \alpha\left|\chi\right\rangle_1\left|\varphi\right\rangle_2\right), \tag{1.2}$$

where $\alpha = +1$ for bosons and $\alpha = -1$ for fermions. Practically this gives a rise to some important quantum mechanical phenomena, such as Pauli Exclusion principle (electrons (fermions) 1 and 2 cannot be in the same state, as $\left|\psi_{1,2}\right\rangle = 0$ would not make sense). Moreover, the observed bunching of two indistinguishable photons (bosons)[3] and antibunching of two indistinguishable electrons (fermions)[4] after colliding on a 50:50 beamsplitter can be explained by the symmetrization arguments and they are often the didactic examples while introducing particle entanglement.

Polarization-entangled photons and their generation is the subject of this work. Photons can encode information as two-level systems by their orthogonal polarization states. They are an attractive choice for various practical application schemes in quantum information science, as they can be used to transfer information or a quantum state over long distances due to the weak interaction with environment and a single qubit can be relatively easily manipulated with linear optics elements.

1.2 Application of entangled photons

Among the most prominent fields of polarization-entangled photon application there are quantum communication and quantum computing. The most mature example of quantum communication is quantum key distribution (QKD). QKD enables secure communication between two parties by encoding the information with a randomly generated key. The weakest point, the initial distribution of a key over the public network between the parties, is irrelevant in QKD, as any attempt to gain knowledge of a key by a third party in the middle is easily disclosed: the measurement of a state alters the wavefunction and it causes anomalies at the final receiving site. While many QKD protocols (BB84 and its modifications) based on a photon polarization state rely on single photon sources (strongly attenuated laser pulses) some realistic proposals (Ekert-91 (Ref. 5), BBM92 (Ref. 6)) based on two-photon polarization-entanglement are on the table. The basic idea is to distribute a pair of maximally entangled photons to both parties and measure entanglement quality to rule out the eavesdropping.

The vision of quantum computation can be realised with a completely different type of computer – a quantum computer[7]. Unlike in classical information processing

schemes, information is encoded in quantum states. The device should enable a certain type of tasks to be performed significantly faster and more efficiently. Among the tasks there are Shor's algorithm[8] for factorizing large numbers, Grover's algorithm[9] for faster searching large lists and others. The realisation of a quantum computer is still in its infancy, with different routes suggested. However, a large number of entangled qubit sources on a single chip will be required most likely. Here, polarization-entangled photons as qubits are a reasonable option.

1.3 Sources of entangled photons

1.3.1 Nonlinear optical processes

The vast majority of experiments and practical applications that require polarization entangled photons rely on nonlinear optical processes. Typically entangled photon pairs are generated via a spontaneous parametric down conversion (SPDC) process in a nonlinear optical crystal with a second order nonlinearity $\chi^{(2)}$(Ref. 10), or less frequently via a spontaneous four-wave-mixing (SFWM) process which uses a third-order nonlinearity $\chi^{(3)}$(Ref. 11). While various schemes exist to exploit the SPDC process, the general idea is to convert a pump photon to two photons (signal and idler) which under appropriate detection conditions are entangled. In one of the first schemes, shown in Figure 1.3-1, a type-II SPSC process (signal and idler photons are of orthogonal linear polarizations H and V) is utilised to generate polarization-entangled photons. Both photons are emitted along the conical surfaces which cross with each other along the two directions: A and B. The energy and momentum conservation law applies for signal and idler, thus if one is detected along A, the other along B and *vice versa*. Due to this indistinguishability, the photons are polarization-entangled:

$$\left|\psi\right\rangle = \tfrac{1}{\sqrt{2}}\left(\left|H_A V_B\right\rangle + e^{i\theta}\left|V_A H_B\right\rangle\right). \tag{1.3}$$

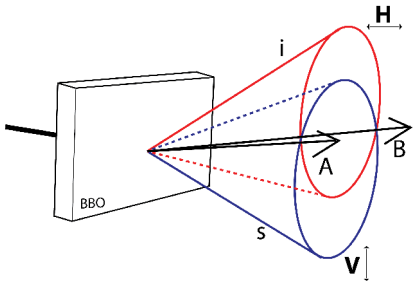


Figure 1.3-1. One of the possible schemes to generate polarization-entangled photons via a spontaneous parametric down conversion process.

1.3.2 Post-selective production of polarization-entangled photons

Polarization entanglement can be generated using two orthogonally polarized and otherwise quantum mechanically indistinguishable photons which are allowed to collide at a non-polarizing beamsplitter (NPB) [12,13]. Two photons of the polarization states $|H\rangle$ and $|V\rangle$ entering through two different input ports are combined at the same time at NPB with two output ports A and B. When a single photon hits 50:50 NPB, NPB performs a linear transformation that converts an entering photon state to a superposition of transmitted and reflected modes. By using a beamsplitter transformation matrix[14], it can be shown that $|H\rangle$ and $|V\rangle$ are converted to $\frac{1}{\sqrt{2}}\left(|H_A\rangle + i|H_B\rangle\right)$ and $\frac{1}{\sqrt{2}}\left(|V_B\rangle + i|V_A\rangle\right)$, respectively. The state of a composite system of two photons then can be expressed as a tensor product:

$$\begin{aligned} |\psi\rangle &= \tfrac{1}{\sqrt{2}}\left(|H_A\rangle + i|H_B\rangle\right) \otimes \tfrac{1}{\sqrt{2}}\left(|V_B\rangle + i|V_A\rangle\right) = \\ &= \tfrac{1}{2}\left(|H_A \otimes V_B\rangle - |V_A \otimes H_B\rangle + i|H_A \otimes V_A\rangle + i|H_B \otimes V_B\rangle\right) = \\ &= \tfrac{1}{2}\left(|H_A V_B\rangle - |V_A H_B\rangle + i|H_A V_A\rangle + i|H_B V_B\rangle\right) \end{aligned} \tag{1.4}$$

The final state is a product state and can be separated to two states of the composing subsystems (photons), thus they are not entangled. However, with an appropriate post-selection procedure it is possible to select detection events that indicate polarization-entangled state. Typically such scheme is realised by selecting photons that only simultaneously are detected at separate output ports A and B. The two-photon polarization state is then:

$$|\psi\rangle = \tfrac{1}{\sqrt{2}}\left(|H_A V_B\rangle - |V_A H_B\rangle\right). \tag{1.5}$$

Such scheme discards half of the detection events, and cannot be employed for true loophole-free nonlocality tests, even though some theoretical proposals[15,16] suggest that loophole-free tests could be performed provided that the source and the detection process are very efficient. However, by accepting quantum nonlocality as a true property of quantum mechanics, the post-selection method can be used to obtain polarization-entanglement.

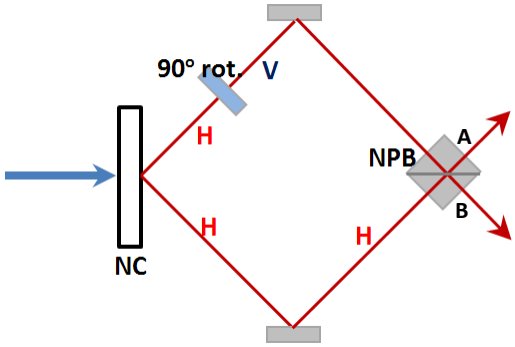


Figure 1.3-2. The scheme of post-selective production of polarization-entangled photons. Spontaneous parametric down conversion process is used to generate two indistinguishable photons.

1.3.3 Single atoms

The first experimental evidence of particle entanglement was obtained with atom sources[17,18,19]. Polarization entanglement was studied using calcium atoms. Initially, a single atom is selectively excited from its ground state $4s^2\ ^1S_0$ (the total angular momentum J=0) to the excited state $4p^2\ ^1S_0$ (J=0). A simple single photon excitation process which is forbidden by the selection rules is overcome by a nonlinear excitation process using two different laser wavelengths (406 nm and 581 nm). The excited state is composed of two electrons present in a *4p* subshell. It is a singlet state, as indicated by the term symbol $^1S_0$, meaning that the same energetic level is populated by two electrons of an opposite spin but otherwise indistinguishable. Particle indistinguishability suggests that the excited two electron state is entangled and, in fact, is the source of polarization-entanglement realized in the following scenario. The excited state $4p^2\ ^1S_0$ cannot directly relax to the ground state $4s^2\ ^1S_0$ by the emission of a single photon as the process is quantum mechanically forbidden (coupling to the photon requires the angular momentum change by ±1). However, the relaxation process can happen through the intermediate

state $4s^1 4p^1\ ^1P_1$ with J=1, by the emission of two sequent photons, constrained to have the total angular momentum equal to zero. If the photons are emitted along the quantization axis *z*, there are two degenerate states with magnetic quantum numbers *m* equal to -1 and +1. The constriction of the total angular momentum of photons emitted in the recombination cascade determines their polarization: the first circularly polarized (either left- or right-hand) photon is followed by a photon of the same polarization, provided that their emission direction is opposite (Figure 1.3-3). Thus in short, the recombination starts from the initial, entangled, two-electron superposition state by the emission of the first photon. The photon and atom remain entangled after this recombination step, and upon the emission of the second photon, entanglement is transferred to the two-photon polarization state:

$$|\psi\rangle = \frac{1}{\sqrt{2}}\left(|R_1 R_2\rangle + |L_1 L_2\rangle\right). \tag{1.6}$$

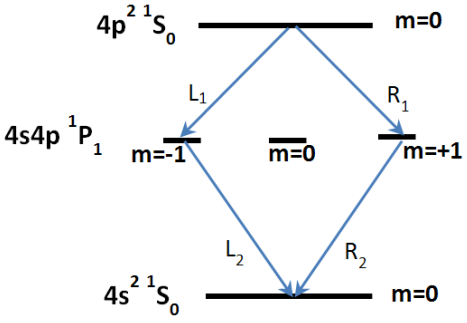


Figure 1.3-3. Polarization-entangled photon emission from a single atom via recombination cascade.

1.3.4 Quantum dots

Quantum dots are usually referred to as artificial atoms due to similarities to the energetic structure of single atoms and their optical phenomena, thus it is not surprising that the fundamental idea[20] of generating polarization-entangled photons with QDs is very similar to the one realized in single atoms. The details of the entangled photon generation scheme, along with a fundamental introduction to QDs are presented in more detail in the following sections.

1.4 QD - an artificial atom conception

An ideal conception of a QD can be realised as a three-dimensional region in the semiconductor material which is confined by a higher bandgap semiconductor.

QDs have an atom-like discrete energetic structure, due to the quantum confinement effect. The separation between energy levels and the number of bound states depend on the size and shape of a QD. Typically QDs are designed with a single or two electron levels in the conduction band and a few hole levels in the valence band.

1.4.1 Excitonic complexes

Holes and electrons injected into a QD from its vicinity or generated directly create a certain excitonic complex. Two factors are responsible for this binding: strong confinement and Coulomb interaction. Two electrons (holes) can occupy each QD energetic level following Pauli Exclusion principle, thus several different types of excitonic complexes can be created in a QD. A combination of a single electron and a hole is a neutral exciton, two electrons and two holes compose a biexciton. The disbalance of the number of opposite charge carriers leads to charging of a QD and to the creation of charged excitonic complexes. For example, two holes and a single electron compose a positively charged exciton (a positive trion). In photoluminescence spectra, different excitonic transitions typically are not degenerate and are separated by a few meV (Figure 1.4-1). This is the consequence of the Coulomb interaction[21]. Thus a single QD has a characteristic pattern of photoluminescence where these transitions can be identified.

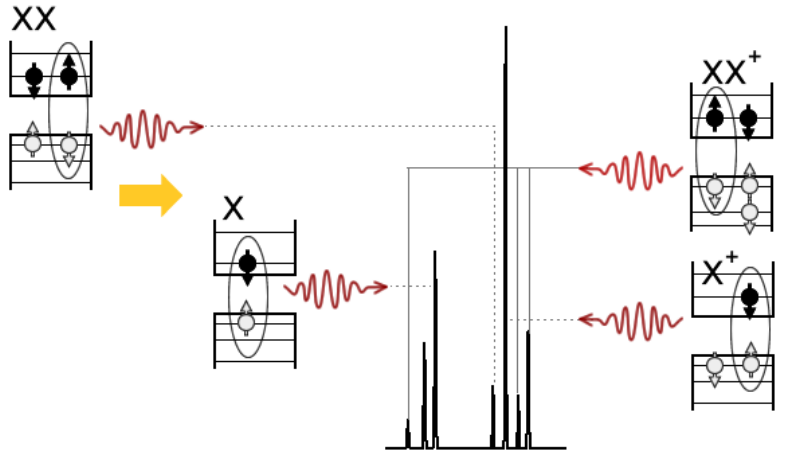


Figure 1.4-1. A few excitonic complexes in QD: exciton, negatively charged exciton, positively charged exciton and biexciton. Each of the transitions has slightly different energy (not obvious from the scheme).

1.4.2 Single photon emission

Light sources can be classified by the photon distribution statistics. A coherent light source (e.g., laser) with a Poissonian distribution of photons is usually considered as a reference point. According to the statistics, there is always a probability to emit two or more photons at a time, no matter how much the Poissonian or super-Poissonian (e.g., thermal light) source is attenuated. A third type of source emits light distributed following the sub-Poissonian distribution. It is a non-classical type of a light source, as single photons are emitted. There are a number of single photon sources: e.g. nitrogen-vacancy center in diamond[22], single molecules[23], single atoms[24]. QDs are atom-like systems and they emit photons in a similar manner[25]. Initially the QD is excited from its ground state and then the relaxation process proceeds through the spontaneous emission of a single photon. The state can be re-excited after a certain delay, thus a true single photon emission is achieved.

1.4.3 The fine structure of exciton

A neutral exciton complex is composed of an electron and a hole. An electron has a spin value of $S = \pm\frac{1}{2}$ $\left(S_z = \pm\frac{1}{2}\right)$, while the total angular momentum of a hole is $J = \pm\frac{3}{2}$ $\left(J_z = \pm\frac{3}{2}\right)$, provided that the separation between heavy- and light-hole levels is of the order of a few meV, which allows neglecting the contribution of light-holes in first approximation[26]. The exchange interaction couples the spin of an electron and the angular momentum of a hole. Thus excitons can be constructed from single-particle bases S, S_z, J and J_z. The consequences of the exchange interaction strongly depend on the symmetry of a QD. Following the theoretical framework developed for nanostructures with the symmetry of D_{2d} (perfectly cylindrical) and lower[27] (the other relevant QD symmetries are shown in Figure 1.4-3), the total angular momentum of an exciton along the quantization axis z is $M = S_z + J_z$. Thus there are four possible spin configurations with M values of +1, -1, +2 and -2. Excitons with $|M| = 1$ can recombine by radiative recombination and they are usually referred to as bright states, while $|M| = 2$ are dark states and the light can be emitted only if a spin flip occurs. If a spin of an electron would not be interacting with the

total angular momentum of a hole, these exciton states would be fourfold degenerate (Figure 1.4-2). However, the exchange interaction lifts the degeneracy between $|M|=1$ and $|M|=2$ states by δ_0. The spin interaction Hamiltonian can be expressed as a 4x4 matrix using the exciton states $|+1\rangle,|-1\rangle,|+2\rangle,|-2\rangle$ as basis:

$$H_{ex}=\frac{1}{2}\begin{pmatrix} +\delta_0 & +\delta_1 & 0 & 0 \\ +\delta_1 & +\delta_0 & 0 & 0 \\ 0 & 0 & -\delta_0 & +\delta_2 \\ 0 & 0 & +\delta_2 & -\delta_0 \end{pmatrix}, \tag{1.7}$$

where $\delta_0=1.5(a_z+2.25b_z)$, $\delta_1=0.75(b_x-b_y)$ and $\delta_2=0.75(b_x+b_y)$, a and b being spin-spin coupling constants. The matrix has a block diagonal form which shows that $|M|=1$ and $|M|=2$ states are not mixed. If the structure is symmetric (D_{2d}), $b_x=b_y$, and $\delta_1=0$ meaning that $|+1\rangle$ and $|-1\rangle$ are the eigenstates of (1.7) and the bright states are twofold degenerate. On the other hand, $\delta_2\neq 0$ meaning that the dark states $|+2\rangle,|-2\rangle$ even initially are mixed as indicated by the presence of off-diagonal elements in the subblock of $|+2\rangle,|-2\rangle$ states. The eigenstates are $\frac{1}{\sqrt{2}}(|+2\rangle\pm|-2\rangle)$ which are separated by δ_2, with the relative energy of $\frac{1}{2}(-\delta_0\pm\delta_2)$. When the symmetry is broken, $b_x\neq b_y$ and $\delta_1\neq 0$ causing an analogous mixing of the bright states: $\frac{1}{\sqrt{2}}(|+1\rangle\pm|-1\rangle)$. The two states are separated by the energy value of δ_1, which is usually referred to as the fine-structure splitting. The states are at the relative energy of $\frac{1}{2}(\delta_0\pm\delta_1)$.

When a QD is completely asymmetric, this picture is no more valid as all the four excitonic states become mixed. They all are partially allowed and are observed in the optical spectrum. For a charged exciton, when two particles of the same kind are at the same (ground) level, a spin singlet state is formed and thus no electron-hole exchange interaction occurs.

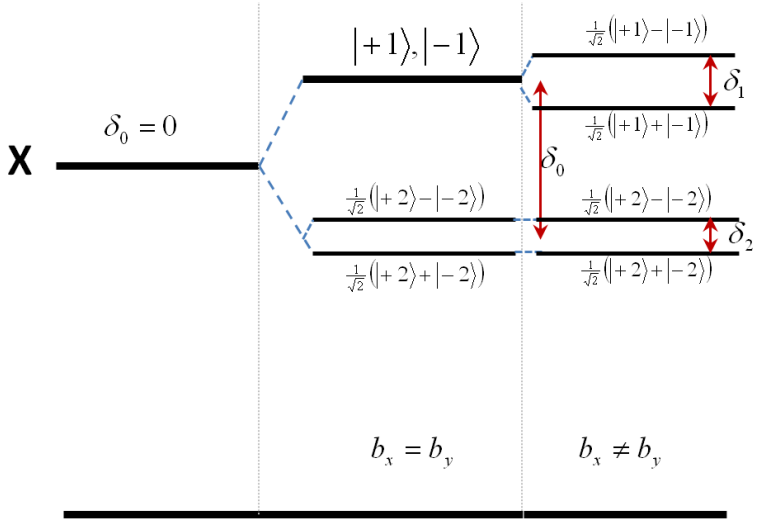


Figure 1.4-2. The exciton fine structure scheme. The central part presents the splitting of exciton level to bright and dark states which are spin degenerate if high rotational symmetry is preserved. The right part shows the fine structure splitting.

The presented simplified picture of an exciton fine-structure is valid for the most QDs studied experimentally, which usually possess low symmetry of C_{2v} (Figure 1.4-3), thus the fine-structure splitting and dark states. However, the spin interaction can be significantly different in structures with other particular symmetries. For example, theoretical calculations based on the group theory predict that QDs with the rotational symmetry of C_{3v}, which is of particular importance in the scope of this work, should not have dark states[28,29]. It rather should be composed of two pairs of bright degenerate states. The lack of the experimental proof of such picture was explained by the fact that all dots present of a D_{3h} symmetry. Some spin-spin interaction peculiarities of C_{3v} symmetry nanostructures have been revealed experimentally with the help of a magnetic field[30,31]. It was shown, that the magnetic field easily mixes hole states $J_z = +\frac{3}{2}$ and $J_z = -\frac{3}{2}$ resulting in significantly different Zeeman interaction when compared to C_{2v} systems.

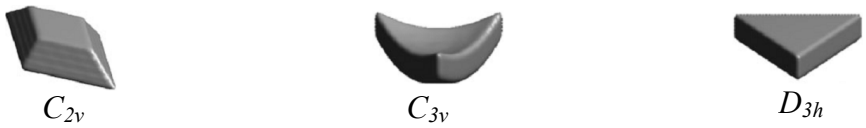


Figure 1.4-3. Possible symmetries of QDs. C_{2v} (C_{3v}) symmetry has a two-fold (three-fold) rotation axis and two (three) vertical mirror planes containing the rotation axis. D_{3h} symmetry has a three-fold rotation axis, 3 two-fold rotation axes perpendicular to the first rotation axis and a horizontal mirror plane. The figure is taken from M. A. Dupertuis et al., Phys. Rev. Lett. 107, 127403 (2011).

1.5 Realisation of entangled photons with QDs

There are a number of ways to obtain entangled photons with quantum dots. All the methods are based on similar ideas previously realised with other types of light sources, which were introduced in section 1.3. The post-selective production of polarization-entangled photons was obtained from QDs with high single photon purity and photon indistinguishability[32]. Moreover, time-bin entanglement was successfully shown using exciton and biexciton transitions[33]. However, the most attractive way to generate entangled photons can be achieved by making use of the biexciton-exciton recombination cascade. While the proposed idea belongs to Benson *et al.*[20], fundamentally it is very similar to the one realised in single atoms. An empty QD is excited to the biexciton state by populating it with two excitons. As discussed, a single exciton has a total angular momentum *z* projection value M=±1. Electrons and holes composing a biexciton are at the corresponding ground states, and they have opposite spins (angular momenta) due to Pauli Exclusion principle. Thus the net spin of the involved electrons and holes is equal to zero and the biexciton state is a single, non-degenerate state. Both excitons composing the mutual complex are of opposite spins and the total angular momentum of the state is equal to zero. Such state cannot recombine directly to the ground state, and like in single atoms, can relax only through the intermediate state by changing the angular momentum value by ±1. The intermediate state is a neutral exciton, with two degenerate states with M=±1, provided that the QD is symmetric. During the recombination to the state with M=-1(+1), a right-(left-)hand circularly polarized photon is emitted. Due to the total angular momentum constriction, further recombination proceeds with the emission of a left-(right-)hand circularly polarized

photon, if both photon emission direction is the same, along the quantization axis. Both possible two-photon polarization states are in the superposition:

$$|\psi\rangle = \frac{1}{\sqrt{2}}\left(|R_{XX}L_X\rangle + |L_{XX}R_X\rangle\right). \tag{1.8}$$

Like in single atoms, the origin of polarization entanglement resides in the initial state electronic configuration. The initial population of a QD with two indistinguishable particles (excitons) leads to the formation of a singlet state. Entanglement is simply transferred from this state to the polarization of two photons during the recombination cascade.

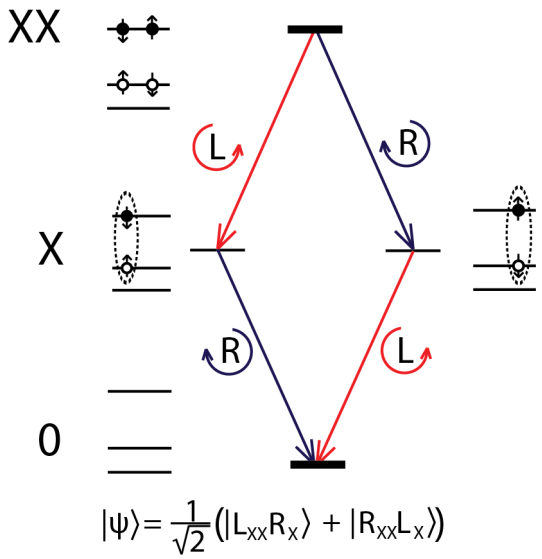


Figure 1.5-1. The recombination cascade in a QD.

1.6 Problems and challenges arising

The presented polarization entanglement realisation scheme is a case which is rarely observed in real quantum dots. Its advantage derives from the degenerate exciton level. However, in the majority of QD systems, the degeneracy of the exciton level is lifted because of the electron-hole exchange interaction, provided that the confinement potential symmetry is low. The symmetry can be reduced due to various reasons such as QD elongation[34,35], strain[36], random alloy segregation[37], etc. In this case, the non-degenerate exciton levels are separated in energy by an amount called the fine-structure splitting (FSS). Both levels are mixed and optical selection rules

valid for linear polarization apply. Thus, in general, a pair of emitted photons is co-linearly polarized. Since the biexciton is a spin singlet state without electron-hole exchange interaction, its level is a single degenerate state[38]. However, its ground state is the exciton, thus the FSS is reflected in both transitions (see Figure 1.6-1).

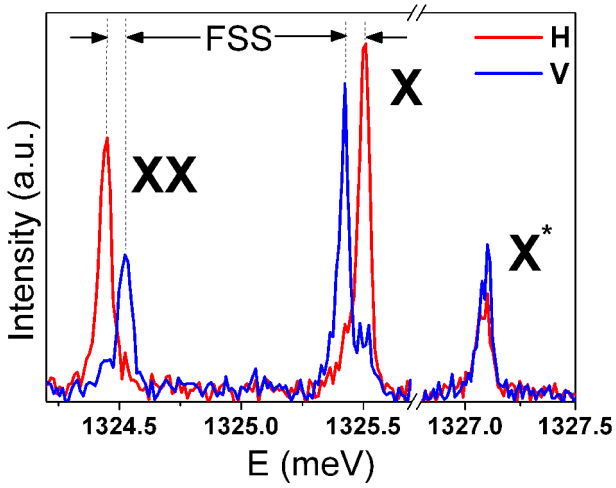


Figure 1.6-1. The fine-structure splitting observed in the spectrum of a QD by filtering the linear photon polarization.

A few points need to be addressed regarding the biexciton-exciton recombination scheme when a FSS is present. Similarly as in an ideal case without FSS, a QD is initially populated by two particles (excitons) which create a spin singlet state which then can be detected through the cascaded recombination process itself, which, despite the FSS, maintains the entangled nature of the original state[39]. However, the final entangled two-photon polarization state is modified because of the FSS. Thus the modification of the entangled state happens according the following scenario. Initially a stationary biexciton state is created:

$$|\psi\rangle = \frac{1}{\sqrt{2}}\left(|XX_H \otimes X_H\rangle + |XX_V \otimes X_V\rangle\right) \tag{1.9}$$

Upon spontaneous emission of the biexciton photon of either horizontal (H) or vertical (V) polarization, the state becomes a superposition of two exciton-photon states:

$$|\psi\rangle = \frac{1}{\sqrt{2}}\left(|H_{XX} \otimes X_H\rangle + |V_{XX} \otimes X_V\rangle\right) \tag{1.10}$$

The non-degenerate exciton states are at different energy and thus evolving at different pace, resulting in the appearance of an evolving phase term in the state:

$$|\psi\rangle = \frac{1}{\sqrt{2}}\left(|H_{XX} \otimes X_H\rangle + e^{i \cdot FSS \cdot t/\hbar}|V_{XX} \otimes X_V\rangle\right) \tag{1.11}$$

Since the emission of the exciton is spontaneous, the phase term evolves until the exciton photon is emitted, transforming the state to a final two photon state:

$$|\psi\rangle = \frac{1}{\sqrt{2}}\left(|H_{XX} \otimes H_X\rangle + e^{i \cdot FSS \cdot \tau_X / \hbar}|V_{XX} \otimes V_X\rangle\right) \tag{1.12}$$

It is a stationary state with a fixed phase term. However, because of a variable lifetime τ_x of individual excitons, the phase term values differ in the corresponding two-photon polarization states. The issue rising here is that entanglement is evaluated using an ensemble of identically prepared particles. Such situation implies that, in the case of non-zero FSS, entanglement is evaluated of an ensemble containing a variety of different states, making an overall state mixed, and thus with degraded or absent entanglement.

The final two photon-polarization state suggests that entanglement can be observed when either the FSS is very small, ideally equal to zero, or photons for entanglement tests are selected with the same τ_x. The latter method, in principle, could be used to prepare various entangled states, such as $\frac{1}{\sqrt{2}}\left(|HH\rangle - |VV\rangle\right)$ or $\frac{1}{\sqrt{2}}\left(|HH\rangle + i|VV\rangle\right)$, however, with the price of reduced source intensity. Thus QDs with vanishing FSS and emitting all photons with maximally entangled state $\frac{1}{\sqrt{2}}\left(|HH\rangle + |VV\rangle\right)$ have an advantage.

A FSS is present in the absolute majority of QDs from various systems. The probability of finding QDs with small enough FSS is very low even in state of the art systems. Tremendous effort was made to overcome this problem by manipulating electronic states with magnetic field[40], annealing[41], electric field[42], strain[43]. However, most of these techniques at the moment are bulky and only a single emitter can be deterministically tuned at a time. Thus, effective local tuning strategies or preferentially 'good' entangled photon emitters are in demand.

1.7 The main QD systems

QDs are an interesting playground for fundamental studies with greatly expanding vision for practical application. Since QDs have to meet requirements for particular applications, a substantial number of QD fabrication approaches exist. Ideally a single QD system should meet several requirements: (1) high optical quality

(indicated by the lifetime-limited linewidth), (2) precise spatial control (e.g., in waveguides, photonic cavities), (3) high uniformity of QD sizes (emission energy), (4) wavelength tunability, (5) high symmetry properties essential in entangled photon emission, (6) a design which allows electrical control and so on. Most of the QD systems still come with certain trade-offs between their properties. The main epitaxially grown QD systems are introduced in this section.

1.7.1 Self-assembled QDs

In self-assembled growth mode, QDs are formed spontaneously due to a particular specific self-organizing mechanism. Stranski-Krastanov (SK) QDs and QDs grown by droplet epitaxy are the most prominent examples, with SK QD system by far being the most popular. Such QDs typically are nearly defect-free and are of a high optical quality. However, due to a random formation process they lack position, size control and the symmetry of QDs is typically low.

Stranski–Krastanov QD formation is essentially based on the lattice constant mismatch between the QD layer and the substrate[44]. Typically a thin InAs layer (the wetting layer) is grown on (100) oriented GaAs substrate. Above the certain critical thickness (a few monolayers) the two-dimensional growth transfers to a three-dimensional in order to minimise the strain (of the wetting layer). These islands are QDs which then are capped with a thick layer of confining material to isolate the QDs from the atmosphere and to provide the confinement. The QD formation process itself is spontaneous.

Growth of QDs by **droplet epitaxy**[45] is based on a different self-organization mechanism – group III elements (Ga, In or Al), deposited on the substrate at higher temperature than their melting point, segregate to droplets of nanometre-sized dimensions. During the following step, the droplets are exposed to the flux of group V elements and crystallization of the droplets into III-V QDs occurs. Such growth method can be exploited growing strain-free QDs (GaAs/AlGaAs), as well as strained (InAs/GaAs).

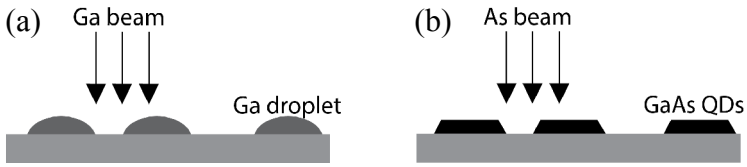


Figure 1.7-1. Fabrication of QDs by droplet epitaxy. (a) Segregation of Ga droplets. (b) Final formation of crystalline QDs.

1.7.2 Site-controlled QDs

A number of site-controlled QD systems has been developed to overcome the issues of self-assembled QDs caused by their random nature. A rapid progress in this field showed that some of these QD systems are highly promising and competitive.

A natural idea to achieve site-control is to force SK **QDs** to grow **on nucleation sites**. In one of the approaches, the GaAs substrate is patterned with shallow (~20 nm) holes with the diameter of ~100 nm[46]. The holes are infilled with GaAs buffer and InAs. When the holes are fully infilled, they act as preferential QD nucleation sites because of the strain difference over the hole area and the adjacent planar area. The strain over the infilled holes is such that the critical amount of InAs is smaller to proceed with QD nucleation. The optical quality of such QDs initially was found to be poor because of the etching induced defects. A substantial improvement has been achieved by overgrowing the first QD layer with a GaAs layer which is thin enough to transfer the strain from the hole sites to its top. This layer reduces defect density and acts a platform for a new site-controlled QD layer[47]. The optical quality of such QDs was high, as indicated by the nearly lifetime-limited linewidth (7 μeV) and photon indistinguishability demonstration. However, the low symmetry issues were not solved.

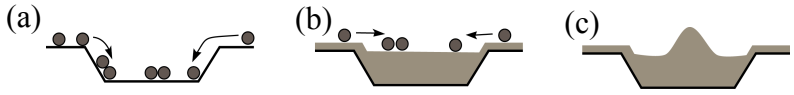


Figure 1.7-2. QDs on nucleation sites. (a) Infilling of the patterned holes. (b) Reduction in critical thickness over the hole site. (c) QD formation.

An alternative way of site-control was achieved by selecting QD growth region with the mask (**selective area grown QDs**[48]). A SiO_2 mask is deposited on (001) GaAs (InP) which is meant to select the wafer areas for the growth (Figure 1.7-3 (a)). Then a relatively thick layer of GaAs (InP) is grown which forms an out-

rising ridge (or pyramid). The top of the ridge is used as a site for SK QD formation (c). It was shown that the template did not affect the optical quality of QDs. By exploiting pyramidal geometry, an electrically driven and tuneable QD light source was designed. However, low symmetry related issues remained unresolved.

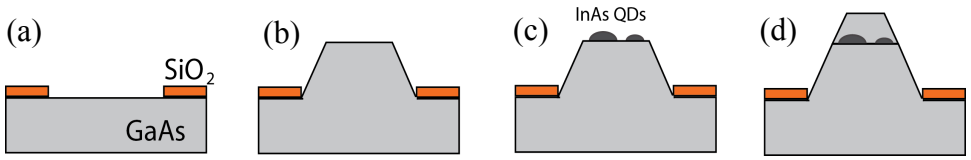


Figure 1.7-3. Selective area grown QDs.

A conceptually different site-controlled QD formation can be achieved by growing **QDs in pyramidal recesses**[49]. These QDs are the subject of this thesis, some growth details and optical properties are discussed hereafter.

Bibliography

[1] J. S. Bell, Physics 1, 3, 195 (1964).

[2] M. L. Messiah and O. W. Greenberg, Physical Review 136, B248 (1964).

[3] C. K. Hong, Z. Y. Ou, and L. Mandel, Phys. Rev. Lett. 59, 2044 (1987).

[4] R. C. Liu, B. Odom, Y. Yamamoto, and S. Tarucha, Nature 391, 263 (1998).

[5] A. K. Ekert, Phys. Rev. Lett.67, 661 (1991).

[6] C. H. Bennett, G. Brassard, and N. D. Mermin, Phys. Rev. Lett. 68, 557 (1992).

[7] E. Knill, R. Laflamme, and G. J. Milburn, Nature 409, 46 (2001).

[8] P. W. Shor, SIAM J. Comput. 26, 1484 (1997).

[9] L. K. Grover, Phys. Rev. Lett. 79, 325 (1997).

[10] P. G. Kwiat, K. Mattle, H. Weinfurter, A. Zeilinger, A. V. Sergienko, and Y. H. Shih, Phys. Rev. Lett. 75, 4337 (1995).

[11] M. Fiorentino, P. L. Voss, J. E. Sharping, and P. Kumar, Photonics Technology Letters, IEEE 14, 983 (2002).

[12] Y. H. Shih and C. O. Alley, Phys. Rev. Lett. 61, 2921 (1988).

[13] Z. Y. Ou and L. Mandel, Phys. Rev. Lett. 61, 50 (1988).

[14] C. H. Holbrow, E. Galvez, and M. E. Parks, American Journal of Physics 70, 260 (2002).

[15] S. Popescu, L. Hardy, and M. Żukowski, Physical Review A 56, R4353 (1997).

[16] P. G. Kwiat, P. H. Eberhard, A. M. Steinberg, and R. Y. Chiao, Physical Review A 49, 3209 (1994).

[17] S. J. Freedman and J. F. Clauser, Phys. Rev. Lett. 28, 938 (1972).

[18] E. S. Fry and R. C. Thompson, Phys. Rev. Lett. 37, 465 (1976).

[19] A. Aspect, P. Grangier, and G. Roger, Phys. Rev. Lett. 47, 460 (1981).

[20] O. Benson, C. Santori, M. Pelton, and Y. Yamamoto, Phys. Rev. Lett. 84, 2513 (2000).

[21] A. Schliwa, M. Winkelnkemper, and D. Bimberg, Phys. Rev. B 79, 075443 (2009).

[22] C. Kurtsiefer, S. Mayer, P. Zarda, and H. Weinfurter, Phys. Rev. Lett. 85, 290 (2000).

[23] F. De Martini, G. Di Giuseppe, and M. Marrocco, Phys. Rev. Lett. 76, 900 (1996).

[24] H. J. Kimble, M. Dagenais, and L. Mandel, Phys. Rev. Lett. 39, 691 (1977).

[25] P. Michler, A. Imamoglu, M. D. Mason, P. J. Carson, G. F. Strouse, and S. K. Buratto, Nature 406, 968 (2000).

[26] H. W. van Kesteren, E. C. Cosman, W. A. J. A. van der Poel, and C. T. Foxon, Phys. Rev. B 41, 5283 (1990).

[27] M. Bayer, et al., Phys. Rev. B 65, 195315 (2002).

[28] K. F. Karlsson, M. A. Dupertuis, D. Y. Oberli, E. Pelucchi, A. Rudra, P. O. Holtz, and E. Kapon, Phys. Rev. B 81, 161307 (2010).

[29] M. A. Dupertuis, K. F. Karlsson, D. Y. Oberli, E. Pelucchi, A. Rudra, P. O. Holtz, and E. Kapon, Phys. Rev. Lett. 107, 127403 (2011).

[30] G. Sallen, et al., Phys. Rev. Lett. 107 (2011).

[31] M. V. Durnev, et al., Phys. Rev. B 87, 085315 (2013).

[32] D. Fattal, K. Inoue, J. Vuckovic, C. Santori, G. S. Solomon, and Y. Yamamoto, Phys. Rev. Lett. 92, 037903 (2004).

[33] T. Huber, G. S. Solomon, and G. Weihs, Time-bin entangled photons from a quantum dot, arXiv:1305.2081v1 (2013).

[34] D. Gammon, E. S. Snow, B. V. Shanabrook, D. S. Katzer, and D. Park, Phys. Rev. Lett. 76, 3005 (1996).

[35] R. M. Stevenson, R. M. Thompson, A. J. Shields, I. Farrer, B. E. Kardynal, D. A. Ritchie, and M. Pepper, Phys. Rev. B 66, 081302 (2002).

[36] R. Seguin, A. Schliwa, S. Rodt, K. Potschke, U. W. Pohl, and D. Bimberg, Phys. Rev. Lett. 95, 257402 (2005).

[37] V. Mlinar and A. Zunger, Phys. Rev. B 79, 115416 (2009).

[38] V. Mlinar and A. Zunger, Phys. Rev. B 80, 205311 (2009).

[39] R. M. Stevenson, A. J. Hudson, A. J. Bennett, R. J. Young, C. A. Nicoll, D. A. Ritchie, and A. J. Shields, Phys. Rev. Lett. 101, 170501 (2008).

[40] R. M. Stevenson, R. J. Young, P. Atkinson, K. Cooper, D. A. Ritchie, and A. J. Shields, Nature 439, 179 (2006).

[41] W. Langbein, P. Borri, U. Woggon, V. Stavarache, D. Reuter, and A. D. Wieck, Phys. Rev. B 69, 161301 (2004).

[42] K. Kowalik, O. Krebs, A. Lemaitre, S. Laurent, P. Senellart, P. Voisin, and J. A. Gaj, Appl. Phys. Lett. 86, 041907 (2005).

[43] R. Trotta, E. Zallo, C. Ortix, P. Atkinson, J. D. Plumhof, J. van den Brink, A. Rastelli, and O. G. Schmidt, Phys. Rev. Lett. 109, 147401 (2012).

[44] D. Leonard, M. Krishnamurthy, C. M. Reaves, S. P. Denbaars, and P. M. Petroff, Appl. Phys. Lett. 63, 3203 (1993).

[45] N. Koguchi, S. Takahashi, and T. Chikyow, J. Cryst. Growth 111, 688 (1991).

[46] P. Atkinson, O. G. Schmidt, S. P. Bremner, and D. A. Ritchie, Comptes Rendus Physique 9, 788 (2008).

[47] K. D. Jöns, P. Atkinson, M. Müller, M. Heldmaier, S. M. Ulrich, O. G. Schmidt, and P. Michler, Nano Letters 13, 126 (2012).

[48] D. Dalacu, et al., Laser Photonics Rev 4, 283 (2010).

[49] A. Hartmann, Y. Ducommun, L. Loubies, K. Leifer, and E. Kapon, Appl. Phys. Lett. 73, 2322 (1998).

Chapter 2

2 Samples, sample preparation and experimental techniques

In this Chapter, preparation and fabrication of pyramidal site-controlled quantum dot samples are described. Moreover, the main experimental techniques used to characterise the QDs are presented.

2.1 Substrate preparation

The initial step while fabricating pyramidal QDs is the substrate preparation. To achieve site control with the precision of a few nanometers, a periodic pattern of ordered inverted pyramidal recesses (tetrahedrons) is created in a number of processing steps shown in Figure 2.1-1.

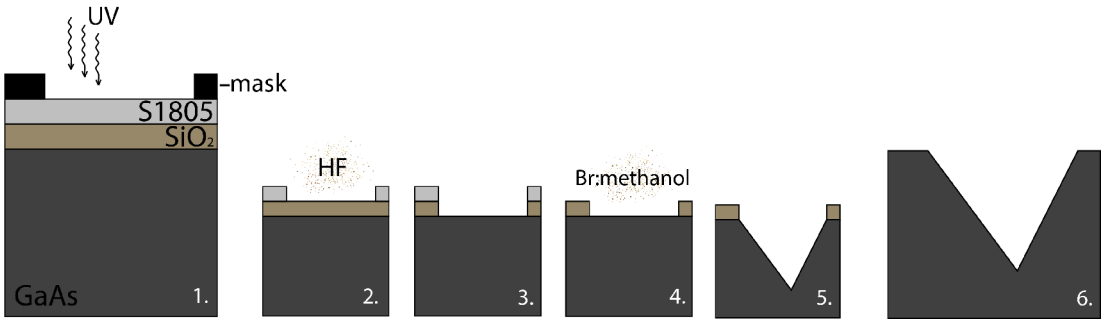


Figure 2.1-1. The processing steps to prepare the substrate with pyramidal recesses.

(1) Initially, a 50 nm thickness SiO_2 layer is sputtered on a (111)B oriented GaAs substrate ((111)B surface is ideally terminated by arsenic atoms as shown in a zinc blende unit cell in Figure 2.1-2(b)). A positive photoresist (S1805) is then spun on the wafer (its adhesion is improved by a thin layer of primer HMDS spun directly on the silicon dioxide). After soft baking at 115°C, the structure is ready for photolithography. The pattern of pyramids is transferred through a chromium mask under exposure to a Hg lamp. The photoresist is developed in a MF-319 developer. (2) A pattern from the photoresist layer is then transferred to SiO_2 using a buffered HF solution. (3)The remaining photoresist is removed in acetone and isopropyl baths. (4) The remaining SiO_2 is ready to be used as a mask for a further wet chemical etching step, where 1% Br_2:methanol solution is used. (5) Here, the chemical etching

anisotropy of (111)B and (111)A surfaces is exploited, resulting in etched inverted pyramidal recesses with exposed (111)A facets (see Figure 2.1-2(a) for the SEM image). (6) The remaining SiO_2 is removed by the buffered HF solution. The distance between the central points of adjacent pyramids is 7.5 μm, in our case.

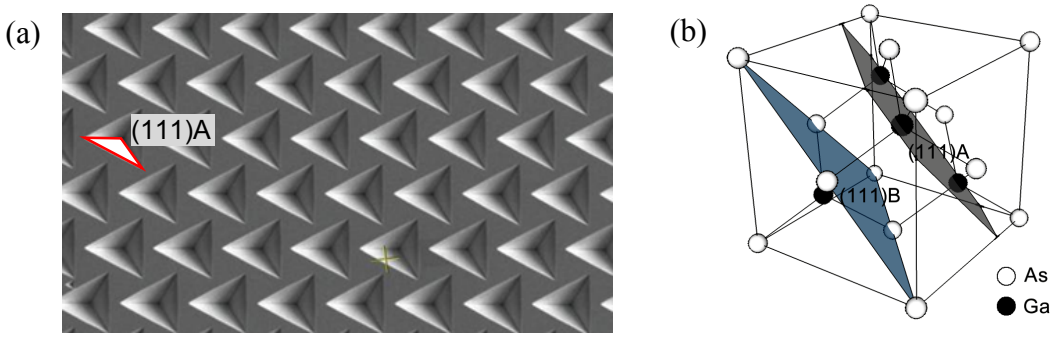


Figure 2.1-2. (a) The SEM top-view image of the substrate pre-patterned with pyramidal recesses. (b) A zinc blende unit cell with the planes (111)A and (111)B identified.

2.2 MOVPE

Metalorganic vapour phase epitaxy (MOVPE) is a technique used to grow thin material layers on a crystalline substrate. Solid films are created through the reactions of gaseous precursors. The precursors are transferred to the reactor by purified carrier gas such as N_2 or H_2, typically under pressure between 20 mbar and 1000 mbar. If III-V group compound semiconductors are grown, the precursors of group III elements are metalorganic compounds (trimethylaluminium, trimethylgallium, trimethylindium) composed of metal (Al, Ga, In) and organic ligands (CH_3), while group V elements are provided from inorganic compounds such as AsH_3, PH_3.

A high flow of N_2 is introduced into the horizontal reactor, also via reactor purge and rotation lines, to assure a laminar flow necessary for a uniform and reproducible deposition of the epitaxial layers. The rotation speed of the satellite (~ 70 rpm) establishes a uniform boundary layer over the substrate, through which the precursors diffuse. The overall MOVPE process is very complex and strongly depends on the interplay between various growth parameters (temperature, the reactor pressure, V/III ratio). While stoichiometrically the formation of, for example,

GaAs can be expressed as $Ga(CH_3)_3 + AsH_3 = GaAs + 3CH_4$, the real formation of a crystalline film involves a complex mechanism of the adsorption and surface migration of the precursor molecules, their decomposition into radicals and remaining adatoms, as well as incorporation, desorption and surface diffusion of the adatoms[1].

The main growth details of the samples studied in this work are presented in Appendix.

2.3 Growth of pyramidal QDs

2.3.1 Self-limiting profile

The epitaxial growth on non-planar substrates involves a more complex growth scenario than on planar ones, as the surface kinetics and chemistry varies significantly on different exposed crystallographic facets. This imbalance is exploited to form site-controlled quantum dots in the pyramidal recesses. The driving phenomenon is the self-limited growth mechanism which is valid for V-grooves[2] and tetrahedron templates[3]. It rises due to two balanced phenomena: (1) anisotropic growth rate on exposed side facets and (2) capillarity effects.

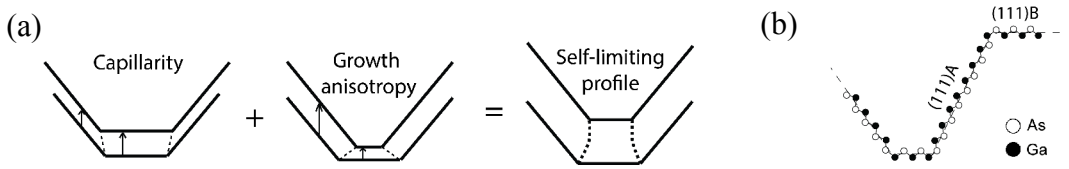


Figure 2.3-1. (a) The self-limiting profile formation under the equilibrium of capillarity and growth anisotropy effects. (b) The atomic arrangement along the cross-sectional profile of an inverted pyramid.

Anisotropic growth rate can be explained if the properties of different surfaces are considered. As mentioned before, the exposed pyramid sidewalls are oriented along (111)A (terminated by Ga atoms). If the structures are grown in the range of growth conditions used in this work, there exists an excess density of precursor decomposition sites on (111)A sidewalls[4]. This leads to a strong decomposition rate anisotropy, and higher growth rate of the crystal on the sidewalls. As the initial

(111)B bottom base of the etched pyramid is only of a few nanometers, the anisotropic growth rate phenomena would maintain it very sharp.

The second, capillarity effect (adatoms diffuse to reduce surface energy by increasing planarity), can be understood if the geometry of a pyramidal recess is taken into account. The released adatoms tend to diffuse to the bottom of a pyramid. If they are released at the distance from the pyramid bottom closer than their diffusion length (a few hundred of nm), they can easily reach the bottom. This mass transfer results in an increased growth rate at the bottom. The phenomenon itself has the tendency to widen the (111)B bottom base of the pyramid.

Both phenomena have opposite tendencies on crystal growth and while present simultaneously, they compete till equilibrium (balance) is reached – so called self-limiting growth. It usually takes a few hundred nanometers of growth to reach this mode. So the final result is a flat base of a few tens of nanometers and oriented along (111)B direction – a site for a QD formation. The self-limiting growth profile width (and thus QD size) can be deterministically controlled by changing growth conditions and materials, such as growth temperature or alloy composition.

2.3.2 Epitaxial layers

To obtain a typical $In_xGa_{1-x}As$ quantum dot confined within GaAs barriers, a stack of epitaxial layers of different functionality is grown. A usual problem and limitation of site-controlled QDs is low photoluminescence quality due to defects introduced close to the vicinity of the dot during the processing and patterning steps. Thus a thick (250 nm) GaAs buffer is grown to reduce the density of defects that could penetrate towards the QD. This layer is topped with a gradually variable $Al_yGa_{1-y}As$ ($y=0.3\rightarrow0.75$) and 90 nm of $Al_{0.75}Ga_{0.25}As$ which is meant to protect the above lying layers from etching with the ammonia solution (NH_4OH) during the post-growth processing. Here, a high etching selectivity ratio between GaAs and $Al_{0.75}Ga_{0.25}As$ is exploited. A pseudomorphic $In_xGa_{1-x}As$ layer is sandwiched between the outer cladding layers of $Al_{0.55}Ga_{0.45}As$ and GaAs. The bottom GaAs layer is of sufficient thickness (100 nm) to develop a self-limiting profile in order to provide a site for a QD formation. The details of the different studied samples are presented in Appendix.

Figure 2.3-2 shows an atomic-force microscopy (AFM) image of side-view of a cleaved pyramidal recess with epitaxial layers grown inside. The weak contrast of the QD is provided due to strain releasing mechanism, while the AlGaAs layers oxidize more than GaAs, resulting in a topographic structure.

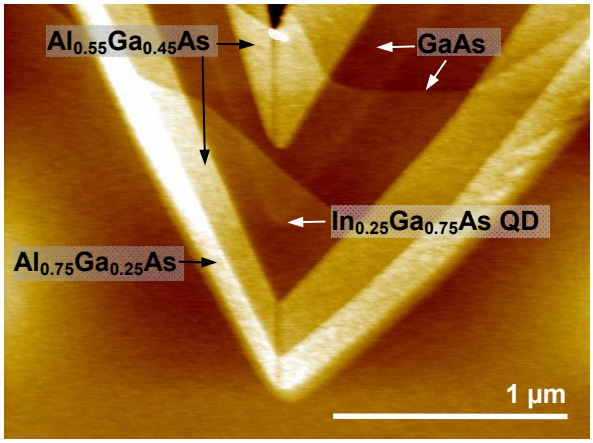


Figure 2.3-2. The AFM image of side-view of a cleaved pyramidal recess with epitaxial layers grown inside.

2.4 Post-growth processing

As-grown samples had to be processed before optical characterisation. There are two post-growth processing procedures: surface etching and back-etching.

2.4.1 Surface-etching

The surface etching is a primary procedure which is meant to improve the quality of the emission spectrum and efficiency. Poor quality of the emission of an as-grown sample is mainly due to irregular structures that form on the surface during the growth near the (111)A facets (Figure 2.4-1(1)). These irregularities might be emitting at the QD emission wavelength and lead to the misinterpretation of results or nearly complete suppression of the dot emission. The purpose of the surface etching is to get rid of the source of faulty emission. Thus the sample is spin coated with a thick layer of the photoresist (2). Then the layer is partially etched away with oxygen plasma until the surface irregularities are uncovered, but a certain amount of photoresist is left in the pyramid (3). The remaining photoresist acts as a QD protection layer during the etching in a sulphuric acid and peroxide solution. The time of etching depends on the quality of the pyramids (planarization, depth of the

recess, etc.) and usually varies from 30 seconds to 3 minutes. Afterwards the sample is thoroughly cleaned in the ultrasound bath of acetone and isopropanol (4).

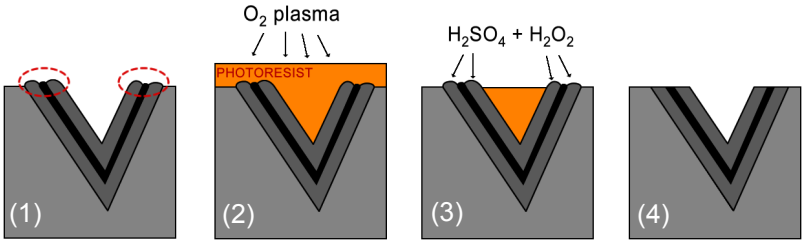


Figure 2.4-1. The steps of the surface-etching procedure.

2.4.2 Back-etching

The advanced processing procedure – back-etching – is primary meant to improve the efficiency of photoluminescence. This is achieved by removing the substrate and placing pyramids in apex-up geometry. In this geometry a pyramid acts as a lens that prevents internal reflections and enhances the extraction of photons. An improvement of up to the three orders of magnitude is observed. The first step in this procedure is preparation of the sample for apex-up orientation. A thin gold and titanium layer is evaporated on the surface of the sample. The functions of this layer are: a mechanical support that keeps pyramids stable, mirror and an electric contact for advanced optoelectronic applications. Then the sample is attached to the support substrate by thermocompression gold-bonding (the steps are shown in Figure 2.4-2). The support substrate is periodically patterned with evaporated gold stripes. It is prepared by a bi-layer lift-off processing. On a preheated and dehydrated support substrate a non-photosensitive layer of LOR10 resist is deposited. It acts as an undercut layer in the lift-off process. Then an imaging resist (UV3) is deposited on the first layer. To promote layer adhesion hexamethyldisilazane (HMDS) is spin-coated before depositing both of the resist layers. A photosensitive layer is exposed to UV radiation through a mask of periodic 1.5 µm stripes. The sample is developed in a MF26 developer. Through the exposed and open areas of the top layer, the underlying layer is dissolved away in a MF319 developer repeating the pattern of the top layer. Since unexposed areas of the imaging resist layer are not developed any longer, prolonged developing results in partially dissolved underlying layer (undercut layer formation). Then the layer of gold is evaporated. Such a bi-layer structure

provides discontinuity in the deposited metal. This structure highly improves the quality of the deposited metallic pattern. The solvent can easily penetrate to the resist and remove it (lift-off). In this way undesirable effects (e.g. retention) are avoided. Finally, the sample is processed in a resist removal solvent 1165 and metalized resist parts are removed. Only the metal layer at the direct contact with the substrate is left. The purpose of patterned support is to provide the escape channels for air from the pyramidal recesses when the sample is kept in vacuum. The absence of such groves can result in the unbinding of the two surfaces.

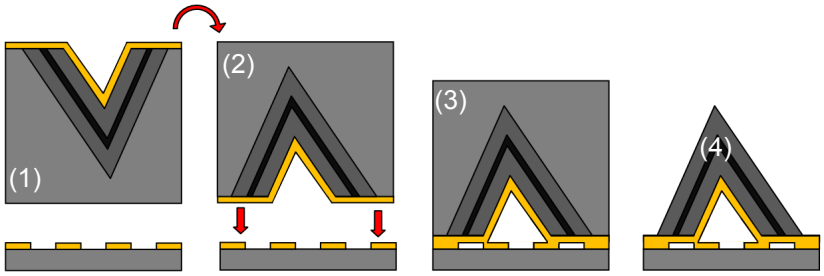


Figure 2.4-2. The back-etching procedure.

The substrate is etched away in hydrogen peroxide and ammonia solution (pH=8.7). When the remaining thickness of the substrate is ~200 µm, the same but less aggressive solution is prepared (pH=8). Etching is kept until the small areas of gold start to appear. Uniformity of etching is achieved in hydrogen peroxide and citric acid solution. The etching rate of $Al_{0.8}Ga_{0.2}As$ layer is much smaller compared to GaAs, thus selectivity and efficient protection of the QD is ensured. The SEM image of back-etched structures is shown in Figure 2.4-3.

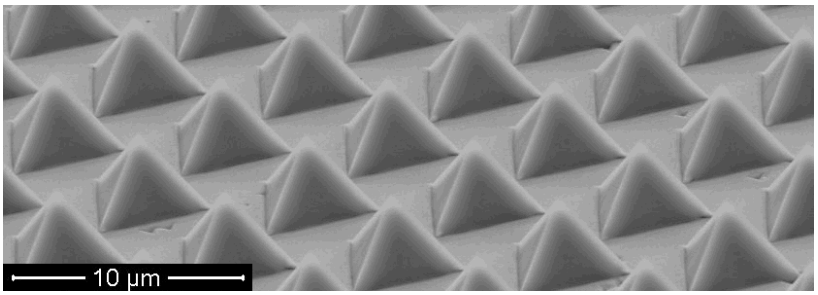


Figure 2.4-3. The HRSEM image of the tilted sample after the substrate removal procedure.

2.5 The basic micro-PL set-up, fine-structure splitting measurement

The optical characterisation of the samples was performed in a standard micro photoluminescence set-up (see Figure 2.5-1) which enables addressing single pyramids. A single objective with a numerical aperture of 0.65 was used to excite the QD and collect its emission in a confocal arrangement. A small working distance of the objective (3.4 mm) enabled high magnification (50x) of the sample surface. For time resolved measurements, a laser diode (PicoQuant LDH-D-C-635M) (λ=635nm) capable to operate in a continuous-wave (*cw*) and pulsed modes (full width at half maximum of 100 ps) was used. The advantage of a *cw* mode is higher intensity of the photoluminescence due to immediate repopulation of the QD after the relaxation. The laser beam was focused on the sample to a spot smaller than the area of a single pyramid (1-2 μm). The typical laser excitation power focused on the sample was a few microwatts (50-200 nW/μm^2). A confocal arrangement was implemented using a pellicle beamsplitter (92/8) which introduced into the optical axis 8% of the initial laser excitation power and transmitted 92% of the emission from a QD. Alternatively a cold mirror was employed for the same purpose. The remaining laser light was filtered by a long-pass filter. A collimated beam of the filtered emission was then focused to the entrance slit of the spectrometer equipped with a charge-coupled device (CCD) or InGaAs detector array. The samples were mounted in a low-vibration, helium closed-cycle cryostat and the temperature values were as low as 7K. A blue LED was used to illuminate the sample for the system aligning and imaging purposes. By placing a beamsplitter in the optical axis, the image of the surface was sent to a video capture device. Such an arrangement enabled a simultaneous live imaging of the surface and detection of the photoluminescence while looking for a possible candidate for the measurement. After finding the position of interest, the beamsplitter could be removed to increase the collection efficiency. The selection of QDs was done by moving the objective in XYZ directions.

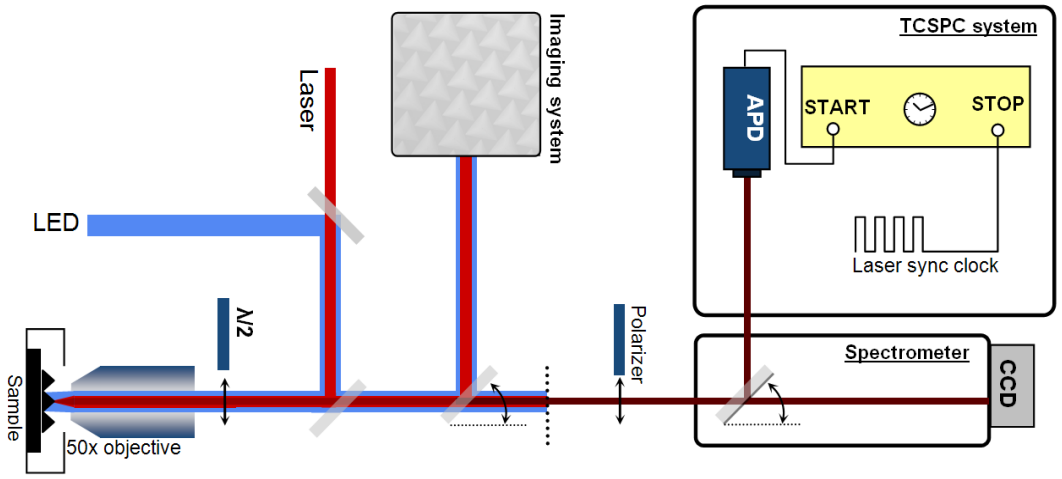


Figure 2.5-1. A micro-photoluminescence set-up combined with a TCSPC system.

High resolution, polarization resolved measurements of the fine structure splitting (FSS) were carried out by placing a half-wave retardation plate and a linear polarizer in the optical axis of the system. The wave-plate was placed just above the objective to avoid polarizing effects especially pronounced in a pellicle beamsplitter. Due to the fine structure splitting, the spectral positions of exciton and biexciton transitions typically follow counterphase sinusoids while changing polarization angle. The value of the FSS can be obtained by subtracting the corresponding biexciton positions from the exciton. Such operation eliminates systematic errors, for example present due to misalignment of the optical axis[5]. The resulting sinusoid amplitude has the value of a FSS. The real spectral resolution of 18 μeV at 870 nm wavelength combined with a peak fitting procedure enabled the total resolution of ~4 μeV in general, and even higher for particular cases (see Chapter 5 for the example).

2.6 Time-correlated single photon counting set-up

Time-correlated single photon counting (TCSPC) is one of the most efficient techniques to analyse photoluminescence kinetics, especially when the light level is very low and high resolution (on the order of picoseconds) is required.

2.6.1 Lifetime measurements

The principle of TCSPC is based on a periodical excitation of a light emitting object and analysing relatively rare single-photon detection events in between the pulses (Figure 2.6-1). Over multiple excitation periods, the profile of intensity decay is built-up. This profile (a photoluminescence decay curve) is nothing more than a histogram composed of time bins (channels) of arbitrary width whose height is determined by the accumulated number of single photon detection events that fit into the corresponding time bin. A photon detection event contains information of the time interval between photon detection and the laser pulse which created it. Thus the electric single-photon detector response and the periodic electric signal synchronised with the optical laser one are fed to a photon counting module and converted to a time value with the precision of picoseconds. The difference between the detection times of the photon and the pulse which created it is used to build the histogram.

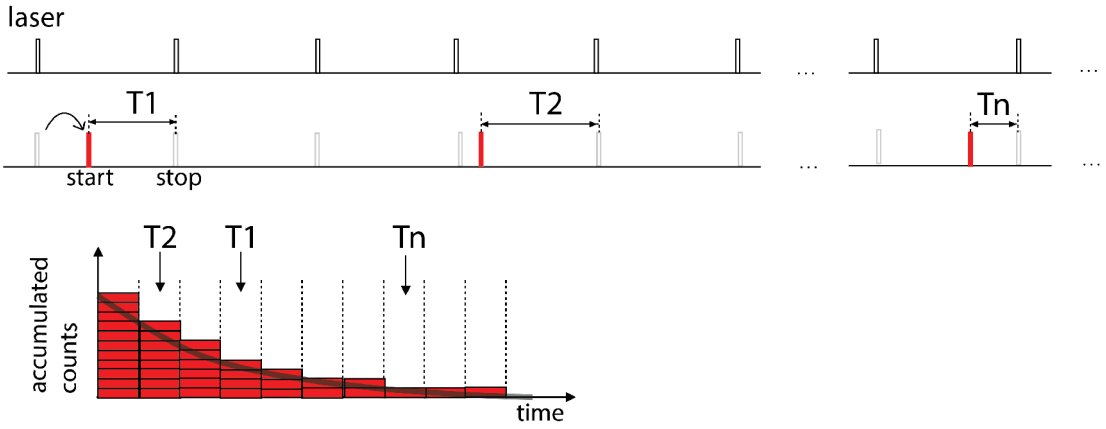


Figure 2.6-1. The principle of TCSPC.

The set-up used in this work is shown in Figure 2.5-1. It is a modified microPL set-up, where light is sent to a monochromator which acts as a tuneable, narrow band-pass filter: the light dispersed by one of the gratings is directed by a lateral mirror towards the side exit slit which selects a desirable wavelength and resolution. The transmitted light was coupled to a multimode fiber attached to an avalanche photodiode (APD) capable of detecting single photons. A TTL signal generated by the APD was fed to a start port of a photon counting module (*SensL HRMTime*) and a train of pulses synchronised with optical laser pulses was fed to the

stop port. The start signal triggers the operation of a time to amplitude converter (TAC) and the stop signal ends it. The analog signal provided by the TAC is converted to a digital one by an anlog to digital converter (ADC) and the obtained values are used to build a histogram of photoluminescence kinetics. The maximum precision (the minimum channel width) was ~27 ps.

2.6.2 Photon correlation measurements

Some correlation measurements were carried out in a classical Hanbury Brown and Twiss (HBT) setup (Figure 2.6-2). A simple auto-correlation curve can be measured by filtering an appropriate excitonic transition with a monochromator, and which is then split by a nonpolarizing 50:50 beamsplitter and detected by two avalanche photo diodes (APD), single photon detectors. One APD starts the photon counting module, the other, delayed, stops it. The histogram constructed from the measured time intervals between the start and stop signals mimics the second order correlation function. Cross-correlations can be measured by splitting photoluminescence with a nonpolarizing 50:50 beamsplitter and directing it to two different monochromators which pass appropriate excitonic transitions of different wavelength. Then, in the same manner as in auto-correlation measurements, the $g^{(2)}(\tau)$ can be measured. If polarization-resolved measurements are required, a polarizer or polarizing beamsplitters can be placed in front of APDs. The set-up is equipped with 4 APDs, thus four curves can be measured simultaneously.

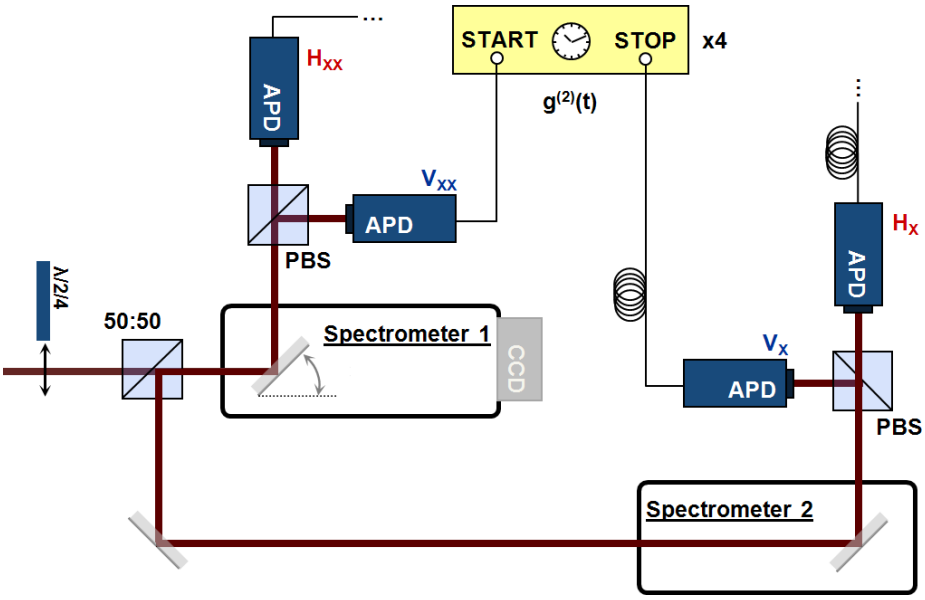


Figure 2.6-2. The set-up for photon correlation measurements.

2.7 Magneto-photoluminescence set-up

Magneto-optical properties were measured in Cambridge Cavendish Laboratory (prof. R .Phillips group) using a magneto-optical confocal setup which enabled probing photoluminescence at arbitrary angles between sample growth direction and magnetic field lines[6]. The sample was placed on four piezoelectric stages which allowed movements in x, y, z directions and rotation around the z axis. The stack of these elements with a short working distance (1.55mm, 0.68 NA) microscope objective coupled to a single-mode fiber were mounted on a stage which enabled tilting the sample in the magnetic field in the range from -10˚ to 100˚. The optical response of a single dot could be studied in this range greatly expanding the functionality of conventional magneto photoluminescence setups. The sample was characterized at 4 K. Continuous-wave He-Ne (633 nm) or Ti:Sapphire (730 nm) lasers were employed as excitation sources.

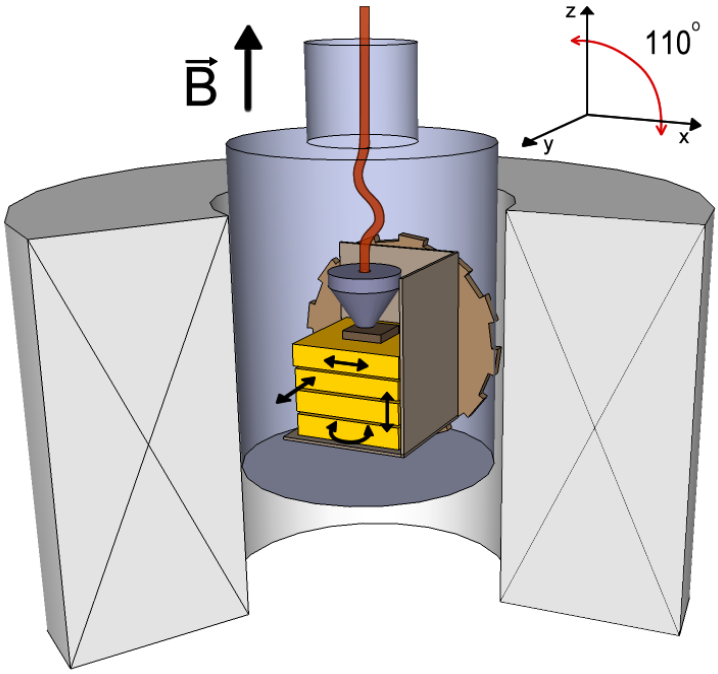


Figure 2.7-1. The set-up to measure magneto-optical properties.

Bibliography

[1] G. Stringfellow, Organometallic Vapor-Phase Epitaxy: Theory and Practice, (1999).

[2] Biasiol and E. Kapon, Phys. Rev. Lett. 81, 2962 (1998).

[3] A. Hartmann, L. Loubies, F. Reinhardt, and E. Kapon, Appl. Phys. Lett. 71, 1314 (1997).

[4] E. Pelucchi, V. Dimastrodonato, A. Rudra, K. Leifer, E. Kapon, L. Bethke, P. A. Zestanakis, and D. D. Vvedensky, Phys. Rev. B 83, 205409 (2011).

[5] R. J. Young, PhD thesis 'Controlling the fine structure splitting in single InAs quantum dots' (2006).

[6] T. Kehoe, M. Ediger, R. T. Phillips, and M. Hopkinson, Rev. Sci. Instr. 81, 013906 (2010).

Chapter 3

3 Optical and structural properties of pyramidal recess heterostructures

The main differences in the optical and structural properties of InGaAs nanostructures confined either by AlGaAs or GaAs and grown in pyramidal recesses are highlighted in this Chapter. The properties of InGaAs structures confined by GaAs (the subject of interest of this work) are shown to be substantially different and they are studied by changing growth parameters: alloy composition, thickness, growth temperature. Moreover, a previously overlooked type of nanostructure (lateral quantum dots) is identified and studied.

3.1 Heterostructures in pyramidal recesses

The first successful growth of site-controlled quantum dots in pyramidal recesses was reported by Hartmann *et al.*[1]. An (In)GaAs QD layer was confined by AlGaAs barriers and for a long time it remained the most widely studied system of such type. It was shown that an ensemble of interconnecting nanostructures develops in the recess (the complex organization of these heterostructures has been broadly studied by atomic-force microscopy, micro-photoluminecence and cathode-luminescence techniques[2]). The sketch of such an ensemble is presented in Figure 3.1-1. If a nominally thin (a few nanometres) pseudomorphically lattice matched InGaAs layer is confined by AlGaAs, a quantum dot is formed at the bottom/centre of the recess. Moreover, the dot is physically connected with three lateral quantum wires (LQWrs) located at the wedges of the adjacent exposed (111)A facets and three lateral quantum wells (LQWs) parallel to the pyramidal recess walls (Figure 3.1-1). If other than a binary alloy is used as barrier material, alloy segregation is produced along the central axis and the three planes perpendicular to the growth direction and extending from the center towards the corners of the pyramid, due to the different surface diffusion constants of the group III adatoms. If the material is AlGaAs, a gallium enriched vertical quantum wire (VQWr) and three vertical quantum wells (VQW) appear.

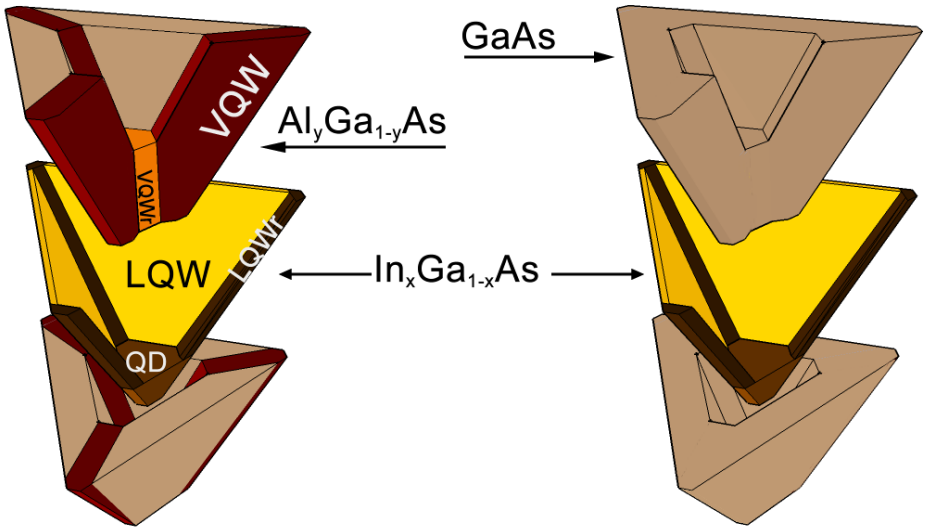


Figure 3.1-1. The schematic spatial configuration of the self-formed nanostructures in two different cases InGaAs layer confinement: (left) AlGaAs and (right) GaAs.

A typical photoluminescence spectrum of the whole InGaAs/AlGaAs ensemble of nanostructures extends from 1.3 eV to 2.05 eV. By this seemingly well-established picture each nanostructure has a unique optical properties signature in the spectrum and they appear ordered on the energy scale. Experimentally it was always observed the QD being at the lowest energy, then typically the emission energy increases following VQWr, LQWrs, LQWs, VQWs and bulk AlGaAs.

On the other hand, using GaAs as a confining barrier instead of AlGaAs has some obvious consequences. First of all, the confining barrier is composed of a uniform material (GaAs), as alloy segregation effects are not present. This implies that the QD is not anymore in direct physical contact with a VQWr and three VQWs. This obviously reduces confinement disorder and also impacts the wavefunctions of the QD charge carriers. Instead, the QD remains connected only to two other types of nanostructures of the same nominal alloy composition of the dot itself: three LQWrs and three LQWs (Figure 3.1-1). Secondly, the emission energies of the InGaAs layer nanostructures are reduced due to lower confinement barrier (see the section 3.3 of this Chapter for more details). Naturally, the photoluminescence energy of these InGaAs structures is expected to be smaller than the GaAs emission and at values determined by confinement effects (real thickness of the structures and real alloy composition, generally speaking expected to be different from the nominal one due

to segregation effects). A representative spectrum of InGaAs nanostructures (the sample *S#2* from the list in Appendix) within GaAs barriers is shown in Figure 3.1-2. All InGaAs nanostructures (a QD, LQWrs and LQWs) are at lower energy than GaAs – 1.512 eV. Emission of a VQWr and VQWs comes from AlGaAs cladding layer which is isolated from InGaAs layer by GaAs.

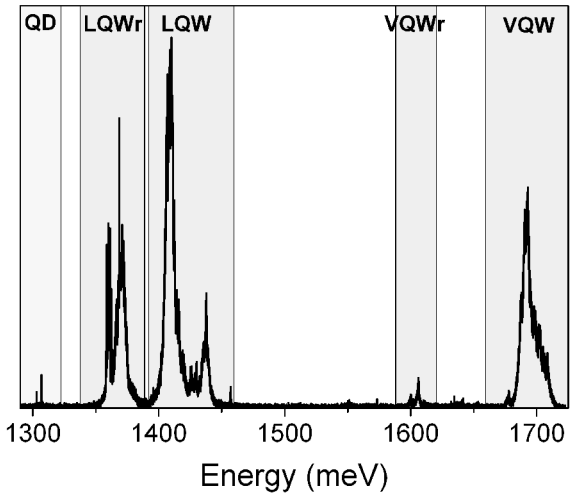


Figure 3.1-2. The PL spectrum of heterostrucures grown in a pyramidal recess taken at 8K. InGaAs nanostructures (QD, LQWr and LQW) are confined by GaAs (not visible PL) barriers and AlGaAs cladding layers which form VQWr and VQW.

3.2 Basic characterisation of excitonic complexes

The main interest of this work was InGaAs QD features (confined by GaAs) present in pyramidal recesses. Their basic, but on the other hand, crucial characterisation was carried out by the methods described in this section.

3.2.1 Excitation power dependence

An important characterisation of a QD can be achieved by excitation power dependence measurements. The set of spectra collected at different laser powers can be used to identify the type of excitonic transitions. At lower excitation powers, the intensity is usually a unique power function of the excitation power. It reflects dynamics of carrier capture and recombination in a QD, which can be described by a random population model[3]. The population of a QD can be approximated to the Poissonian statistics:

$$N_n = \frac{\langle n \rangle^n}{n!} \exp\left(-\langle n \rangle\right), \tag{3.1}$$

where n is the number of electron-hole pairs in a QD, $\langle n \rangle$ is the average population of a QD with e-h pairs over the integration time. The probability of a QD to be populated by a single exciton is then expressed as $N_1 = \langle n \rangle \exp\left(-\langle n \rangle\right)$, while the biexciton probability is $N_2 = \langle n \rangle^2 \exp\left(-\langle n \rangle\right)/2$. It is assumed that $\langle n \rangle$ is linearly proportional to the pump rate (and the excitation power) of carriers to the barriers which feed a QD[3]. Thus the simple Poissonian approximation, in many cases, can be used to describe experimental observations[4].

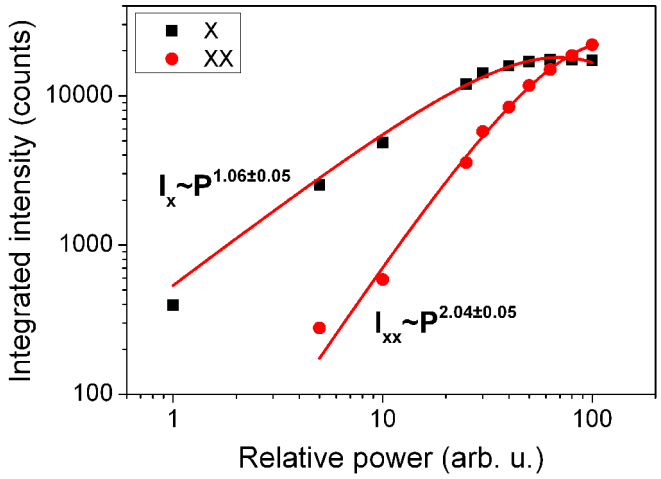


Figure 3.2-1. Representative excitation power dependent intensity of a QD exciton and biexciton transitions. Fittings are on the Poissonian QD population statistics.

Figure 3.2-1 shows an example of exciton and biexciton intensity dependence on the excitation power. As expected by the theoretical assumptions, the exciton intensity increases nearly linearly at low excitation power, while the biexciton intensity follows a quadratic law. Such dependence is used as a preliminary indication of the type of transitions.

While linear and quadratic dependencies of exciton and biexciton hold for the vast majority of QDs reported in literature, this was the case only for a small fraction of pyramidal QDs. Excitation power dependence of the exciton transition nearly always was superlinear, however, the ratio of the power law exponents was maintained equal to ~2 and was used to differentiate one transition from another. The

section 4.6 of Chapter 4 provides a possible explanation of such unusual trend. As pointed out there, due a complex non-linear QD feeding mechanism, $\langle n \rangle$ is not anymore linearly proportional to the excitation power.

3.2.2 Photoluminescence lifetime

An important characteristic of a QD is the PL lifetime. While the knowledge of time resolved properties can be useful identifying multiexcitonic transitions and analysing carrier dynamics, it is important for practical reasons as well: fast recombination of exciton and biexciton complexes means higher operation frequency for the quantum information processing devices. Typically it is assumed and observed that individual multiexcitons decay by a single-exponential law, however, with different lifetime constants. A very simple rule of thumb suggests, that the ratio of exciton and biexciton lifetimes is equal to two ($\tau_X / \tau_{XX} = 2$), as there are two possible recombination channels for the biexciton, comparing to a single one for the exciton. Indeed, this ratio is quite often observed in many QD systems, as well as in a pyramidal QD system. However, the ratio of two assumption does not necessarily hold in all cases – experimental observations and theoretical calculations show that it can vary from 1 to 4, as it strongly depends on the confinement, shape, size of a QD[5,6].

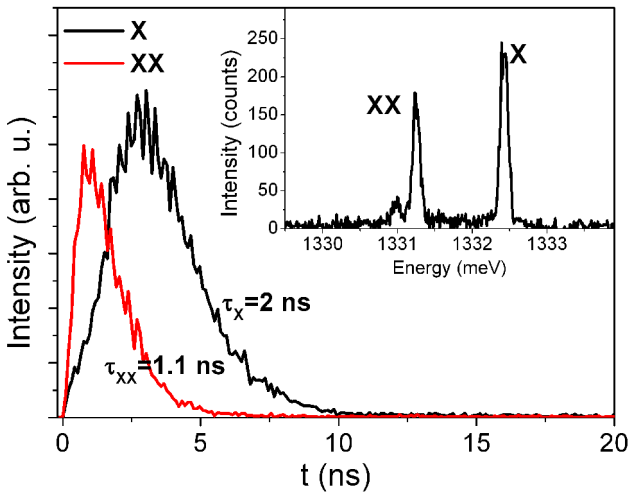


Figure 3.2-2. The PL lifetime traces of exciton and biexciton transitions.

Figure 3.2-2 shows an exciton and a biexciton PL decay traces. Single-exponential decay fits provided lifetime constants of 2 ns and 1.1 ns for the exciton

and biexciton, respectively. The typical exciton lifetime values were found in the range of 1.5 – 2.5 ns. A pronounced long rise time of exciton is consistent with the recombination cascade fact: an exciton can be emitted only after the emission of a biexciton, thus a delay is introduced.

3.2.3 Linewidth

The integration of the emitted photons of a single transition over a period of time shows that the emitted light is not monochromatic. It has a spectral shape characterised by the value of linewidth: a full width at half maximum. There are a number of reasons for the linewidth broadening. Firstly, there is a fundamental limitation, a natural broadening, which is present because of the uncertainty principle. As already discussed, excitonic complexes have a finite lifetime and the energy-time uncertainty is expressed as $\Delta E \Delta t \geq \hbar$. The broadening in energy is then $\Delta E \geq \hbar/\Delta t \approx \hbar/\tau$, where τ is the PL lifetime. The broadening is referred to as Fourier limited, as alternatively it can be obtained by applying a Fourier transform on an exponentially decaying burst of light[7]. The transformation shows that the lineshape of a naturally broadened transition is Lorentzian.

The natural broadening of a transition with τ=1 ns is expected to be ~1 μeV. However, in most cases the measured values of a QD transitions are bigger by one or two order of magnitude. The reason of the excess broadening in QDs is because of the influence of the environment: mainly because of the charge noise and spin noise[8]. Charge noise arises when a QD is excited non-resonantly. Carriers trapped in the vicinity of a QD create random local electric fields which perturb the electronic structure of a QD because of the Stark effect[9]. The homogenous line jumps with the changes in the environment resulting in the linewidth broadening when integrated for longer time. The process is sometimes referred to as spectral diffusion. A recent method of measuring the spectral diffusion timescale[10] suggests that the linewidth wandering can take place in an order of a few nanoseconds even if it is generally considered a slower process (for example, microseconds or milliseconds[11]). The naturally broadened lineshape randomly changes the central position within the spectral diffusion timescale (i.e. the intrinsically narrow emission moves from position to position during the spectral diffusion timescale). The range of the emission energy random shift depends on the environment of a QD (e.g., charged

defect density) and it can be more than two orders of magnitude bigger than the natural linewidth. When integrated longer than the spectral diffusion timescale, the measured lineshape is the superposition of wandering naturally broadened lineshapes. A too short spectral diffusion timescale can be a problem, as various application tasks, with an exception of quantum cryptography, require indistinguishable photons.

The spectral diffusion problem can be overcome by resonant excitation of a QD, which indeed helps to achieve nearly Fourier limited linewidth[12] or producing QDs with high quality, nearly defect-free environment. The typical linewidth of QDs studied in this thesis were 80-120 μeV. Linewidth broadening is especially pronounced in site-controlled QD systems, as patterning introduces defects in the vicinity of a QD, which can act as charge traps. Nevertheless, a significant number of QDs had a linewidth limited by the set-up resolution (18-22 μeV). For example, Figure 3.3-1 shows a QD with a resolution limited linewidth (<22 μeV). It is a very clear indication that linewidth broadening is not a fundamental issue of the site-controlled pyramidal QD system and can be largely overcome only by optimising growth and processing conditions.

3.3 Dependence on the confinement barrier material

Figure 3.3-1 shows two spectra of 0.5 nm nominal thickness $In_{0.25}Ga_{0.75}As$ QDs confined by different barriers – $Al_{0.3}Ga_{0.7}As$ (top) and GaAs (bottom) (the samples *S#1* and *S#3*). The PL of the corresponding InGaAs nanostructures (QD and LQWrs) confined by AlGaAs is at higher energy comparing to the ones confined by GaAs – the blueshift is ~60 meV and ~140 meV of a QD and LQWrs, respectively. On one hand, the result is expected due to higher confinement of $Al_{0.3}Ga_{0.7}As$ barrier (1937 meV vs. 1520 meV at 10 K), however, cannot be explained solely by the solution of a finite potential well problem. The underlying barrier material develops a self-limiting profile which determines the size/shape of a QD. Experimental and theoretical works show that the profile strongly depends on the alloy composition (GaAs can be ~2.5 times larger)[13]. Thus the optical changes are induced by multiple factors.

The most significant modification induced by the confinement barrier was observed in the QD properties (the insets of Figure 3.3-1). QDs confined by AlGaAs have a characteristic energetic order of excitonic transitions – a biexciton was always observed at lower energy (binding) than an exciton. In contrast, QDs of the same nominal properties but confined with GaAs always had a biexciton at higher energy (antibinding) to the respect of an exciton. It is an indication of a very strong perturbation of the QD energetic configuration confirmed by other differences in the overall multiexcitonic energetic order, fine-structure, symmetry, time resolved properties studied in this work.

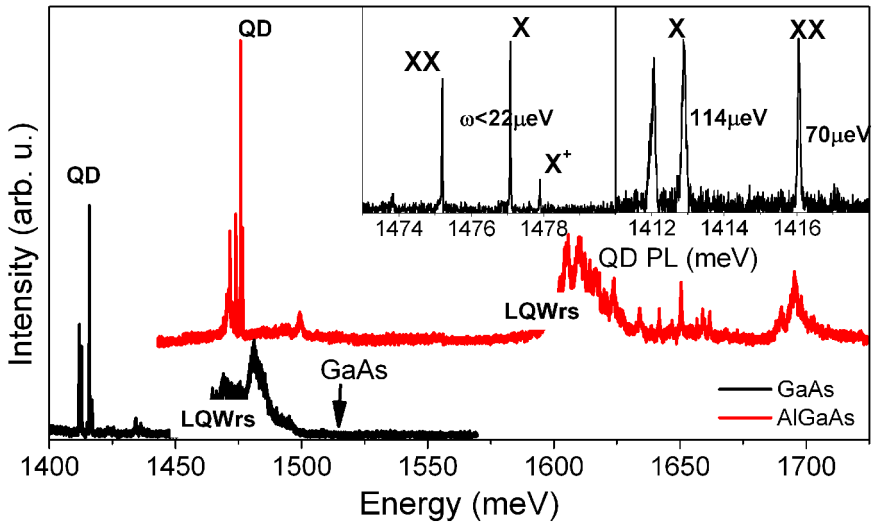


Figure 3.3-1. Comparison of PL spectra of 0.5 nm thickness $In_{0.25}Ga_{0.75}As$ nanostructures grown at identical conditions, but confined within different barriers: GaAs and $Al_{0.3}Ga_{0.7}As$. The spectra are taken at 8K.

3.4 Dependence on alloy composition

The influence of alloy composition is presented in Figure 3.4-1where PL spectra of nominal $In_xGa_{1-x}As$ ($0.15 \leq x \leq 0.65$) nanostructures of 0.5 nm thickness (growth temperature T_g=730˚C) confined by GaAs are shown (the samples *S#(4-9)* listed in Appendix). The bandgap shrinking is directly reflected in the relative emission energy reduction of all InGaAs nanostructures due to an increasing indium concentration. The QD emission is the mostly redshifted as identified by the shaded area in Figure 3.4-1. The emission energy of a QD ground state has been varied in the range of ~230 meV. QD-like emission has still been observed from the structures

with indium concentration of 0.65, however, a detailed analysis showed that the systematic changes in the excitonic pattern (e.g., a biexciton binding energy) have been lost. This is not surprising, as layers of a nominal alloy composition $In_{0.65}Ga_{0.35}As$ grown on GaAs are expected to be highly strained due to the lattice mismatch. At higher concentrations strain in pseudomorphically grown layers is expected to be high enough to become destructive (through defect relaxation).

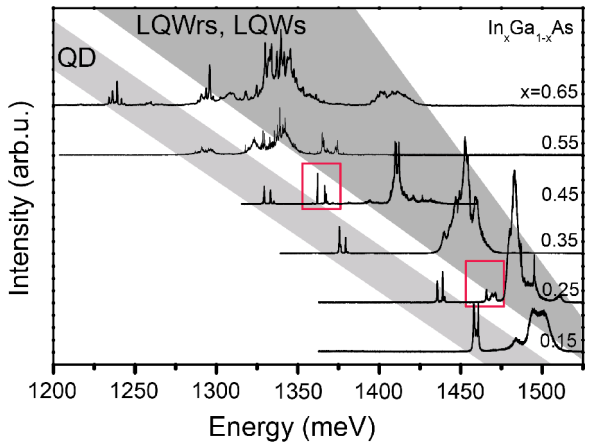


Figure 3.4-1. Photoluminescence of $In_xGa_{1-x}As$ ($0.15 \leq x \leq 0.65$) 0.5 nm nanostructures grown in 7.5 µm pitch pyramidal recesses and confined by GaAs barriers. The red squares highlight additional QD-like peaks which are referred to as lateral QDs as discussed in the text.

3.5 Biexciton binding energy

Up to 55% of indium, a typical QD excitonic pattern exists which acts as a unique signature of this type of nanostructures. A characteristic feature of these dots is an antibinding biexciton (XX) transition (at higher energy than the exciton (X)). QD-like emission was still observed from $In_{0.65}Ga_{0.35}As$ nanostructures, however, the excitonic pattern showed random behaviours from dot to dot.

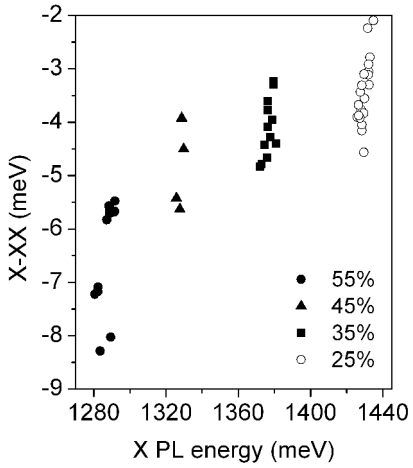


Figure 3.5-1. Biexciton binding energy of individual 0.5 nm thickness QDs of various $In_xGa_{1-x}As$ compositions.

The excitonic pattern can be a very sensitive fingerprint for a specific QD structure (QD size, shape, aspect ratio, alloy composition, etc.)[14]. As already said, it has been observed that a characteristic feature of all presented InGaAs QDs confined by GaAs is an antibinding biexciton (E_x-E_{xx}<0). The result is consistent with a similar pyramidal InGaAs/GaAs QD system[15], however, at variance to Ref. 15 no biexciton with a positive binding energy was observed. Here, the QD confinement barrier clearly plays a significant role, as the pyramidal InGaAs QDs within AlGaAs barriers always had a binding biexciton[16]. Figure 3.5-1 shows XX binding energy distribution in InGaAs QDs of different indium composition. The separation between X and XX is increasing with indium concentration up to -8.3 meV at 55% of indium. While, in general, the behavior of the two-exciton complex can be explained in terms of Coulomb interactions between carriers[17], it appears that here the structural details have a major role. For example, a heavily non-monotonous XX binding energy dependence was observed in a wide range of nominal $In_{0.25}Ga_{0.75}As$ QD thickness (0.45 nm – 1.2 nm) with reduced X and XX separation for largest and smallest QDs (Figure 3.5-2). An advanced theoretical analysis including all the peculiarities of pyramidal QDs is still missing to explain this trend.

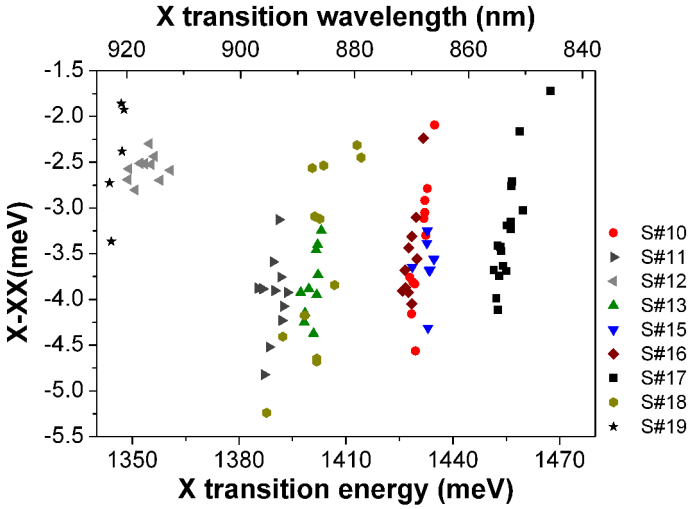


Figure 3.5-2. Biexciton binding energy of $In_{25}Ga_{0.75}As$ QDs as function of exciton emission energy.

3.6 QD size effect

The QD photoluminescence energy can be alternatively controlled by changing the size (thickness) of a QD. Figure 3.6-1 shows average exciton transition energy of $In_{25}Ga_{0.75}As$ ODs of different nominal thickness. By changing the QD thickness from 0.45 nm to 1.2 nm, energy reduction has been achieved in nearly a 100 meV range. A typical standard deviation of the emission energy was found to be 2 – 3 meV. The initial attempts have already been made to reproduce the energy trend by theoretical calculations[18]. Here an important role is played by a large piezoelectric potential across (111) direction which more affects thicker QDs and those with higher indium concentration.

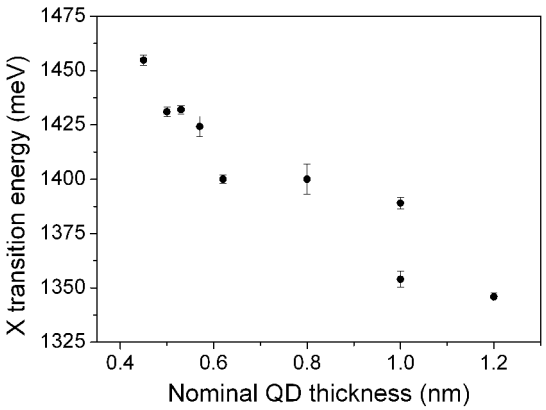


Figure 3.6-1. QD PL energy dependence on the nominal thickness of a QD.

3.7 The effect of a QD layer exposure to U-DMHy

An efficient energy control can be achieved through the growth of dilute nitride alloys[19,20,21]. Incorporation of a small concentration of nitrogen atoms into such host materials as GaAs or InGaAs strongly perturbs their energetic structure so that the band gap shrinks significantly (up to a few hundred of meV). The underlying physics of this perturbation can be quite complicated and is very sensitive to the actual concentration and configuration of nitrogen atoms, however, a good approximation is achieved with the band-anticrossing model. It states that incorporated nitrogen atoms form an isoenergetic defect level in the conduction band because of the large difference in electronegativity and atomic size between N and As. Because of the interaction between the nitrogen defect level and the conduction band, the latter shrinks in energy resulting in the reduction of emission energy.

Such an emission energy control scenario was attempted in pyramidal QDs. An InGaAs QD layer was exposed to unsymmetrical dimethyl hydrazine (U-DMHy) – a standard MOVPE precursor of nitrogen. The typical QD structure and growth conditions (0.5 nm, $In_{0.25}Ga_{0.75}As$, 730°C growth temperature) were selected during the growth. U-DMHy gas flow was exposed simultaneously with the other precursors during the QD layer formation. Figure 3.7-1 shows the summary of the study, where the QD ground state is presented as a function of U-DMHy/AsH_3 ratio. An increase in energy was observed instead of the expected energy reduction. The fact that PL reduction has not been achieved is not very surprising – the conditions of the growth were rather unusual in dilute nitride alloy growth. The temperature of 730°C and low U-DMHy flux are not favourable for nitrogen incorporation, as at high temperature nitrogen atoms tend to be desorbed from the surface[22]. Despite an obvious effect in photoluminescence properties, the role of hydrazine is still not clear. It is possible that it acts as a surfactant[23] which modifies kinetics of the other adatoms and precursors resulting, for example, in reduced growth rate.

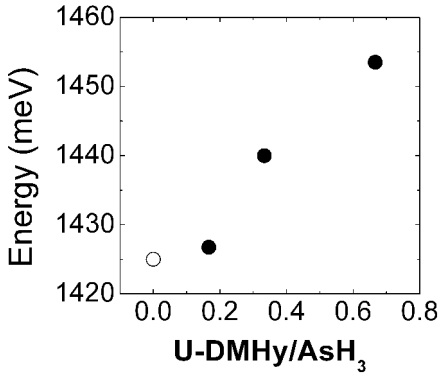


Figure 3.7-1. The effect of the QD emission energy increase due to the exposure to U-DMHy (the samples S#5, S#20, S#21 and S#22).

An important observation from this study has to be stressed as well – the best results in the terms of QD symmetry (as indicated by the detection of polarization-entangled photons) have been achieved from the samples exposed to U-DMHy. It is possible that exposure of a QD layer to U-DMHy is a unique way to improve the small asymmetry of pyramidal QDs.

3.8 Growth temperature study

Growth temperature is one of the key parameters which governs the kinetics of precursors and adatoms that participate in the self-limiting growth in pyramidal (and V-grooved actually) recesses. The complex evolution of self-limiting profiles is well understood and reliably described within a recently proposed theoretical framework[13]. In short, the barrier geometrical profile underlying the QD layer is the one which determines the width of a QD. It is growth temperature and alloy composition dependent, thus it is one of the key parameters which determines the QD properties. The geometrical properties of QDs are directly reflected in the optical ones (e.g., excitonic pattern – which itself can sometimes be used as a fingerprint of a particular geometry). Thus the possibility to tailor them by deterministic control of a QD geometry is not only of a fundamental but of practical interest as well.

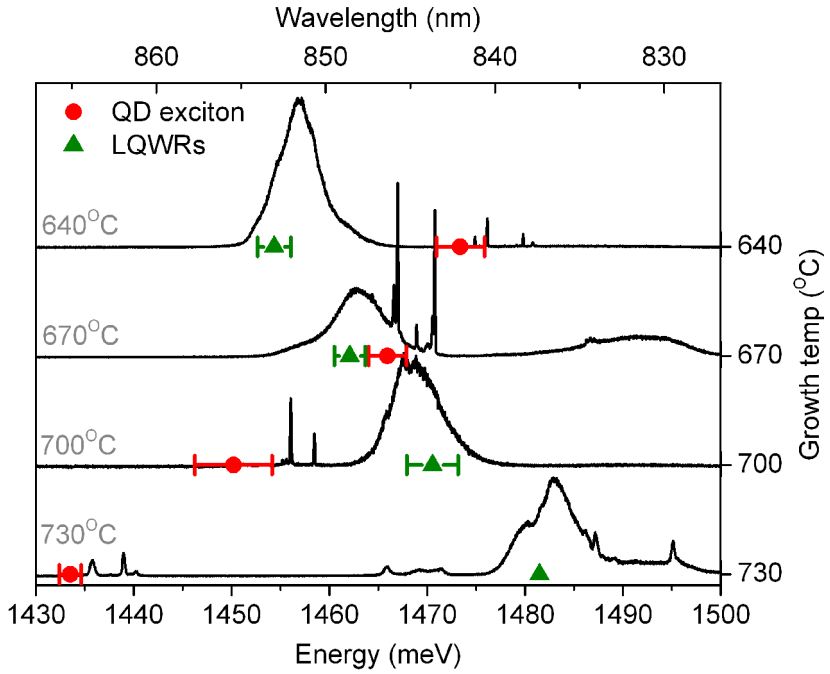


Figure 3.8-1. Photoluminescence energy dependence of QDs and LQWrs on the growth temperature. The structures are formed from 0.5 nm nominal thickness $In_{25}Ga_{0.75}As$ layers.

Figure 3.8-1 summarizes the growth temperature dependence results. The same 0.5 nm nominal thickness $In_{0.25}Ga_{0.75}As$ within GaAs barriers structure was grown at four different temperature values: 640˚C, 670˚C, 700˚C and 730˚C (the samples S#25, S#24, S#23 and S#5, respectively). A clear QD emission energy increase with growth temperature reduction was observed (~40meV comparing PL at 640˚C and 730˚C). The peak attributed to LQWrs followed an opposite trend, crossing with QD emission at structures grown at 670˚C, becoming the mostly redshifted PL feature in the spectra of the structures grown at 640˚C. This observation not only reveals one aspect of the system's complexity, but raises obvious questions if the element of a QD confinement is considered. If the dot is in a direct physical contact with uniform LQWrs at its corners, then the confinement potential should be very complicated or even the structure possibly should not exhibit QD-like properties. However, QD-like emission was always observed from all four samples. This was carefully checked by photon correlation measurements. Moreover, the excitonic pattern with an antibinding biexciton was maintained. And what is more important, polarization resolved correlations proved that all the samples

contain relatively easily found QDs emitting polarization-entangled photons (see the section 5.8 of Chapter 5). It is not only unambiguous indication of a QD as a structure as such, even though not mostly redshifted, but it is a confirmation of the presence of a very similar excitonic pattern and a proof of a high symmetry maintained in the range of studied growth conditions.

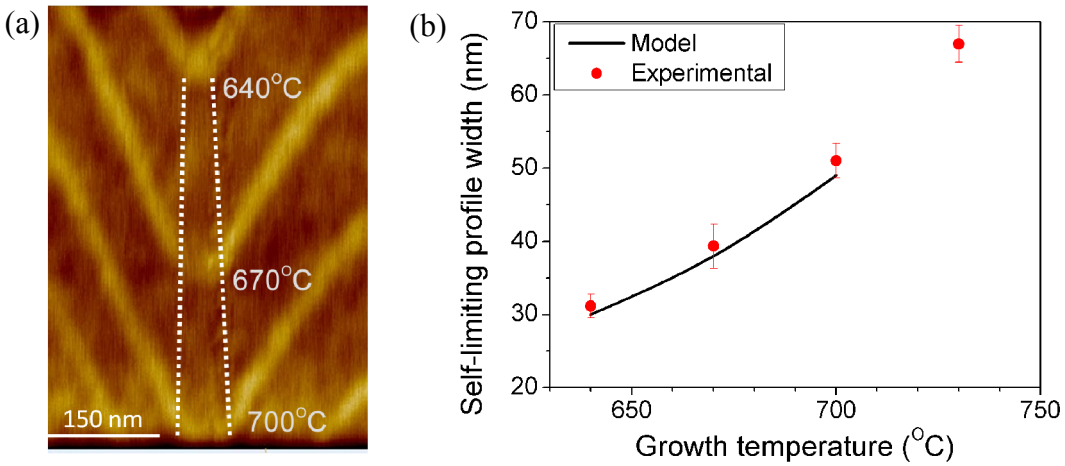


Figure 3.8-2. The AFM study of self-limiting profile evolution at different growth temperature and comparison to the theoretical calculations.

There are several points which should be addressed regarding these observations: (1) the shift trends of QDs and LQWrs and (2) LQWrs becoming the least energetic type of structures at reduced growth temperature values. To verify the influence of growth temperature on the QD morphology, an AFM cross-section image of GaAs (darker regions in Figure 3.8-2(a)) layers grown at the temperature values of 640˚C, 670˚C and 700˚C was taken. GaAs layers were thick enough (100 nm) to develop a self-limited-growth at each corresponding temperature. The width of a GaAs self-limiting profile (or otherwise the lateral QD width determined by the underlying layer) was measured at the interface of GaAs and $Al_{0.3}Ga_{0.7}As$ markers (as indicated in Figure 3.8-2(a)). The width was clearly increasing from ~30 nm at 640˚C to ~70 nm at 730˚C (the latter value was known and already measured previously[24]), as presented in Figure 3.8-2(b). The morphology evolution of such patterned surfaces was expected and thus well understood[13], confirming the accuracy of the modelling results. On the other hand, while the width of a QD decreases more than twice at the lowest temperature, the growth temperature

influence on a QD alloy itself (segregation, exact QD thickness and shape) is not obvious.

Some speculations can be made on these points using growth analysis theory and experimental results based on the AlGaAs alloy. In general, one can expect InGaAs to be analogous in the physics involved. It is well established that in AlGaAs structures enrichment of Ga is present at the central axis of the pyramidal recess due to the more diffusive nature of Ga compared with Al. Similarly, as indium atoms are more diffusive than gallium, segregation of In is also expected and, in fact, this trend was observed in nanowires grown in V-groove shaped patterns[25]. Calculations based on the phenomenological theoretical framework presented in Ref.13 showed no growth temperature dependence of the relative Ga concentration in the AlGaAs alloy along the vertical axis of the pyramid. By assuming a similar scenario for the InGaAs alloy, the influence of the segregation effect (a different alloy composition) on the QD emission energy should be ruled out.

The change of the third QD parameter – its thickness – is still under discussion. However, at this stage it is considered that the change of the growth rate (thickness) at different temperature is not that significant as the self-limiting profile width. By taking into account all three assumptions (self-limiting profile shrinking at lower temperatures, somehow constant alloy composition and roughly the same growth rate for the QD), the QD energy increase at lower temperature can be attributed mostly to the increased confinement associated to a shrinking of the QD size.

The opposite trend in the LQWrs shift can be explained using similar arguments. Within this scenario (the relative Ga concentration in the middle does not change and the volume of the QD is reduced, as the thickness is nearly the same, while the base is smaller at lower temperature) and by invoking the mass conservation (the total flux sent and amount of precursor decomposition are the same), a lower growth temperature would result in an enhanced Ga relative amount/concentration on the lateral facets/LQWRs, not necessarily in a uniform fashion, as the reduced incorporation of group III elements in the QD will be compensated elsewhere. The increased Ga relative concentration could lead to a redshift of the LQWrs emission. In such a scenario, the redshift can be expected only

if Ga segregation effect overtakes the base narrowing effect, which causes the blueshift.

Moreover, to explain the observed relative energetic position of LQWrs and QD grown at 640˚C, the profile of a single LQWr should be considered. It was already shown that in GaAs/AlGaAs pyramidal QD system, the shape of GaAs LQWrs is not uniform along there axes, but tapered towards the center of a pyramid[2]. InGaAs LQWrs are expected to be of an analogous structure. This would imply that the observed LQWrs photoluminescence at lower excitation powers is mainly emitted from regions close to the top corners of a pyramidal recess, while a QD remains confined by a thin part of LQWrs. This would also be consistent with the persistence of a QD confinement, despite the presence of other nanostructures showing lower energy emission.

3.9 Lateral QD states

A further complexity of the pyramidal QD system can be revealed by identifying and demonstrating the existence of a different, previously overlooked, type of structure. In Figure 3.4-1, specific parts of $In_{0.25}Ga_{0.75}As$ and $In_{0.45}Ga_{0.55}As$ spectra are highlighted by open rectangles. These QD-like spectra appear in many pyramidal QD structures in appropriate pumping conditions, and are not accidental to a specific measurement or sample. Moreover, the fact that these relatively sharp QD-like peaks (sometimes as narrow as a few tens of μeV) are not related to excited states of QDs could be immediately ruled out by simple excitation power dependent measurements, as often peaks were appearing before the main QD emission or even were the only ones present when the samples were measured as grown (the absence of the main QD PL is very common in apex-down geometry (or as grown) for InGaAs/GaAs pyramids due to the very poor QD emission extraction). A closer study showed that these peaks had indeed typical QD properties: multiexcitonic transitions could be identified by excitation power dependent and time resolved measurements and the relevant fine-structure splitting measured and characterized. By all means, new QD-like features were found, which are further referred to as lateral QDs (LQDs) due to reasons which will become clearer in the following. To understand more about these QD structures and their relation with the previously

known nanostructures, further analyses were performed. A part of it is presented in Chapter 6, where LQDs were analysed by the magneto-photoluminescence technique. The studied sample was with $In_{0.25}Ga_{0.75}As$ QDs of 0.5 nm nominal thickness, grown at 730˚C (S#3).

3.9.1 Characterization by polarization anisotropy

A rarely used but efficient way to characterize a QD is to probe its emission from the cleaved side[26,27]. Pyramidal QDs are favourable for such measurements due to site-controlled positioning of the dots which allows an easy access to a significant number of QDs even in side-view. This is achieved by cleaving the sample and placing in the cryostat facing the edge up (see the sketch in Figure 3.9-1(a)).

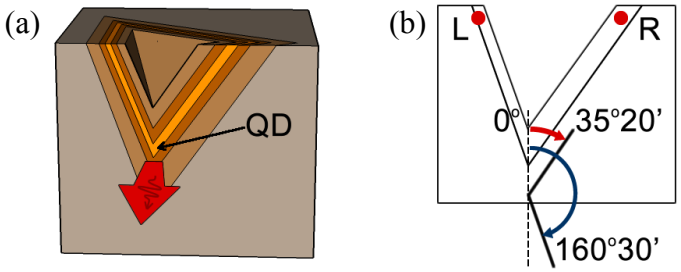


Figure 3.9-1. (a) The scheme of cross-section measurements. PL emitted through the cleaved side is analysed. (b) The projection of side-view of a pyramidal recess.

The initial characterization of the peaks in top-view showed very clear QD properties: exciton-biexciton dynamics, fine-structure splitting reflected in both transitions. A representative spectrum of LQDs simultaneously visible with PL of the main QD is shown in Figure 3.9-2. Both peaks were rarely observed jointly at the same excitation conditions due to the already mentioned poor main QD PL extraction efficiency, which forces relatively high pumping conditions. Thus the spectrum does not reflect the usual optical quality, which typically is justified by a narrow linewidth. In a previous report based on the same sample, the minimum linewidth of the main QD from a bright sample where the substrate was removed was typically found to be smaller than the resolution of the experimental set-up (18 μeV) even though, at the time, the interpretation of LQDs states was missing and some conclusions inaccurate[28,29].

The emitted photoluminescence was analyzed with a linear polarizer placed after the rotating half-wave plate. As presented in the inset of Figure 3.9-2, strong polarization anisotropy of the both PL features was observed. Polarization anisotropy is an expected result as it can be explained in the terms of a radiant dipole placed in a plane of a QD growth which is a valid picture if ground transitions between heavy-hole and electron are observed[26,30]. Advanced analysis and theoretical models demonstrated that polarization anisotropy can be a unique tool to probe transitions that involve different types of holes[26,31]. Here, the maximum intensity of the main QD (exciton transition) was observed when the linear polarizer was oriented along the growth plane and nearly suppressed when it was perpendicular. It is a symptomatic feature of the QD ground transitions involving heavy-hole recombination, somehow confirming the peaks are originated from the main QD. Unlike the main QD emission, LQDs revealed unusual polarization anisotropy properties which could not be simply related to heavy-(light-) hole properties. For example, the representative LQD presented in Figure 3.9-2, had a maximum at ~35˚.

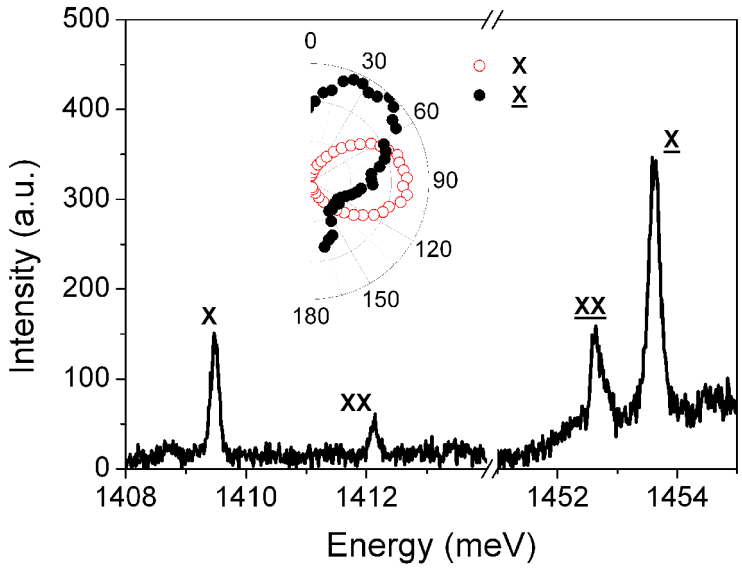


Figure 3.9-2. The PL spectrum of $In_{25}Ga_{0.75}As$ QD which simultaneously contains both types of QD features – lateral QDs (underlined) and central QDs. (The inset) Polarization anisotropy of exciton transition of LQD and central QD collected from cleaved edge geometry.

The results of this systematic study are shown in Figure 3.9-3. The maximum intensity values are very clearly bunched in three groups. As expected, the main QD PL always had maximum intensity polarized along ~90˚ (in the plane of growth),

while the LQD peaks had anisotropy maxima distributed around 35˚ and 160˚. The relevance of these angles becomes clearer, if the geometry of the pyramidal recess is taken into consideration. Figure 3.9-1(b) shows the projection of a measured pyramid cleaved in the plane perpendicular to one of the facets (the real orientation during the measurements) and the polarization analysis scheme (reference point, rotation direction). Considering 0˚ axes being perpendicular to the growth plane, 35˚20', 90˚ and 160˚30' are the angles that match the directions along the three projections. Since all three LQWrs are located as wedges between adjacent pyramidal facets, 35˚20' and 160˚30' also represent projections of the LQWrs. This fact suggests that there is a strong relation between the observed QD-like peaks (LQDs) and LQWrs. The polarization anisotropy maximum along the wire indicates that the LQD growth plane resides along the wire itself.

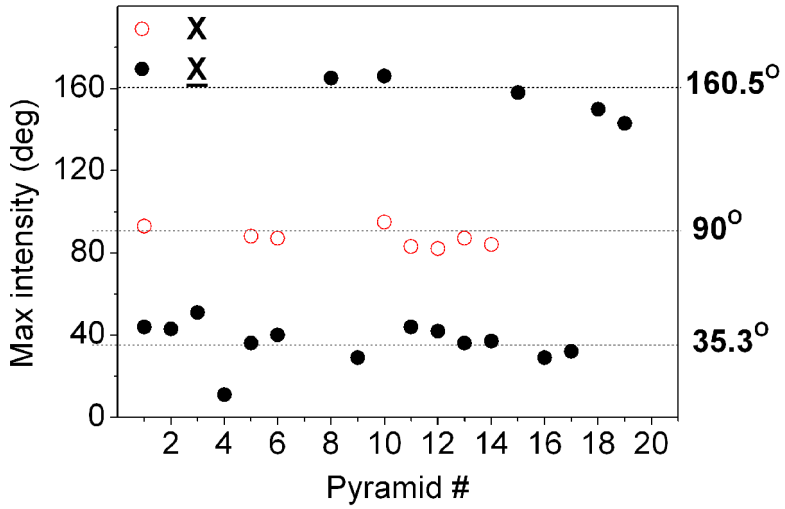


Figure 3.9-3. The distribution of polarization anisotropy maximum values of the central QDs (open circles) and LQDs (solid).

3.9.2 LQD indication by FSS measurements

A different approach was taken to clarify the origin of LQDs. The sample was characterized in a different geometry – conventional top-view. One point, which is valid for the previous method as well, has to be addressed before going into details. It was observed a clear correlation between the spatial excitation point and the maximum PL intensity of the LQDs. In side-view, the maximum intensity collection was optimum when the laser was focused to spots close to the growth

surface either on one or the other side of a pyramid projection (the spots L and R are indicated in Figure 3.9-1(b)). If the LQD emission was collected from the point R, the polarization anisotropy maximum was always along ~35˚20', while from the point L the anisotropy was associated to 160˚30'. The observations were consistent with similar behavior in top-view measurements. In fact, it was relatively easy to find pyramids with a number of simultaneously visible peaks while focusing the laser spot to the center of the pyramid. By moving the laser spot (and thus the probing point) to each of the pyramid corners, the PL intensity of a single pair of peaks (exciton and biexciton-like) increased while the rest of the peaks decreased. This situation is well illustrated in Figure 3.9-4, where insets with a single pyramid images exhibit excitation-probing points (bright spots) and the corresponding collected PL. Note that all the spectra contain fractions of each LQD spectrum.

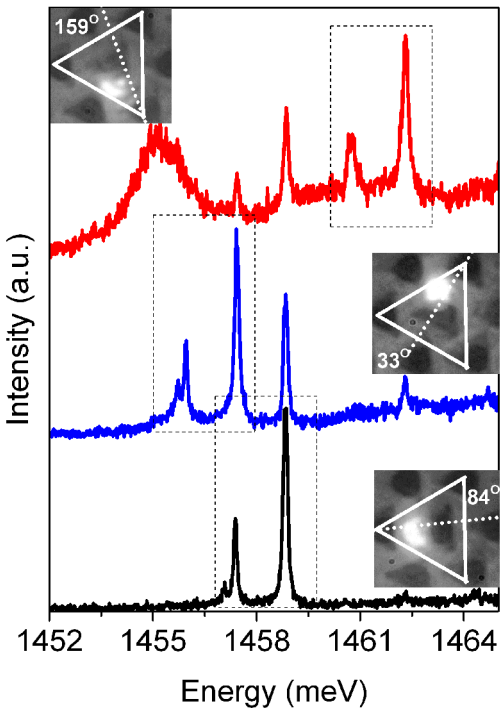


Figure 3.9-4. The PL spectra collected from a single pyramid to show the existence of three LQDs. PL is collected from different regions indicated by bright laser spots in the insets. Each dashed rectangle indicates a separate LQD. Dashed lines and degrees in the insets indicate the angle of a LQD polarization axis derived from a fine structure splitting measurement.

Moreover, the photoluminescence of single LQDs was observed at the edge of a sample, in top-view geometry but from the cleaved fractions of the pyramidal recesses which did not contain the central part where the main QD resides, confirming a significant physical separation between the LQDs and the central QD

(see Figure 3.9-5). It must be stressed that a special care was taken to make sure that PL was collected from the same pyramid and not from the adjacent ones as that might be the case if an extremely bright feature would be present nearby. According to these observations, the first assumption can be derived: there are three additional QD states in a pyramidal recess, they are closely related to LQWrs and spatially they are located close to the top of the sample and to the corners of a pyramidal recess.

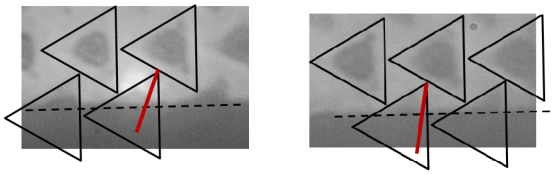


Figure 3.9-5. Two examples of cleaved pyramids with the PL of LQDs. The polarization axis of each LQD is shown by a red line.

All observed LQDs were characterized in terms of their carrier confinement potential symmetry by measuring the fine-structure splitting (FSS). The inset of Figure 3.9-6 presents a typical FSS detection procedure with the FSS value of ~21 μeV for the representative dot. Figure 3.9-6 summarizes FSS measurements of LQDs. Dots always had measurable FSS with a mean value of ~13 μeV which is rather small value in the context of other QD systems, but is significant when compared to the ~ zero the central dots can offer, and allows entangled photon emission (discussed in Chapter 5).

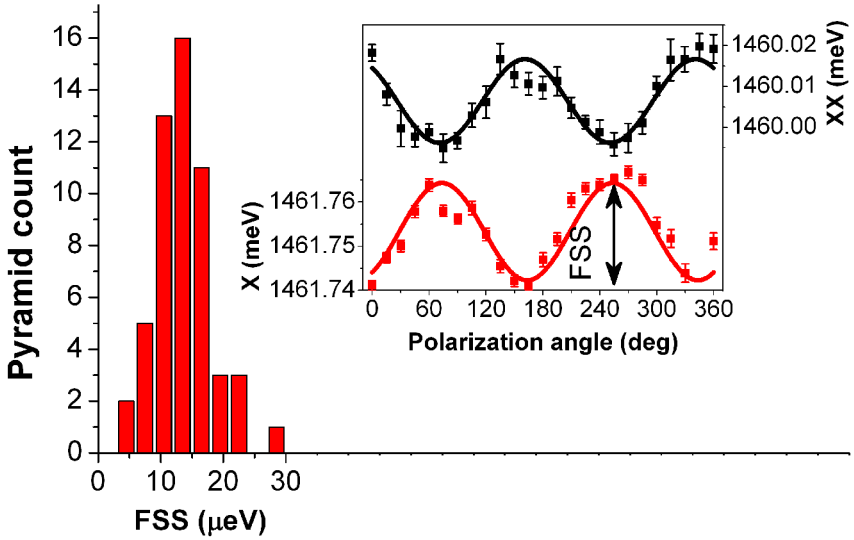


Figure 3.9-6. The distribution of the FSS values of LQDs. (The inset) A typical FSS measurement procedure – exciton and biexciton follow counterphase sinusoidal trend.

One of the main reasons for having a FSS is a QD elongation along a particular crystallographic direction[34,35]. The angles where the linear polarization components of the exciton (biexciton) are dominant can be called polarization axes of the QD. They usually match the QD elongation direction. In the representative FSS measurement of LQDs (the inset of Figure 3.9-6), the polarization axes of the particular LQD are at the sinusoid peak values of 73˚ and 163˚ (can be referred to as H and V). This data was systematically analyzed and presented in Figure 3.9-7(a). Since both axes are orthogonal, a single angle value, at which the exciton transition was the least energetic, was used. Values of polarization axis were bunched to three groups, scattered next to 30˚, 90˚ and 150˚. Similarly to side-view measurements, the relevance of these angles can be realized by taking into account the orientation of the pyramids within the measurement set-up. As presented in Figure 3.9-7(b), 30˚, 90˚ and 150˚ are the angles at which the center of a pyramid can be connected with each its corner or, otherwise, top-view projections of the LQWrs. The top inset of Figure 3.9-4 shows how the polarization axes correlate with the LQD location. All three LQDs were observed from this pyramid and their polarization axes were found to be 33˚, 84˚ and 159˚ as indicated in the insets. Analogously, the polarization axes directions of single LQDs found in the cleaved parts of pyramids are shown in Figure 3.9-5. It is obvious that the polarization axis of each LQD nearly matches direction of LQWrs. This was always the case for each measured LQD. This observation confirms that LQDs are indeed located within LQWrs which are most likely responsible for the observed FSS properties (e.g., due to a small dot elongation along a wire).

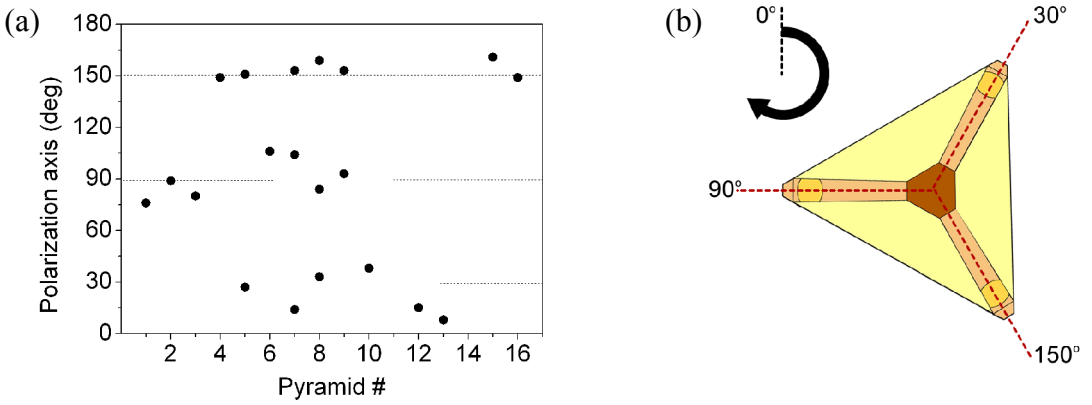


Figure 3.9-7. (a) The distribution of the polarization axis angles of LQDs. (b) The top-view of a pyramid indicating the angles LQWrs projections.

3.9.3 Speculation on the origin of LQDs

The analyzed sample with LQDs had exceptional uniformity and density of these states, observed nearly from half (or nearly all in some areas) of the pyramids. A lower density of LQDs with more random properties (emission energy, an excitonic pattern, fine-structure splitting values) has been observed in other samples of different alloy concentration and/or thickness (for example see the spectrum of $In_{0.45}Ga_{0.55}As$ structures in Figure 3.4-1). Some of these samples are analyzed in Ref. 29 despite the wrong identification of the type of nanostructures (i.e. they have been considered to be the central dots). Such systematic observation indicates that the LQDs are indeed an intrinsic structural feature of InGaAs/GaAs pyramidal heterostructures, and should not be neglected, nor misinterpreted as the main, highly symmetric central dot.

The fact that sometimes this feature is not pronounced or missing in some samples, is an issue which needs discussion. Probably this can be attributed to the primal post-growth processing step which is routinely performed (surface etching) which is meant to etch away irregular growth structures close to the surface of the pyramidal recesses. The procedure is essential, as the mentioned irregularities comprise a broad photoluminescence background which overlaps with the systematic features from the pyramidal recess. The lack of a precise control of the post growth processing procedure might result in “etched away” LQDs, as they are likely to be close to the surface. This would explain why these structures have been overlooked for so long in the scientific literature.

Despite the obvious proof of their existence, the structural origin of LQDs is still obscure, and more work will be needed in the future to investigate their origin.

3.10 Summary

InGaAs pyramidal site-controlled QDs confined by GaAs possess substantially different optical properties than the counterparts confined by AlGaAs barriers. A bBiexciton present at higher energy than the exciton was shown for the first time as a characteristic feature. The QD optical properties (emission energy, biexciton binding energy) could be deterministically controlled solely with the epitaxial growth parameters and conditions without compromising the optical quality of QDs. An

improved picture of the over-all ensemble of self-formed InGaAs nanostructures found in pyramidal recesses was presented by identifying a new type of nanostructure: a lateral quantum dot. In general, three spatially separated lateral QDs were located at the top corners of a pyramidal recess. A meticulous study of a new type of QD-like nanostructure allowed, for the first time, a clear differentiation between the two QD-like structures (lateral and central QDs) and their properties, importantly clarifying the interpretation of previous results which appeared in the literature.

Bibliography

[1] A. Hartmann, Y. Ducommun, L. Loubies, K. Leifer, and E. Kapon, Appl. Phys. Lett. 73, 2322 (1998).

[2] A. Hartmann, Y. Ducommun, K. Leifer, and E. Kapon, J. Phys.: Condens. Matter 11, 5901 (1999).

[3] M. Grundmann and D. Bimberg, Phys. Rev. B 55, 9740 (1997).

[4] M. Abbarchi, C. Mastrandrea, T. Kuroda, T. Mano, A. Vinattieri, K. Sakoda, and M. Gurioli, J. Appl. Phys. 106, 053504 (2009).

[5] M. Wimmer, S. V. Nair, and J. Shumway, Phys. Rev. B 73, 165305 (2006).

[6] G. A. Narvaez, G. Bester, A. Franceschetti, and A. Zunger, Phys. Rev. B 74, 205422 (2006).

[7] M. Fox, Quantum Optics: An Introduction (Oxford Master Series in Physics, 6) (Oxford University Press, USA, 2006).

[8] A.V. Kuhlmann, J.H. Prechtel, J. Houel, A. Ludwig, D. Reuter, A.D. Wieck, R.J. Warburton, arXiv:1307.7109 (2013).

[9] V. Turck, S. Rodt, O. Stier, R. Heitz, R. Engelhardt, U. W. Pohl, D. Bimberg, and R. Steingruber, Phys. Rev. B 61, 9944 (2000).

[10] G. Sallen, et al., Nat Photonics 4, 696 (2010).

[11] A. V. Kuhlmann, J. Houel, A. Ludwig, L. Greuter, D. Reuter, A. D. Wieck, M. Poggio, and R. J. Warburton, Nat Phys 9, 570 (2013).

[12] S. Ates, S. M. Ulrich, S. Reitzenstein, A. Loffler, A. Forchel, and P. Michler, Phys. Rev. Lett. 103, 167402 (2009).

[13] V. Dimastrodonato, E. Pelucchi, and D. D. Vvedensky, Phys. Rev. Lett. 108, 256102 (2012).

[14] A. Schliwa, M. Winkelnkemper, and D. Bimberg, Phys. Rev. B 79, 075443 (2009).

[15] C. Jarlov, P. Gallo, M. Calic, B. Dwir, A. Rudra, and E. Kapon, Appl. Phys. Lett. 101, 191101 (2012).

[16] M. H. Baier, E. Pelucchi, E. Kapon, S. Varoutsis, M. Gallart, I. Robert-Philip, and I. Abram, Appl. Phys. Lett. 84, 648 (2004).

[17] S. Rodt, R. Heitz, A. Schliwa, R. L. Sellin, F. Guffarth, and D. Bimberg, Phys. Rev. B 68, 035331 (2003).

[18] B. H. Sorcha and P. O. R. Eoin, Journal of Physics: Conference Series 245, 012022 (2010).

[19] K. Kim and A. Zunger, Phys. Rev. Lett. 86, 2609 (2001).

[20] J. Wu, W. Shan, and W. Walukiewicz, Semicond. Sci. Technol. 17, 860 (2002).

[21] E. P. O'Reilly, A. Lindsay, P. J. Klar, A. Polimeni, and M. Capizzi, Semicond. Sci. Technol. 24, 033001 (2009).

[22] D. J. Friedman, J. F. Geisz, S. R. Kurtz, J. M. Olson, and R. Reedy, J. Cryst. Growth 195, 438 (1998).

[23] L. Auvray, H. Dumont, J. Dazord, Y. Monteil, J. Bouix, and C. Bru-Chevalier, J. Cryst. Growth 221, 475 (2000).

[24] V. Dimastrodonato, L. O. Mereni, R. J. Young, and E. Pelucchi, Phys. Status Solidi B 247, 1862 (2010).

[25] F. Lelarge, C. Constantin, K. Leifer, A. Condo, V. Iakovlev, E. Martinet, A. Rudra, and E. Kapon, Appl. Phys. Lett. 75, 3300 (1999).

[26] K. F. Karlsson, V. Troncale, D. Y. Oberli, A. Malko, E. Pelucchi, A. Rudra, and E. Kapon, Appl. Phys. Lett. 89, 251113 (2006).

[27] V. Troncale, K. F. Karlsson, D.Y. Oberli, M. Byszewski, A. Malko, E. Pelucchi, A. Rudra and E. Kapon, J. Appl. Phys. 101, 081703 (2007).

[28] L. O. Mereni, V. Dimastrodonato, R. J. Young, and E. Pelucchi, Appl. Phys. Lett. 94, 223121 (2009).

[29] L. O. Mereni, O. Marquardt, G. Juska, V. Dimastrodonato, E. P. O'Reilly, and E. Pelucchi, Phys. Rev. B 85, 155453 (2012).

[30] R. M. Stevenson, R. J. Young, P. See, C. E. Norman, A. J. Shields, P. Atkinson, and D. A. Ritchie, Appl. Phys. Lett. 87, 133120 (2005).

[31] Y. H. Huo, B. J. Witek, S. Kumar, R. Singh, , E. Zallo, R. Grifone, D. Kriegner, R. Trotta, N. Akopian, J. Stangl, V. Zwiller, G. Bester, A. Rastelli, O. G. Schmidt, arXiv:1208.6554.

Chapter 4

4 Single and correlated photon emission

Intensity correlation measurements of photons emitted from single quantum dots is a powerful tool to characterise a QD and its quality by obtaining a second order temporal coherence function (a second order correlation function). This method allows demonstrating single photon emission, probing multiexcitonic transitions and carrier dynamics. In this chapter, QDs are characterised at low temperature (~8K) by this technique. Moreover, some scholarly examples of correlation spectroscopy application to QD characterisation are discussed, and shown how they apply to pyramidal QDs.

4.1 Pulsed and continuous-wave modes

The general expression of a second-order correlation function is given by the relation:

$$g_{i,j}^{(2)}(\tau) = \frac{\langle I_i(t) I_j(t+\tau) \rangle}{\langle I_i(t) \rangle \langle I_j(t) \rangle}, \tag{4.0}$$

where $I_n(t)$ is the intensity of the n-th excitonic complex at time t. It represents a conditional probability of a j-th excitonic complex photon to be detected at the time point τ, after an i-th excitonic complex photon is detected. If the same excitonic complex is being probed ($i=j$), the obtained function conventionally is called auto-correlation, while if $i \neq j$, it is called cross-correlation.

The set-up (Hanbury, Brown and Twiss arrangement) to measure the second-order correlation is shown in Chapter 2. However, depending on the excitation source type – pulsed or continuous-wave, $g^{(2)}(\tau)$ can have two different representations. Each excitation mode comes with different capabilities to characterise a QD by photon statistics. For example, an important characteristic is the value of $g^{(2)}(0)$ of the auto-correlation, which indicates how good is a QD as a source of single photons. In a continuous-wave mode, an ideal $g^{(2)}(\tau)$ curve of an ideal single photon source would have a dip which at $g^{(2)}(0)$ would be equal to zero indicating

single photon emission. However, due to inevitable effects of a poor timing resolution present in the set-up, an experimentally obtained curve is the result of the convolution of the real $g^{(2)}(\tau)$ curve and the instrument-response function. To obtain a $g^{(2)}(0)$ value, a deconvolution process is required which can be tricky. Such process would require the knowledge of the instrument response function, lifetime of the transition, noise level and/or carrier capture rate. By using too broad bounds of the parameters, or wrong values, which indeed can be strongly excitation power dependent, an estimated $g^{(2)}(0)$ value can be unreliable. These problems can be 'completely' overcome by a pulsed mode. As it is explained later, the pulsed mode allows measuring $g^{(2)}(0)$ value directly, which then can reliably be used in the quantum information processing tasks. Moreover, photons on demand can be obtained only in a pulsed mode, thus it is the most practically useful. However, correlation measurements under continuous-wave excitation should not be underestimated, as this way is a powerful method to probe the dynamics of the carriers, especially when multiexcitonic transitions are involved.

4.2 Correlations under continuous-wave excitation

If a continuous-wave source is used to excite a QD, the following carrier dynamics scenario is valid. After non-resonant excitation, a QD is randomly populated by electrons and holes which quickly relax to the lowest unoccupied levels creating electron-hole pairs: excitons[1]. Provided that electrons and holes are captured at nearly the same rate (there is no charging of a QD), a single parameter – electron-hole pair capture time constant t_{eh} – describes the population. It is expected to be dependent on the experimental conditions, such as excitation power, which modifies the density of the reservoir of carriers available to populate a QD. If a QD is occupied by a single e-h pair, the recombination occurs spontaneously and is characterised by a photoluminescence decay constant τ_x (lifetime). A single photon is emitted during this process leaving the QD empty. Another e-h pair is injected by the capture process with a time constant of t_{eh}, which is typically of the order of nanoseconds. Thus the conditional probability to detect the second photon immediately after the first one is vanishing, resulting in single photon emission and antibunching in the second-order *auto*-correlation function.

A different dynamic is observed when a QD is populated by two e-h pairs. Such excitonic complex fully recombines in the cascade. At first, the recombination proceeds by the emission of a single photon (biexciton) with decay constant τ_{xx} and the QD remains occupied by a single e-h pair which then decays to the ground state. Both transitions ideally are single photon sources, as the scenario of an e-h pair capture→recombination→capture is still valid, except that exciton now is additionally being fed by the recombination of a biexciton. Thus the conditional probability to detect an exciton photon after the detection of biexciton becomes high and it is highlighted by bunching in the second-order *cross*-correlation function.

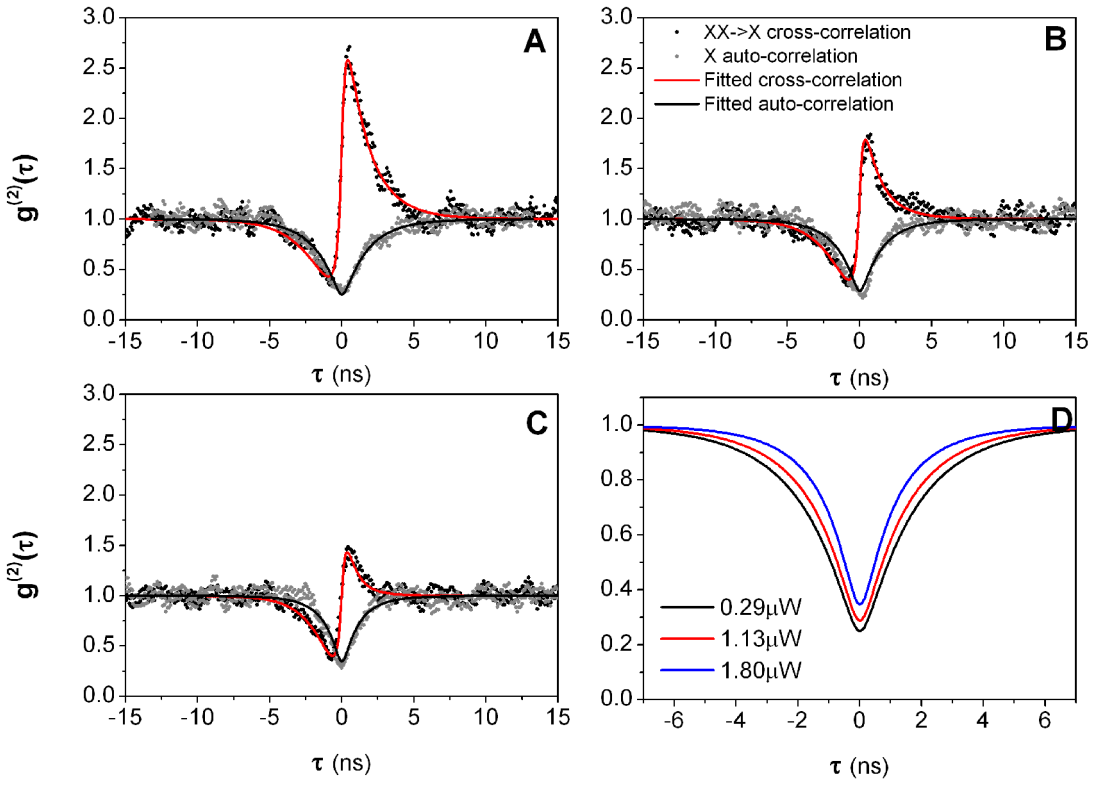


Figure 4.2-1. (A, B, C) Cross- and auto-correlation data obtained at different excitation powers (0.29 μW, 1.13 μW and 1.8 μW). The data is fitted using three-level rate equations. (D) The comparison of auto-correlation curves.

Figure 4.2-1 shows representative exciton (X) auto-correlations and biexciton-exciton (XX-X) cross-correlations taken at different excitation powers from the sample S#12. Both curves were obtained simultaneously at each excitation power, in order to avoid any deviations due to the sample drifting or laser intensity fluctuations. Such set of data could be reliably used to fit a well-established QD

recombination model presented below. To interpret the curves, several points have to be addressed. The presence of negative time values between two single-photon detection events is an 'artefact' enabled by the configuration of the electric delay line which was plugged to the STOP channel of the correlation set-up. During the processing, the curves are then artificially shifted back by the amount of time taken by the electric triggering signal to travel the delay line[2]. When $\tau>0$, the XX-X cross-correlation data can be related to the conditional probability to detect an exciton photon when the biexciton photon was detected, while $\tau<0$ represents probability to detect the biexciton after the recombination of the exciton. By applying the same logic to any auto-correlation curve, it can be concluded that it has to be symmetric respect to $\tau=0$.

The dip is visible in all X auto-correlation curves in Figure 4.2-1. At the lowest excitation power, the minimum $g^{(2)}(\tau)$ value is 0.23 – a clear proof of single photon emission. Zero value is not reached because of the limited timing resolution. As shown in Figure 4.2-1, a convolution with the instrument-response function, which is a good approximation of a Gaussian with its width of 500 ps, is capable to reproduce the experimentally observed curves with a very good agreement. Biexciton-exciton cross-correlation curves have characteristic properties of the recombination cascade. At positive delay times, strong bunching indicates emission of two photons one after another. These data combined with excitation power dependent (Figure 4.2-2) and PL lifetime measurements (τ_x=1.85 ns, τ_{xx}=0.8 ns) can be unambiguously used to identify the type of the excitonic transitions.

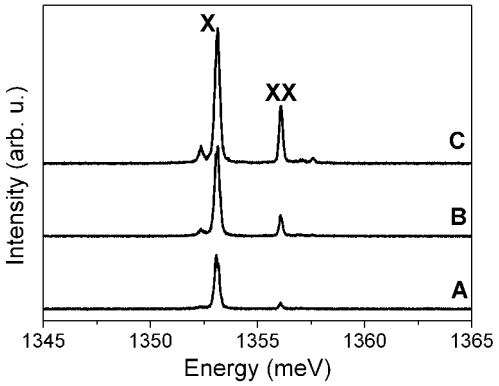


Figure 4.2-2. PL spectra of a representative QD at the excitation conditions used in the correlation measurements. Only exciton and biexciton transitions are dominant.

4.3 Modelling correlation curves

To explain the evolution of the correlation curves seen in Figure 4.2-1 at different excitation power values, a theoretical model can be applied[3,4]. The model considers that e-h pairs are captured creating excitonic complexes identified by the number of charge carriers present in a dot. By the recombination of a single e-h pair present in the ground level (and the possible following rapid thermalisation of carriers to the new state) a new complex is created which can recombine in the same manner. The set of rate equations 4.1 describes temporal evolution of excitonic complexes in the QD. Evolution of multiexciton (N in total) occupation probabilities $\vec{p}(t) = \left[p_0(t), p_1(t), \ldots, p_N(t)\right]$ is used to simulate the second-order correlation function:

$$\frac{d\vec{p}(t)}{dt} = \begin{pmatrix} -\left(1/t_{eh} + 1/\tau_0\right) & 1/\tau_1 & 0 & 0 & 0 & 0 & 0 \\ 1/t_{eh} & -\left(1/t_{eh} + 1/\tau_1\right) & 1/\tau_2 & 0 & 0 & 0 & 0 \\ & & & \vdots & & & \\ 0 & 0 & 0 & 1/t_{eh} & -\left(1/t_{eh} + 1/\tau_{N-1}\right) & 1/\tau_N & 0 \\ 0 & 0 & 0 & 0 & 0 & 1/t_{eh} & -1/\tau_N \end{pmatrix} \begin{pmatrix} p_0(t) \\ p_1(t) \\ \cdots \\ p_{N-1}(t) \\ p_N(t) \end{pmatrix} \quad (4.1)$$

where τ_i is the multiexciton photoluminescence lifetime, except τ_0 being equal to ∞. The positive terms describe feeding of the i-th state which occurs either due to the capture of an e-h pair by the (i-1)-th multiexciton or either by the radiative recombination of the (i+1)-th multiexciton. All the probabilities at each time point sum up to unity:

$$\sum_{i=0}^{N} p_i(t) = 1. \quad (4.2)$$

The second-order correlation curves presented in Figure 4.2-1 were obtained by populating the QD mainly by two excitons, as indicated by Figure 4.2-2 which shows the PL spectra at the corresponding excitation conditions. No charged or higher order than biexciton multiexcitons were present, thus the system could be considered as the three level system described by the three rate equations:

$$\begin{aligned} \frac{dp_0}{dt} &= -\frac{p_0}{t_{eh}} + \frac{p_X}{\tau_X} \\ \frac{dp_X}{dt} &= \frac{p_0}{t_{eh}} + \frac{p_{XX}}{\tau_{XX}} - p_X\left(\frac{1}{t_{eh}} + \frac{1}{\tau_X}\right) \\ \frac{dp_{XX}}{dt} &= \frac{p_X}{t_{eh}} - \frac{p_{XX}}{\tau_{XX}} \end{aligned} \quad (4.3)$$

By applying appropriate initial conditions, the solutions can be used to express correlation functions[4]. The exciton auto-correlation function $g^{(2)}_{X,X}(t)$ requires to set the initial conditions so that the QD would be in the ground state ($p_0(0)$=1, $p_x(0)$=0 and $p_{xx}(0)$=0 for the solutions when $t\geq 0$). Then the auto-correlation is:

$$g^{(2)}_{X,X}(t) = \begin{cases} p_X(t)/p_X(\infty) & t \geq 0 \\ g^{(2)}_{X,X}(-t) & t < 0 \end{cases} \tag{4.4}$$

In order to represent a cross-correlation function between biexciton and exciton, the initial conditions for positive delay time ($t\geq 0$) have to set the QD to the state which could reflect the conditional probability to detect an exciton photon after the recombination of a biexciton ($p_0(0)$=0, $p_x(0)$=1 and $p_{xx}(0)$=0). At negative delay time, $g^{(2)}_{XX,X}(t)\big|_{t<0}$ represents the probability of detecting a biexciton photon when the QD is initially in the ground state ($p_0(0)$=1, $p_x(0)$=0 and $p_{xx}(0)$=0). The cross-correlation then can be obtained from the equations:

$$g^{(2)}_{XX,X}(t) = \begin{cases} p_X(t)/p_X(\infty) & t \geq 0 \\ p_{XX}(-t)/p_{XX}(\infty) & t < 0 \end{cases} \tag{4.5}$$

The rate equations (4.3) were solved numerically, convoluted with the instrument-response function and fitted to the experimental data presented in Figure 4.2-1 (the sample S#12). The only variable parameter was the capture time t_{eh}, as the photoluminescence decay constants τ_x and τ_{xx} were measured directly. Figure 4.3-1 presents the characteristic e-h pair capture time dependence on the excitation power. The capture rate ($1/t_{eh}$) is decreasing at lower power. At the lowest measured power (Figure 4.2-1(A)) 0.17 e-h pair/ns were captured. The capture rate reduction is explained by the reduced reservoir of carriers in the vicinity of the QD.

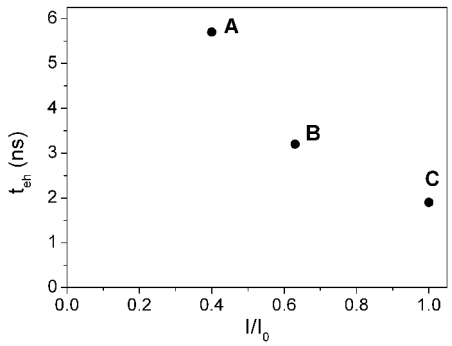


Figure 4.3-1. The capture time at different excitation powers.

The capture rate dependence on the excitation power is reflected in the evolution of $g^{(2)}_{XX,X}(t)$. At the lowest power the maximum value is 2.7, while at the highest power it drops to 1.5 (Figure 4.2-1). At higher power, the probability to capture an e-h pair is increasing. If a pair is captured while the QD is populated by an exciton ($p_x(0)$=1), a biexciton is created and thus a full recombination cascade has to occur again in order to detect an exciton photon. If the capture happens multiple times (i.e., there is a high probability of generating a biexciton before the recombination cascade happens), the maximum bunching value is significantly reduced.

The auto-correlation dip tends to narrow, as the excitation power is increased. By further reducing excitation power, a low injection mode is achieved. In the case when biexciton is not created anymore, the QD can be described as the two level system:

$$\begin{aligned} \frac{dp_0}{dt} &= -\frac{p_0}{t_{eh}} + \frac{p_X}{\tau_X} \\ \frac{dp_X}{dt} &= \frac{p_0}{t_{eh}} - \frac{p_X}{\tau_X} \end{aligned} \tag{4.6}$$

By solving the rate equations, it is possible to show that the autocorrelation has the following expression:

$$g^{(2)}_{X,X}(t) = 1 - \exp[-|t|(1/\tau_X + 1/t_{eh})] \tag{4.7}$$

As the excitation power is decreased, $t_{eh} \gg \tau_x$ and the dip of the second-order correlation function is determined only by the exciton lifetime. Thus $g^{(2)}_{X,X}(t)$ can be used to obtain exciton lifetime at low excitation conditions.

4.4 Pulsed excitation mode

When a QD is excited by pulsed excitation, the QD is expected to be excited only once, fully relax to the ground state emitting a single photon or a sequence of single photons and ideally it should be re-excited only by the upcoming laser pulse. This mode allows deterministic population of QDs and thus single photon control[5,6]. Since any events related to different excitation pulses are separable, this allows a direct measurement of the second-order correlation function value (unlike in a continuous-wave excitation mode), which then can be used as a state intensity in

various quantum information processing tasks. For this reason, this mode is very important for practical applications.

A typical pulsed second-order correlation curve is composed of the detection events bunched around the time values separated by the laser period values nT, where n is an integer (Figure 4.4-1). The appearance of $nT(|n|>0)$ peaks is possible because of the imperfect detection process[7]. In fact, losses occur due to poor photon extraction and collection from a QD, in the optical elements, by monochromators, in the detection efficiency. The typical overall efficiency of a regular QD system without QD coupling to a cavity can be estimated as a fraction of percent. This can lead to the situation where a photon counting module triggered by a single photon is stopped by a second photon after hundreds or thousands of laser periods. The integration of such events results in the rise of side peaks.

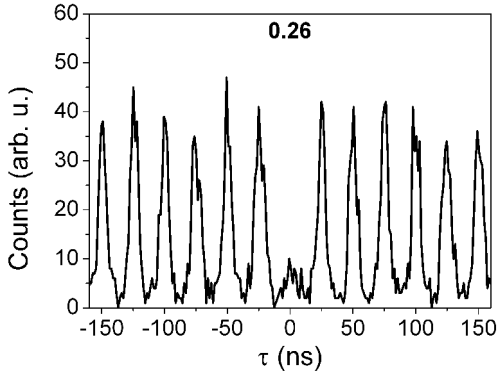


Figure 4.4-1. An example of a pulsed auto-correlation obtained from one of the pyramidal QDs (sample S#12).

The events near n=0 are of the most importance and they are used to calculate the second-order correlation function value. If an auto-correlation curve of a QD transition is being measured, two-photon events are expected to be suppressed and $g^{(2)}_{n=0}=0$. If a cross-correlation between photons emitted in the cascade is measured, photon bunching is expected. The second-order correlation function value can be measured by integrating events of the zero peak N_0 and dividing by an average value of a few closest $nT(|n|>0)$ peaks:

$$g^{(2)}(0)=\frac{N_0}{N/n}, \tag{4.8}$$

where N is the total number of events of n side-peaks. Typically measurements were made using 40 MHz, 635 nm wavelength laser excitation of 100 ps pulse width. N_0 was obtained by integrating the range from -12.5 ns to 12.5 ns.

The example of single photon emission is shown in Figure 4.4-1. The suppression of correlation counts around 0 ns value indicates reduced probability of two-photon emission events. In this case (Figure 4.4-1), the directly measured value of the second order correlation function is 0.26.

4.5 Visibility of the biexciton-exciton cascade bunching

Figure 4.5-1 shows $g^{(2)}_{xx,x}(0)$ dependence on the excitation power (the sample S#26). The highest $g^{(2)}_{xx,x}(0)$ value (3.58) was obtained at the lowest excitation. By increasing excitation power 3.2 times, the $g^{(2)}_{xx,x}(0)$ value has dropped to 1.35, close to the level of uncorrelated peaks. This needs a discussion.

The visibility of XX-X bunching has been theoretically and experimentally studied in Ref. 7, which is referred to in order to discuss the observed results. In principle, the reasons of bunching visibility reduction at higher power could be thought as the result of multiexcitonic transitions appearance close to the emission energy of both exciton and biexciton. However, by carefully choosing filtering conditions, this assumption could be ruled out in this case. The reason of $g^{(2)}_{xx,x}(0)$ reduction was shown to be rather not of a physical origin, but purely a statistical effect which appears in realistic photon-correlation set-ups[7]. By using analysis based on Poissonian statistics of a QD occupation and photon emission, it could be concluded that bunching tends to decrease strongly with increasing probability to find together both, exciton and biexciton, photons generated by each laser pulse[7]. While ideally such emission (each pulse always generates a pair of exciton-biexciton photons) would be the most favourable, practically it leads to poor measurement results because of the limited over-all detection efficiency. Thus excitation conditions where a biexciton-exciton pair creation happens very occasionally tend to provide the best result in the terms of bunching visibility.

The dependence of the second-order cross-correlation function on excitation power has the following expression[7]:

$$g^{(2)}(0) = \left(1 - \exp(-\langle n \rangle)\right)^{-1}, \tag{4.9}$$

where $\langle n \rangle$ is the mean number of excitons in a QD. $\langle n \rangle$ can be related to the excitation power using power dependent measurements (not shown), which can be described by a Poissonian statistics. The obtained dependence of a QD presented in Figure 4.5-1 is $\langle n \rangle = 0.005 P^{1.22}$. The fact that the relation is non-linear is discussed in the next section. By using it in the equation (4.9), an excellent agreement between the experimental data was found. The highest $g^{(2)}_{xx,x}(0)$ value was found when an average QD population was ~0.3 excitons over multiple excitation cycles – far less than the value of 2 which would indicate the highest probability to create biexciton with each excitation pulse. In practice, a trade-off in the experimental conditions had to be found, as at the lowest excitation powers, the intensity of the biexciton transition was getting closer to the value of dark counts and integration times were unreasonably long. The typical conditions for entanglement tests presented in the Chapter 5 are marked by the ellipse in Figure 4.5-1. The intensity ratio I_x / I_{xx} was ~15 as seen in Figure 4.5-1(A).

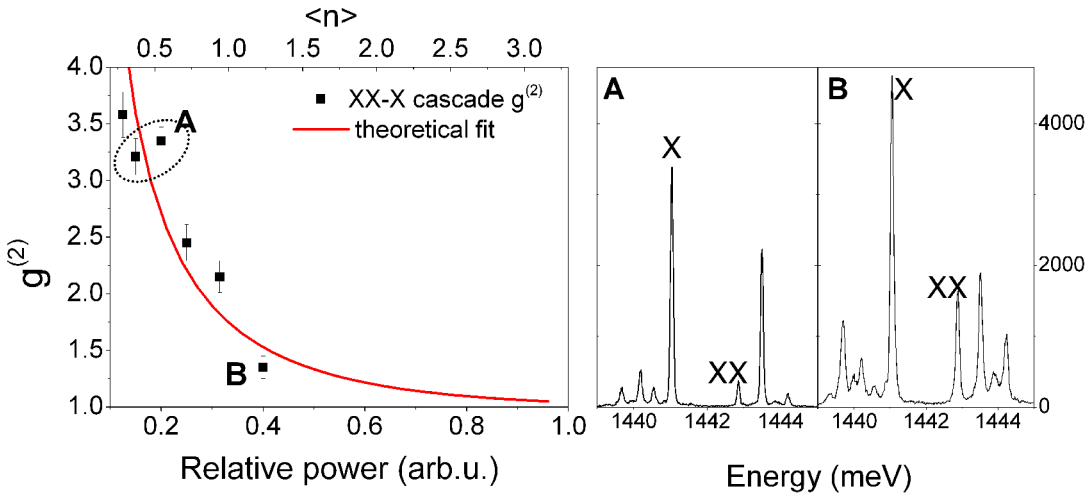


Figure 4.5-1. (Left)The second-order correlation function dependence on excitation power and theoretical fitting in one of the representative samples (S#26). Letters A and B indicate spectra (right) of a QD.

4.6 Quantum dot feeding

Figure 4.6-1 presents exciton and biexciton integrated intensity as a function of excitation power (the sample S#12). The intensity of exciton at low power is strongly

superlinear ($I_x \sim P^{1.5}$) – a typical feature of pyramidal QDs studied in this work. The result clearly deviates from the theoretical predictions and experimental observations, where a linear dependence is often obtained.

Power dependence of exciton and biexciton transitions under continuous-wave excitation can indeed be modeled using the rate equations (4.2) and (4.2). A steady-state solution of (4.3) is then required. The three-level rate equations present the QD occupation probability, thus the emission of a photon is proportional to a corresponding radiative recombination term:

$$\begin{aligned} I_X &\sim \frac{n_X}{\tau_X} = \frac{1}{\tau_X}\left(1 + \frac{t_{eh}}{\tau_X} + \frac{\tau_{XX}}{t_{eh}}\right)^{-1} \\ I_{XX} &\sim \frac{n_{XX}}{\tau_{XX}} = \frac{1}{\tau_{XX}}\left(1 + \frac{t_{eh}}{\tau_{XX}} + \frac{t_{eh}^2}{\tau_X \tau_{XX}}\right)^{-1} \end{aligned} \tag{4.10}$$

Here a capture (pump) rate $p = 1/t_{eh}$ can be introduced. If it is assumed that the capture rate is directly proportional to the excitation power (p~P)[8,9], this leads to the observation of a linear and quadratic dependence of exciton and biexciton intensity, respectively. However, as it was already pointed out[10], a simple assumption of a direct dependence of the QD feeding rate on the excitation power is not necessarily valid, due to the potentially complex QD feeding mechanisms.

To test a possibility of a non-linear QD feeding rate, the pump rate p was measured as a function of power. As described in the section 4.3, p was obtained by fitting the second-order correlation curves taken at different excitation powers. A non-linear dependence was found and p could be described by the relation:

$$p = 1/t_{eh} = \alpha P^{\gamma}, \tag{4.11}$$

with γ=1.58±0.16. By using this directly measured dependence, lifetimes (τ_x=1.3 ns, τ_{xx}=0.6 ns) and the equation 4.10, intensity fittings of X and XX were made (Figure 4.6-1). Good fittings were obtained of both I_X and I_{XX} (the same scaling parameters were used).

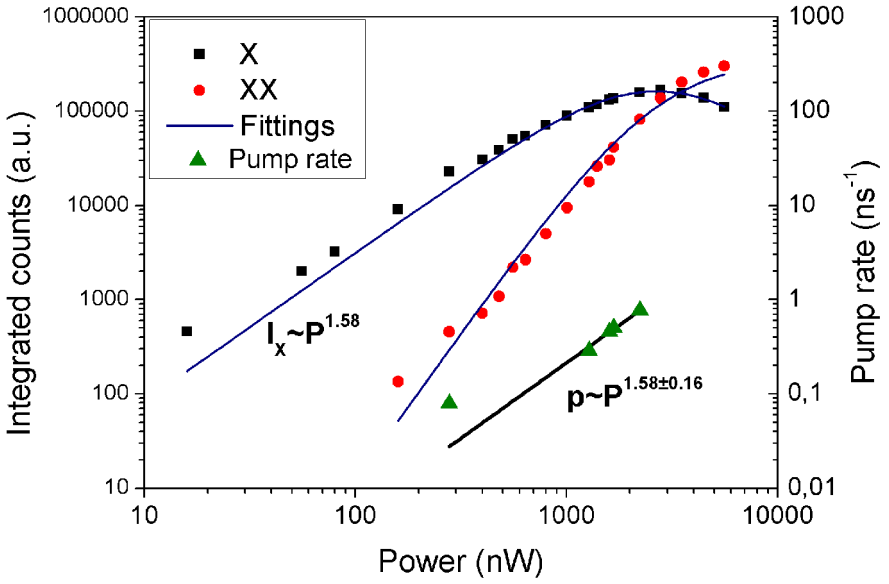


Figure 4.6-1. The power dependence of the intensity of exciton and biexciton transitions. The capture (pump) rate of the same QD is obtained from auto-correlation curves measured at different excitation powers. The measured capture rate dependence on the excitation power is used to fit the intensity data.

The pyramidal QD system is complex and several QD feeding scenarios are conceivable, especially when the excitation is non-resonant. A few speculations can be made by analyzing second-order auto-correlation curves obtained in pulsed mode (Figure 4.6-2). In this case, $g^{(2)}_{X,X}(0)$ has never been suppressed to vanishing values in a pulsed excitation mode. Poor single photon purity indeed would be a serious issue in various quantum information processing schemes. However, the problem itself is not new and can be efficiently overcome by using resonant or quasi-resonant excitation schemes[11,12]. There might be a few other reasons of two-photon emission, such as background, dark-counts of the detectors, poor filtering of single excitonic transition, re-excitation of a QD with the same laser pulse, re-capture of long-lived carriers from the barrier material. In this case, all but the last one can nearly certainly be ruled out. Re-capturer of carriers would occur when carriers are trapped in the vicinity of a QD. If their recombination rate is comparable to the QD exciton's one, there is non-vanishing probability that after the emission of an exciton, a QD is re-populated with another electron-hole pair. Such dynamics reminds continuous-wave excitation, when a QD is re-populated after it becomes empty. A closer inspection of $g^{(2)}_{X,X}(0)$ peak of two different QDs measured (Figure 4.6-2(a)) shows that there is a

dip at τ=0. The presence of a dip is consistent with the re-capture model. The origin of the dip is the same as in a continuous-wave excitation mode where it indicates single photon emission. It is not reaching zero value because of the limited timing resolution.

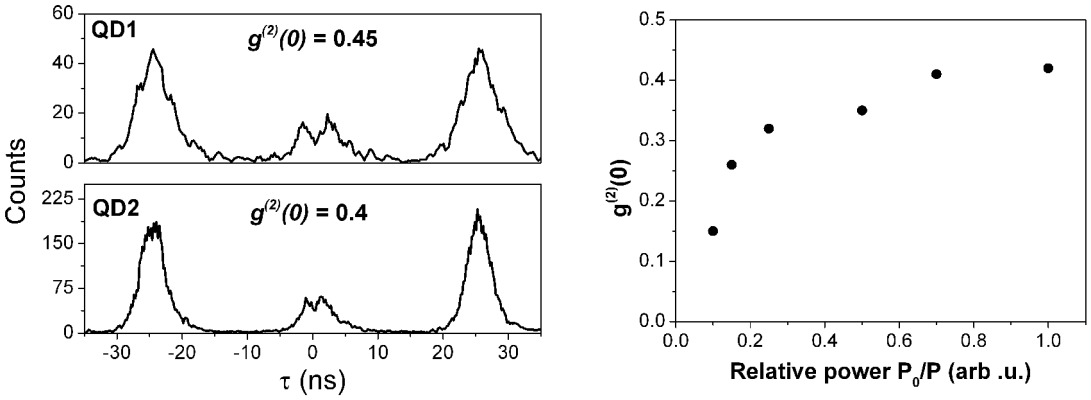


Figure 4.6-2. (a) The second-order auto-correlation curves of two different QDs. (b) The second-order auto-correlation function value dependence on the excitation power for a specific QD from the sample (S#12).

While fundamentally single photon emission is preserved, practically no true deterministic single photon emission is provided in this case. In some cases, it is possible to reduce $g^{(2)}_{X,X}(0)$ value to ~0.15 (Figure 4.6-2(b)) by reducing excitation power, however, two-photon emission has not been suppressed completely. These results show that QD feeding is complex and deviations in power-dependent measurements can be justified.

4.7 Probing multiexcitonic transitions

A significant number of quantum dots were found with a particular constant excitonic pattern composed of multiple relatively sharp lines (< 40 μeV), which was also found to be an important property of entangled photon emitters studied in this work (see Figure 4.7-1). The presence of multiple lines is a clear indication of the existence of multiexcitonic complexes, created due to charging of a QD. Charging of a QD indicates imbalance between electron and hole capture rate. Photon correlation spectroscopy can be employed to indicate the type of the transitions and study the dynamics of carriers[13].

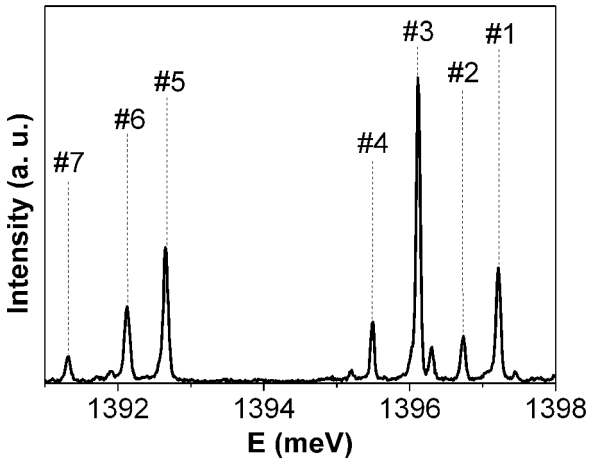


Figure 4.7-1. The spectrum of a representaive QD with multiexcitonic transitions identified in the analysis.

Initially, the representative QD (the sample S#18) was characterised by basic excitation power dependence and lifetime measurements which can be very informative, as they reveal the dynamics of charge carriers. Figure 4.7-2 presents integrated intensity of the seven most prominent transitions (labelled in Figure 4.7-1) at different excitation power. The measured lifetime values of the corresponding transitions are presented in the boxes of each figure. The brightest transition #3 always appears nearly simultaneously with #5 and both usually depend linearly or slightly super-linearly. This is a typical signature of charged and neutral excitons, which tend to be visible as the first ones at low excitation power. At higher power other transitions start to appear. Strong super-linear dependence, appearance at higher power, shorter photoluminescence lifetime (≤1 ns) of the transitions #1, #2, #4 and #7 would suggest them being excitonic complexes that participate in the recombination cascade as initial or intermediate states, but not the final ones.

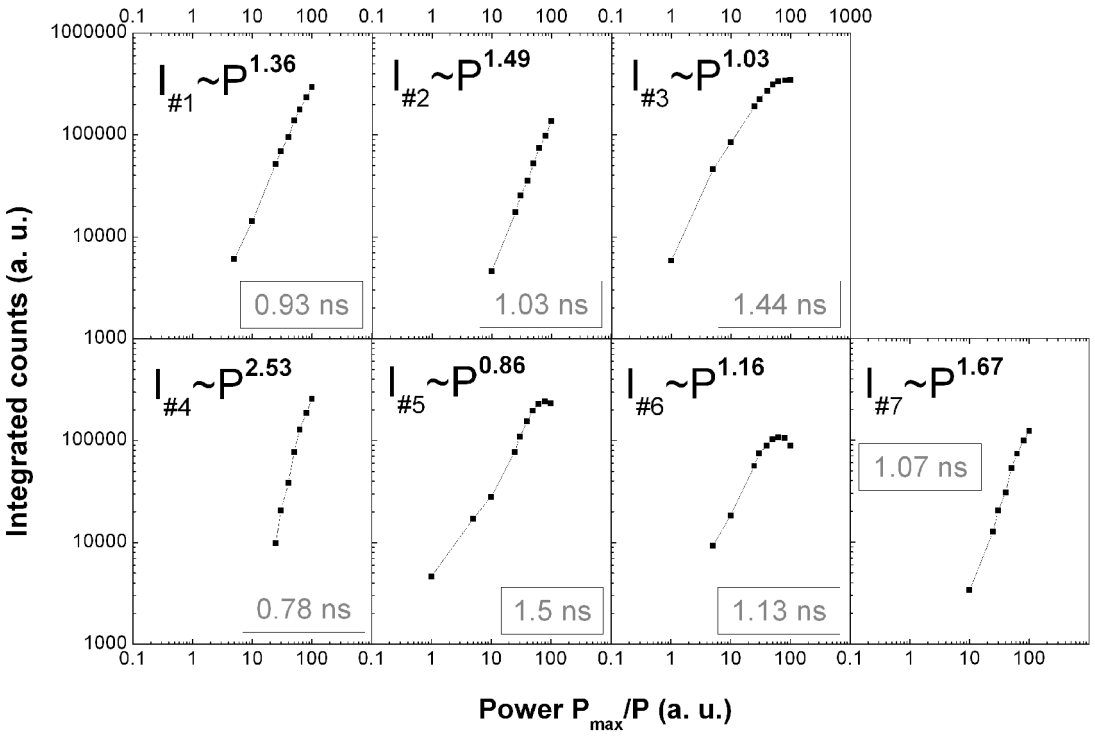


Figure 4.7-2. Intensity power dependence of the analysed transitions. The PL lifetime values are outlined.

An unambiguous indication of the transitions #4 and #5 as biexciton (XX) and exciton (X) was made from multiple measurements. Cross-correlation between XX and X confirmed strong bunching in $g^{(2)}(t>0)$ – a clear signature of a recombination cascade (Figure 4.7-3). A simple three level rate equation model could not be applied anymore, as it produced only poor fitting results (not shown). This a clear indication that additional generation or decay terms exist due to imbalanced electron-hole capture rates and the rate equation model presented above is not valid anymore. Moreover, a tiny fine-structure splitting of ~3 μeV was found and polarization resolved classical type polarization correlations were obtained (see Chapter 5.2 for more details). A clear indication of X and XX could be used as a strong reference point analysing cross-correlation data between the other unknown transitions.

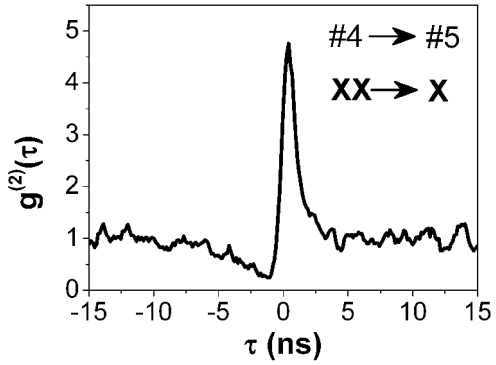


Figure 4.7-3. The cross-correlation curve between exciton and biexciton transitions.

Cross-correlation results between #5 (X) – #3 and #5 (X) – #6 transitions are shown in Figure 4.7-4(a). The preliminary indication of these peaks as charged excitons is confirmed by asymmetric antibunching – a characteristic feature of neutral and charged exciton correlations[13]. The dip is narrower at negative correlation time values because the conditional probability to detect a neutral exciton after the emission of a positive (negative) charged exciton is higher as the capture of only a single electron (hole) is required to create a neutral exciton. The occurrence of the reverse event requires capturing of three charge carriers, thus it is less likely to happen as indicated by a well pronounced dip at positive delay values.

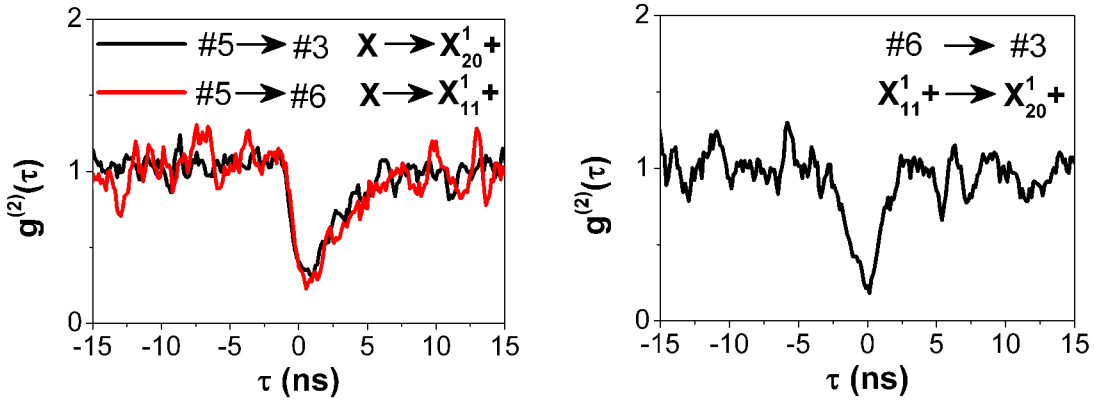


Figure 4.7-4. (a) The cross-correlations between transitions #5 and #3 (#6). (b) The cross-correlation between #6 and #3.

Cross-correlation between both charged complexes #3 and #6 has a clear symmetric dip – an evidence that both excitonic complexes do not coexist in a QD in a short time scale and the conditional probability of the occurrence of one event after the other is nearly equal. This information alone is not sufficient to identify the

charging type of the complexes, however, with the help of other cross-correlations a few feasible configurations can be easily ruled out.

The shapes of #5 (X) – #3 and #5 (X) – #6 curves are identical. According one scenario, it could be possible that both, #3 and #6, are of an opposite charging. However, asymmetry in hole and electron capture rate in principle should cause different shape of $g^{(2)}_{\#3}(\tau)$ and $g^{(2)}_{\#6}(\tau)$, even though it is not a strong argument to confirm the same charging. As explained below, this could be achieved by cross-correlations with peaks #1 and #2, and the fact that #3 and #6 are of the opposite sign was ruled out. The symmetric antibunching between #3 and #6, and identical cross-correlations with #5 (X) would suggest that both excitons are of the same charge, however, different spin configurations. The most probable configurations are positive (X+) or negative trions (X-). An alternative possibility of a double charged exciton X++ (X--)[14,15] could be considered as well, however, there is no obvious reason why a double charged exciton complex (#6 and #3 both) should be the brightest and coexist with the neutral exciton at different excitation powers without the presence of a trion (X+ or X-).

Assignment of the charging type and energetic transitions ordering is not trivial. Theoretical calculations show that various configurations of excitonic complex energetic order are possible and could be used as a fingerprint of a QD structural and morphological properties[16]. However, a positive trion was observed at higher energy in the majority of experiments (the summary can be found in Ref. 16). Moreover, a good agreement with positive charge configurations, namely, the fine structure of 'hot trion'[17,18,19] was found in this work. A source of positive charging could be an unintentional intrinsic p-type doping by carbon, which indeed can be observed in the PL spectra as a strong PL band below the bulk GaAs energy ($\Delta E = -18$ meV). Nevertheless, an unambiguous indication of the charging type can be made only by charging the QD when integrated in a light-emitting diode type structure[20], which unfortunately was not available at this experiment stage. A less reliable, but informative way would be studying thinner QDs, which are expected to have only a single confined electron level (and thus no possibility to form a negative biexciton) and, possibly, only a few hole levels. Indeed, thinner dots have very similar pattern, as discussed in Chapter 5, however they are usually less 'charged' and that rich

variety of excitonic complexes or their intensity was not visible. By taking into account the mentioned arguments, the charging type was tentatively attributed to positive and used as such in further representation and analysis of the data.

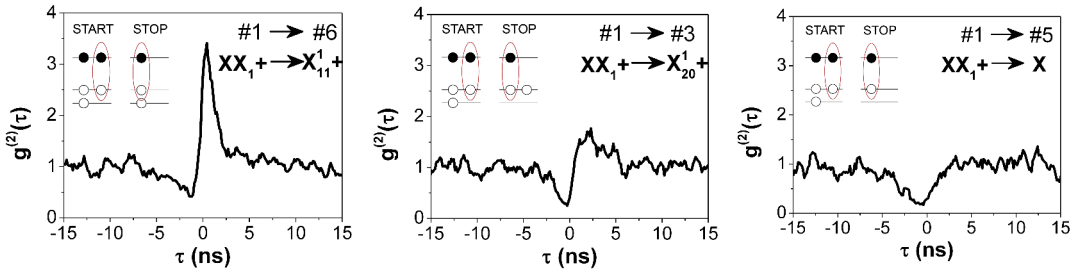


Figure 4.7-5. The cross-correlations between the transitions labelled at the top of each graph.

Cross-correlations between #1 and assumed positively charged trions X+ #3, #6 of different spin configurations, along with a neutral exciton #5 are shown in Figure 4.7-5. Strong photon bunching was observed between #1 and #6 transition photons, indicating the presence of a direct recombination cascade. Less pronounced bunching was obtained between #1 and #3, and antibunching between #1 and #5. This observation can be also used to justify the assignment of the same charging of #3 and #6. In the case of opposite charging, the second-order correlation curve of #1-#3 (for example, XX+ vs. X-) transitions should have had an even more pronounced antibunching than #1-#5.

Strong bunching between #1 and #6 indicated #1 belonging to a positively charged biexciton XX_1+. To understand the origin of the other multiexcitons, the electronic and fine structure of positively charged biexciton and positively charged trions needs to be discussed. A positively charged biexciton is composed of two electrons occupying the s-shell in the conduction band, and three holes in the valence band – two in the s-shell, and one partially occupying the p-shell. Two degrees of freedom (2^1) are present because of the angular momentum of the latter, and thus the initial state is double degenerate (there is no exchange interaction to cause the fine structure splitting). The final state is a positively charged exciton, so called 'hot trion' ($X^1_{1,1}+$) which has rather complex fine-structure reflected in the emission of a charged biexciton[21,22,23]. It is composed of one electron in the s-shell of the conduction band, and two remaining holes in the valence band s- and p-shells,

respectively. Since all particles are in different energetic levels of a QD, there are eight possible configurations (2^3) to the respect of their spin/angular momentum orientation. The electronic structure is mostly influenced by the isotropic exchange interaction of two identical particles – holes. The eight-fold degenerate level is split by hole-hole exchange interaction to a two-fold singlet level, and six-fold triplet level. The singlet level $S_{\pm1/2}$ is at higher energy and has the total spin z-projection equal to $m_z=\pm1/2$. The triplet level is further separately modified by electron-hole exchange interaction resulting in splitting of two-fold triplet levels from each other. Each double-degenerate 'hot trion' triplet level $T_{\pm1/2}$, $T_{\pm5/2}$ and $T_{\pm7/2}$ has $m_z=\pm1/2$, $\pm5/2$ and $\pm7/2$, respectively. This fine structure scheme is shown in Figure 4.7-6.

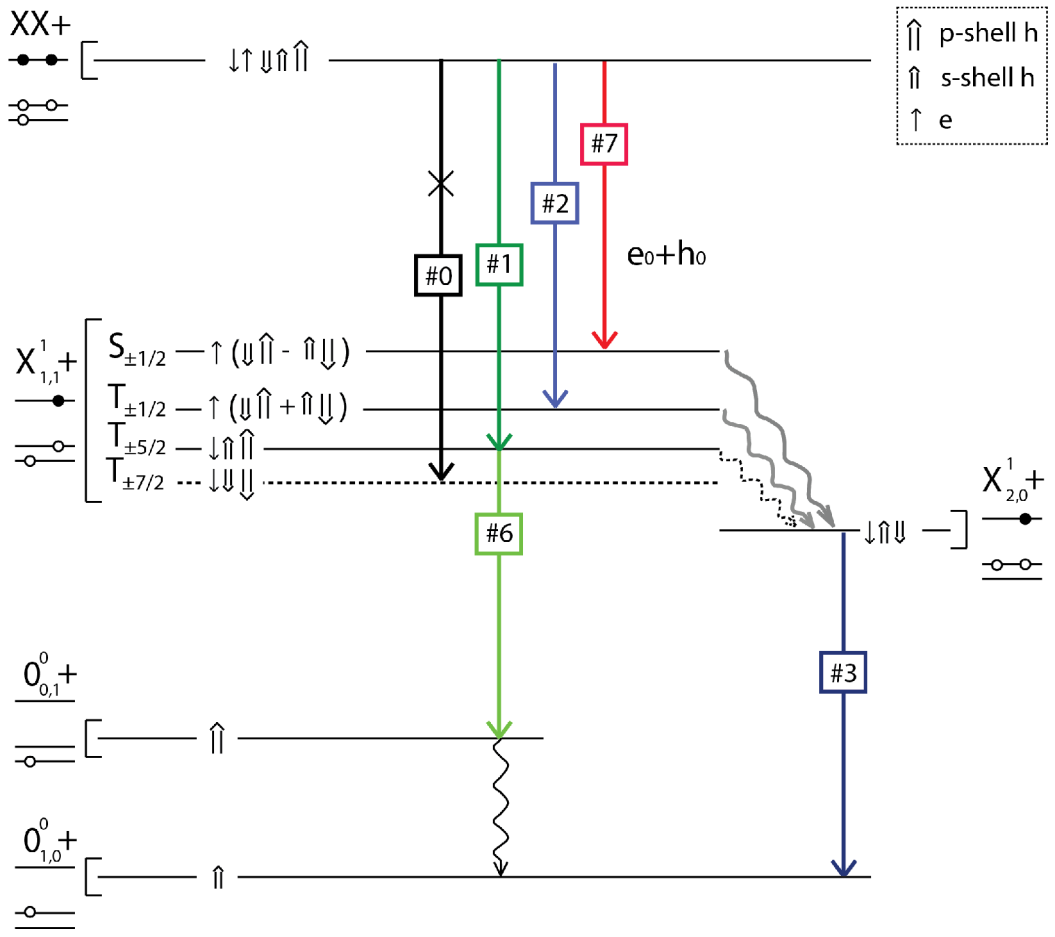


Figure 4.7-6. The proposed decay scheme of a positively charged biexciton.

Following the scenario of a positive biexciton decay, it is clear that the fine structure of a hot trion is partially reflected by XX+ photoluminescence. There are four possible recombination paths, however, $T_{\pm7/2}$ (#0) is a dark states and the

probability of coupling to a photon is very low. Typically it is not observed in the photoluminescence, unless the mixing of the triplet states is strong[18]. The rest three XX+ states were experimentally observed by different methods and the contributions are in good agreement identifying the states and there energetic order[17,18,19,21].

The characteristic feature of XX+ states $T_{\pm1/2}$, $T_{\pm5/2}$ is ~double intensity of $T_{\pm5/2}$ compared to $T_{\pm1/2}$, and the energetic separation between the triplet states being much smaller than between the singlet state $S_{\pm1/2}$ (a few hundred μeV vs. a few meV). Attribution of the states $T_{\pm1/2}$, $T_{\pm5/2}$ and $S_{\pm1/2}$ to #2, #1 and #7, respectively, is consistent with these details.

In the final state of a hot trion, a few recombination channels are available. (1) If a singlet trion state $S_{\pm1/2}$ is created (by the emission of #7), the hole from the p-shell very rapidly (in a few ps)[24] relaxes to the ground state (the process is indicated by a wavy arrow in the scheme of Figure 4.7-6), creating a new, singlet trion state $X^1_{2,0}+$. It is the typical, well known excitonic complex composed of two holes and electron in the ground state. There is no particle exchange interaction in this complex and the fine-structure is fairly simple allowing only a single optical transition. So the further relaxation proceeds with the emission of the positively charged, ground trion (#3). It is a new state created because of the fast hole relaxation and by all means does not reflect the fine structure of a hot trion $X^1_{1,1}+$ by the emission energy or so. Because of the rapid $X^1_{2,0}+$ creation, $X^1_{1,1}+$ singlet state is not visible in the optical spectrum. (2) If XX+ decays to $T_{\pm1/2}$ state (#2), the same recombination channel is used. However, in order to relax to the ground trion, a phase term of $T_{\pm1/2}$ state has to be changed by π to transform it to $S_{\pm1/2}$ and then decay to $X^1_{2,0}+$. Both states have the same spin projection, thus the process is quick and happens in a few tens of picosends[19,24]. (3) The last triplet state $T_{\pm5/2}$ (#1) requires the change of the momentum projection by -2 in order to relax through the same channel. Such process is less probable in QDs and can happen in a few hundred of picoseconds[19,24]. This time scale is sufficient to allow the hot trion to relax by radiative recombination, introducing the second relaxation channel. In this case, recombination of a hot trion can be directly observed in the photoluminescence spectrum (#6).

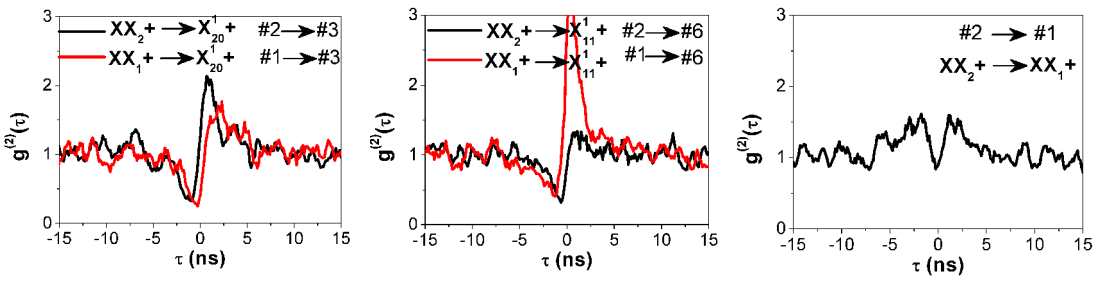


Figure 4.7-7. The cross-correlations between the transitions labelled at the top of each graph.

The presented QD relaxation scheme was tested by cross-correlation measurements presented in Figure 4.7-7. As discussed, the source of the transition #3, ground trion $X^1_{2,0}+$, are expected to be all three optically active XX+ transitions #2, #7 and partially #1. Unfortunately, cross-correlations with #7 have not been done at the time of the experiment, and its assignment to $S_{\pm 1/2}$ is mainly based on PL energy, excitation power dependence and lifetime measurements. The cross-correlations with the remaining two transitions #1 and #2 vs. #3 indeed bunch at positive delay time values (Figure 4.7.7(a)) confirming the feeding of the ground exciton. Figure 4.7.7(b) shows cross-correlations with the same charged biexciton transitions and #6 – hot trion. Two recombination channels are expected, because of the hole spin-flip and radiative recombination. Radiative recombination is confirmed by the very strong bunching between #1 and #6. On the other hand, the spin flip and relaxation through $S_{\pm 1/2}$ to $X^1_{2,0}+$ (#3) is somehow confirmed by weaker bunching between #1 and #3 (Figure 4.7.7(a)). However, the high intensity of #6 is a good indicator that such spin-flip process in these QDs is a slow process, comparable to the lifetime (~1 ns). Figure 4.7.7(c) shows that #1 and #2 do not participate in the recombination cascade. A rather symmetric curve shows bunching ('shoulders') approaching a zero delay value which at 0 ns is replaced by a symmetric untibunching – an indication of single photon emission. Such bunching shoulders can be obtained in the autocorrelation curves when excitation is high (the carrier capture time is small). This can be easily confirmed with the three level rate equations (4.3). Thus the cross-correlation between #1 and #2 can be regarded as an auto-correlation, which is consistent with the fact that both transitions belong to the same excitonic complex XX+.

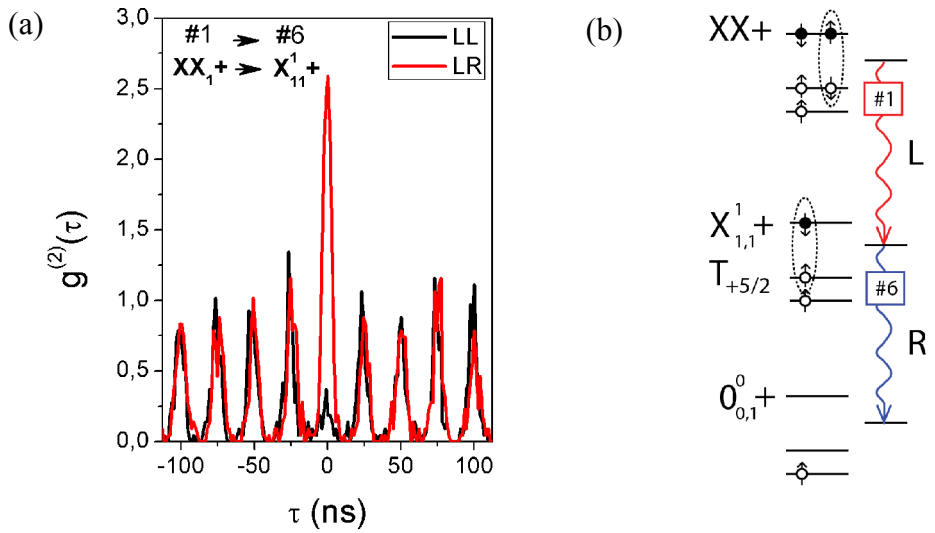


Figure 4.7-8. (a) Polarization resolved cross-correlations between transitions #1 and #6 in circular basis. (b) The recombination cascade of the transitions #1 and #6.

In general, the second order correlation curves with the transition #3 ($X^1_{2,0}+$) have less pronounced bunching features. This is not surprising as the feeding sources of #3 are three XX+ states and the neutral exciton X (by capturing a hole). This causes high counts of uncorrelated light which reduces a well pronounced indication of a recombination cascade (or so). The situation is different for #1 and #6 cross-correlation as can be seen from $g^{(2)}_{\#1,\#6}(\tau)$. According to the proposed recombination scheme, the only source of #6 is expected to be #1. Experimentally it was confirmed by making polarization resolved correlation measurements (Figure 4.7-8(a)). Two cross-correlation curves were measured simultaneously in circular polarization basis – left-hand polarized photons of #1 were correlated with left-hand and right-hand photons of #6. Strong correlation between counter-circularly polarized photons was obtained, along with very well pronounced antibunching in a co-polarized photon correlation curve. Such type of correlations is expected to occur, when a QD is populated by a positively charged biexciton with the spin projection of +3/2. Figure 4.7-8(b) indicates the decay scheme, where left-hand circularly polarized XX+ photon is followed by left-hand polarized $X^1_{1,1}+$. An analogous decay but with opposite polarization states occurs when a QD is populated by XX+ with m_z=-3/2. The same polarization correlations are expected to occure in circular basis in the

entanglement tests, where biexciton-exciton recombination scheme is employed. However, the latter should not be confused with this case, as #1-#6 cascade generates only a classical mixture of $\left|L_{(+3/2)XX+}R_{(+5/2)X+}\right\rangle$ and $\left|R_{(-3/2)XX+}L_{(-5/2)X+}\right\rangle$ photons, that would fail the entanglement tests.

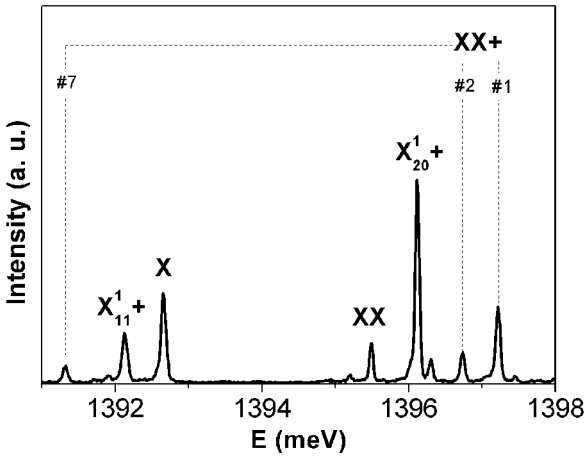


Figure 4.7-9. The labelled excitonic transitions.

The labelled excitonic configuration based on the experimental observations discussed above is presented in Figure 4.7-9.

4.8 Summary

Pyramidal QDs were shown as single photon sources, while QD population dynamic was studied by photon correlation spectroscopy, for the first time in such systems. Excitation power dependent measurements combined with theoretical modelling results showed atypical QD population dynamics, which deviated from a usual linear dependence. Further studies showed that a non-trivial QD feeding mechanism existed. Moreover, a specific excitonic pattern of highly symmetric QDs was studied. Charged and neutral excitonic complexes were identified from the cross-correlation measurements. The recombination cascade from a positively charged biexciton through an excited charged exciton was shown to be contributing to the photoluminescence spectra. All these findings were important, original steps for clarifying excitonic formation and dynamics, improving largely on the existing knowledge, and feeding important information into the development of the results of the next chapter.

Bibliography

[1] M. Grundmann and D. Bimberg, Phys. Rev. B 55, 9740 (1997).

[2] S. Felekyan, R. Kuhnemuth, V. Kudryavtsev, C. Sandhagen, W. Becker, and C. A. M. Seidel, Rev. Sci. Instrum. 76, 083104 (2005).

[3] E. Dekel, D. Gershoni, E. Ehrenfreund, J. M. Garcia, and P. M. Petroff, Phys. Rev. B 61, 11009 (2000).

[4] D. V. Regelman, U. Mizrahi, D. Gershoni, E. Ehrenfreund, W. V. Schoenfeld, and P. M. Petroff, Phys. Rev. Lett. 87, 257401 (2001).

[5] P. Michler, A. Kiraz, C. Becher, W. V. Schoenfeld, P. M. Petroff, L. Zhang, E. Hu, and A. Imamoglu, Science 290, 2282 (2000).

[6] C. Santori, M. Pelton, G. Solomon, Y. Dale, and Y. Yamamoto, Phys. Rev. Lett. 86, 1502 (2001).

[7] T. Kuroda, et al., Phys. Rev. B 79, 035330 (2009).

[8] M. Grundmann and D. Bimberg, Phys. Rev. B 55, 9740 (1997).

[9] C. Santori, G. S. Solomon, M. Pelton, and Y. Yamamoto, Phys. Rev. B 65, 073310 (2002).

[10] M. Abbarchi, C. Mastrandrea, T. Kuroda, T. Mano, A. Vinattieri, K. Sakoda, and M. Gurioli, J. Appl. Phys. 106, 053504 (2009).

[11] A. Malko, M. H. Baier, K. F. Karlsson, E. Pelucchi, D. Y. Oberli, and E. Kapon, Appl. Phys. Lett. 88, 081905 (2006).

[12] C. Santori, D. Fattal, J. Vuckovic, G. S. Solomon, and Y. Yamamoto, Nature 419, 594 (2002).

[13] M. H. Baier, A. Malko, E. Pelucchi, D. Y. Oberli, and E. Kapon, Phys. Rev. B 73, 205321 (2006).

[14] M. Ediger, G. Bester, B. D. Gerardot, A. Badolato, P. M. Petroff, K. Karrai, A. Zunger, and R. J. Warburton, Phys. Rev. Lett. 98, 036808 (2007).

[15] B. Urbaszek, R. J. Warburton, K. Karrai, B. D. Gerardot, P. M. Petroff, and J. M. Garcia, Phys. Rev. Lett. 90, 247403 (2003).

[16] A. Schliwa, M. Winkelnkemper, and D. Bimberg, Phys. Rev. B 79, 075443 (2009).

[17] E. Poem, J. Shemesh, I. Marderfeld, D. Galushko, N. Akopian, D. Gershoni, B. D. Gerardot, A. Badolato, and P. M. Petroff, Phys. Rev. B 76, 235304 (2007).

[18] T. Warming, E. Siebert, A. Schliwa, E. Stock, R. Zimmermann, and D. Bimberg, Phys. Rev. B 79, 125316 (2009).

[19] Y. Igarashi, et al., Phys. Rev. B 81, 245304 (2010).

[20] M. Baier, F. Findeis, A. Zrenner, M. Bichler, and G. Abstreiter, Phys. Rev. B 64, 195326 (2001).

[21] R. Seguin, S. Rodt, A. Schliwa, K. Potschke, U. W. Pohl, and D. Bimberg, Physica Status Solidi B-Basic Solid State Physics 243, 3937 (2006).

[22] I. A. Akimov, K. V. Kavokin, A. Hundt, and F. Henneberger, Phys. Rev. B 71, 075326 (2005).

[23] V. Mlinar and A. Zunger, Phys. Rev. B 80, 205311 (2009).

[24] M. E. Ware, et al., Phys. Rev. Lett. 95, 177403 (2005).

Chapter 5

5 Polarization-entangled photons

In this chapter, pyramidal quantum dots are shown as polarization-entangled photon sources at the temperature of 8K. A high density of such sources is reported. Finally, several different growth conditions and QD parameters are discussed which were successfully used to produce highly symmetric QD samples.

5.1 Showing polarization-entanglement

A typical protocol to reveal entanglement, which resides in the superposition of two-photon (biexciton and exciton) polarization states, is to measure polarization resolved second-order correlation functions[1]. An expected maximally entangled state of a photon pair emitted from an ideally symmetric QD is expressed as $|\psi\rangle = \frac{1}{\sqrt{2}}\left(|L_{XX} \otimes R_X\rangle + |R_{XX} \otimes L_X\rangle\right)$, where L and R represent a left and right circular polarization state of a biexciton (XX) and an exciton (X). As, in general, a pure polarization state can be expressed as a superposition of two other orthogonal pure polarization states (e.g., $|R\rangle = \frac{1}{\sqrt{2}}\left(|H\rangle + i|V\rangle\right)$, $|L\rangle = \frac{1}{\sqrt{2}}\left(|H\rangle - i|V\rangle\right)$, $|D\rangle = \frac{1}{\sqrt{2}}\left(|H\rangle + |V\rangle\right)$, $|A\rangle = \frac{1}{\sqrt{2}}\left(|H\rangle - |V\rangle\right)$, where H, V, D and A represent horizontal vertical, diagonal and antidiagonal states), the maximally entangled state can be rewritten in terms of these states and thus expressed in different polarization bases:

$$\begin{aligned}
|\psi\rangle &= \tfrac{1}{\sqrt{2}}\left(|L_{XX} \otimes R_X\rangle + |R_{XX} \otimes L_X\rangle\right) = \\
&= \tfrac{1}{\sqrt{2}}\begin{pmatrix} \left|\tfrac{1}{\sqrt{2}}\left(|H_{XX}\rangle - i|V_{XX}\rangle\right) \otimes \tfrac{1}{\sqrt{2}}\left(|H_X\rangle + i|V_X\rangle\right)\right\rangle + \\ + \left|\tfrac{1}{\sqrt{2}}\left(|H_{XX}\rangle + i|V_{XX}\rangle\right) \otimes \tfrac{1}{\sqrt{2}}\left(|H_X\rangle - i|V_X\rangle\right)\right\rangle \end{pmatrix} = \\
&= \tfrac{1}{2\sqrt{2}}\begin{pmatrix} |H_{XX} \otimes H_X\rangle + i|H_{XX} \otimes V_X\rangle - i|V_{XX} \otimes H_X\rangle + |V_{XX} \otimes V_X\rangle + \\ + |H_{XX} \otimes H_X\rangle - i|H_{XX} \otimes V_X\rangle + i|V_{XX} \otimes H_X\rangle + |V_{XX} \otimes V_X\rangle \end{pmatrix} = \\
&= \tfrac{1}{\sqrt{2}}\left(|H_{XX} \otimes H_X\rangle + |V_{XX} \otimes V_X\rangle\right)
\end{aligned} \tag{5.1}$$

Analogously, in the diagonal basis, the state is transformed to:

$$|\psi\rangle = \tfrac{1}{\sqrt{2}}\left(|D_{XX} \otimes D_X\rangle + |A_{XX} \otimes A_X\rangle\right). \tag{5.2}$$

The expressed two photon polarization superposition states indicate correlation of counter-polarized photons in circular basis and correlation of co-polarized photons in linear and diagonal bases.

5.2 Influence of the FSS

As discussed in the introductory part in Chapter 1, the fine structure splitting (FSS) complicates polarization entanglement detection. If a FSS is big enough (a few μeV), polarization correlation is observed only in linear basis (so called classical correlation)[2]. An example of a QD from the sample S#18 with a FSS of ~3 μeV is shown in Figure 5.2-1. Correlations measured in linear, diagonal and circular bases are presented in Figure 5.2-2. Polarization correlation is observed only in linear bases between co-linearly polarized photons, while polarization correlations are completely lost in diagonal and circular bases.

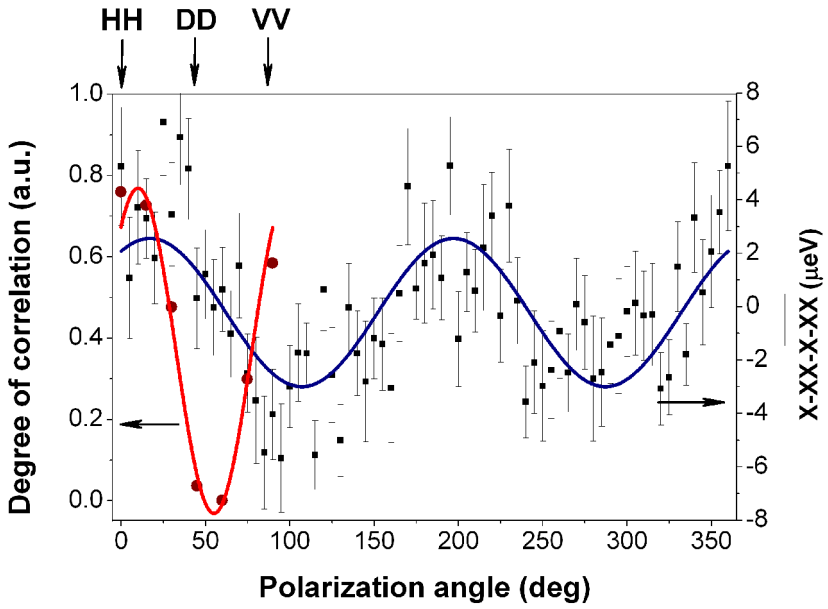


Figure 5.2-1. An example of the fine-structure splitting and degree of correlation measurement. The blue curve represents the fitting of exciton and biexciton emission energy difference subtracted by the average biexciton binding energy. The amplitude of the fitted sinusoidal function is equal to the fine-structure splitting (~3 μeV). The red curve represents the degree of correlation measured at different linear polarization (a half-wave plate) angle.

Classical-like correlations can be indicated by measuring the degree of correlation as a function of linear polarization detection angle (twice the angle of a rotated half-wave plate). The degree of correlation of an unpolarized source can be

obtained directly from the experimental data by $C_{basis} = \left(g^{(2)}_{xx,x} - g^{(2)}_{xx,\bar{x}}\right) / \left(g^{(2)}_{xx,x} + g^{(2)}_{xx,\bar{x}}\right)$, with $xx(x)$ – polarization of a biexciton (exciton) and $\bar{x}$ – orthogonal polarization of an exciton[3]. It varies from -1 to 1, presenting a perfect correlation by 1, a perfect anti-correlation by -1 and no correlation by 0. Similarly as in the section 5.1, it can be shown that for any linear polarization detection angle correlations between co-polarized photons should be maintained. Thus the degree of correlation of an ideal entangled photon source should be unity in the whole range. However, if a FSS is present, the degree of correlation is expected to follow a sinusoidal trend[3,4] with the maximum at the polarization axis of a QD. Such behaviour was observed in the measurement presented in Figure 5.2-1 – the maximum was obtained at ~10˚, while no correlation at ~55˚. The polarization axis value (~20˚) in the current example was obtained from the FSS measurement. The maximum of degree of correlation and the polarization axis values, as expected, are very close.

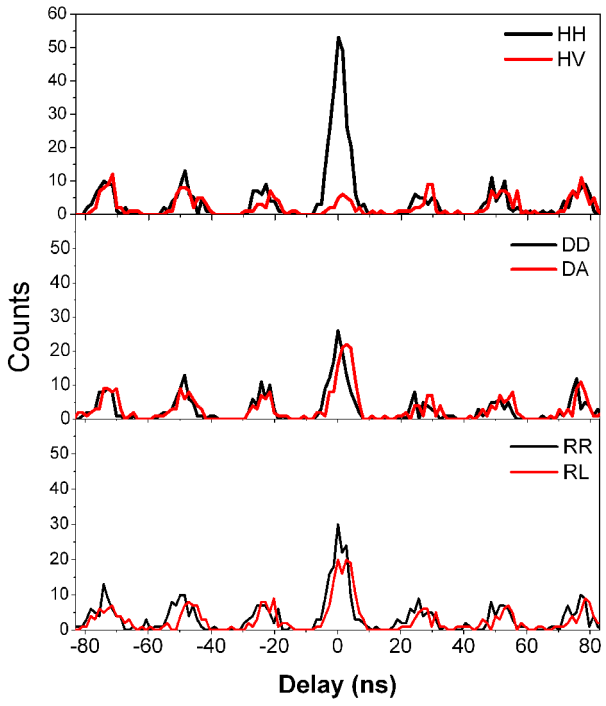


Figure 5.2-2. Polarization resolved the second order correlation functions taken in linear, diagonal and circular bases.

5.3 Selection of QDs

Typically a reliable criterion of potential entangled photon emitters is the measured FSS value. In this work, a vanishing FSS was a necessary condition, however, not sufficient. Interestingly, a number of $In_{0.25}Ga_{0.75}As(N)$ QD samples, especially thinner ones, were fabricated where FSS could not be resolved at all within an overall FSS measurement precision of 4 μeV. However, during the initial attempts no polarization entanglement was measured. After further growth studies and improved post-growth processing procedures, it was observed that all QDs from a single sample could be grouped by their excitonic patterns which appeared to be a key parameter successfully selecting good entangled photon emitters.

QDs could be distinguished by two different types of excitonic patterns which mainly differ in the order of biexciton and charged exciton (the attributed type of transitions is consistent with photon correlation, excitation power dependent, time resolved and temperature dependent measurements). The most widely spread type is presented in Figure 5.3-1. It is the pattern which was nearly almost always observed in our first samples[4] – antibinding biexciton with binding energy in the range of 3-4 meV. Typically there exists a charged exciton between exciton and biexciton (X, X*, XX in energy scale), so that the biexciton binding energy (dE_{xx}) ratio with the charged exciton binding energy (dE_{x*}) $dE_{xx}/dE_{x*} \approx 2$. QDs with this type of pattern have always failed entanglement tests. Moreover, the degree of polarization correlation measurements showed the absence of polarization correlation at all detection angles, possibly explained by a strong exciton spin scattering. For example, a rapid QD feeding from the reservoir of carriers at the vicinity of a QD could be responsible for degrading entanglement, when after the emission of the first biexciton photon, a QD is repopulated with another exciton creating a new biexciton and a new recombination cascade. If such biexciton and exciton from different cascades are detected, their polarization states are not correlated, even though they look like emitted during the same cascade. Indeed, the scenario is possible, as it was discussed in Chapter 4 (section 4.6), feeding of carriers after non-resonant excitation in pyramidal QDs can be strongly pronounced.

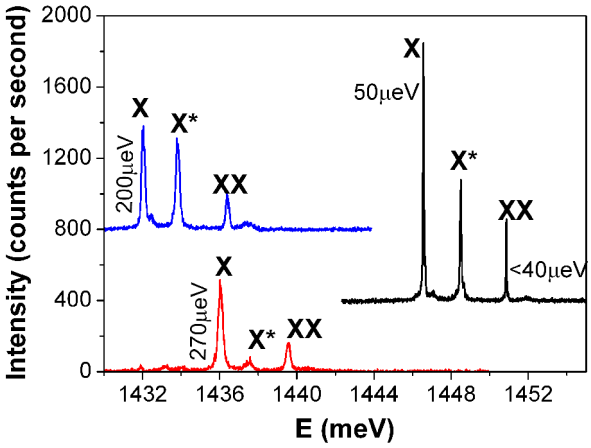


Figure 5.3-1. The typical spectra of QDs that fail entanglement tests (the values in μeV denote the linewidth of the transitions).

In the second QD pattern, biexciton and charged exciton energetic positions were swapped (X, XX, X*) and dE_{xx}/dE_{x^*} typically of ~0.65 – 0.75 (see Figure 5.3-2). The percentage of such QDs typically was 10-20% over the sample. When tested for entangled photon emission, these dots mostly succeeded with fidelities above 0.5. Thus the excitonic pattern was used as a main indicator of potential entangled photon emitters.

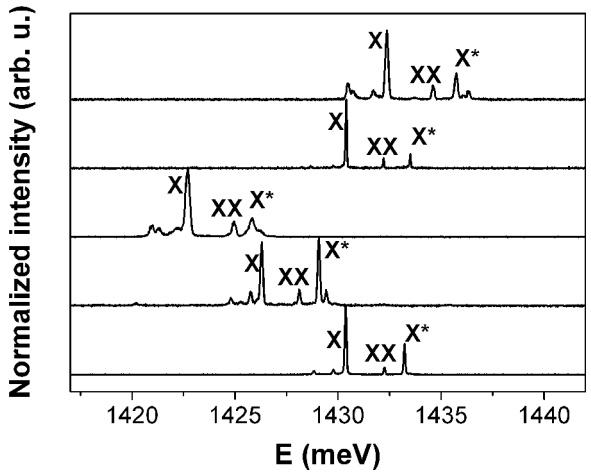


Figure 5.3-2. The typical spectra of entangled photon emitters.

The presence of two dominant excitonic patterns was found to be not a specific property of a single sample design, but a general feature of pyramidal QDs in a relatively broad range of dot shapes and compositions (discussed further). It is worth stressing that no evident transition between the two patterns was observed and

the origin of this phenomenology was not clear at that stage of the study. Meticulous study of the excitonic complexes of both patterns needs to be carried out fully by photon correlation spectroscopy, in the first place. Moreover, as previously discussed, in general an excitonic pattern is very sensitive to various morphological details (e.g., QD size, shape, alloy composition, piezoelectric fields) and can be used as a fingerprint of these properties. While the observation of the two distinct patterns would imply the existence of two different sets of morphological properties, the causes of these differences are not obvious. The systematic study of pyramidal QDs with different structural properties might be useful to test some speculations related to QD geometry and alloy composition. Understanding the origins of this phenomenology is of practical importance and will have to be addressed in the future in order to increase the density of entangled photon emitters.

5.4 Indication of polarization-entanglement

Polarization entanglement was studied using $In_{0.25}Ga_{0.75}As$, 0.8 nm nominal thickness QDs exposed to U-DMHy (the sample S#26). These growth conditions were found to give the best results in the terms of entanglement and QD quality. The spectrum of a representative QD is shown in Figure 5.4-1. The types of excitonic complexes were determined by excitation power dependent measurements (see the top inset in Figure 5.4-1). The bottom inset shows the QD photoluminescence as a function of linear polarization detection angle. Here the QD is shown as a source of unpolarized light. Such property is important as it reduces the experimental efforts to characterize the source of light. In general, precise entanglement measurements, which allow to keep tracking of experimental errors due to sample drifting, excitation power fluctuations, require measurement of a full polarization basis, preferably measured simultaneously[5,6]. For example, to obtain $|HH\rangle$ state intensity, one needs to measure $|HH\rangle$, $|HV\rangle$, $|VH\rangle$ and $|VV\rangle$. However, if the source is unpolarized ($|HH\rangle$ and $|VV\rangle$ intensities are equal), the total number of measurements can be safely reduced twice and only $|HH\rangle$ and $|HV\rangle$ are required. This reduces the complexity of the set-up and problems which might be present due to polarizing effects of such elements as diffraction gratings and others.

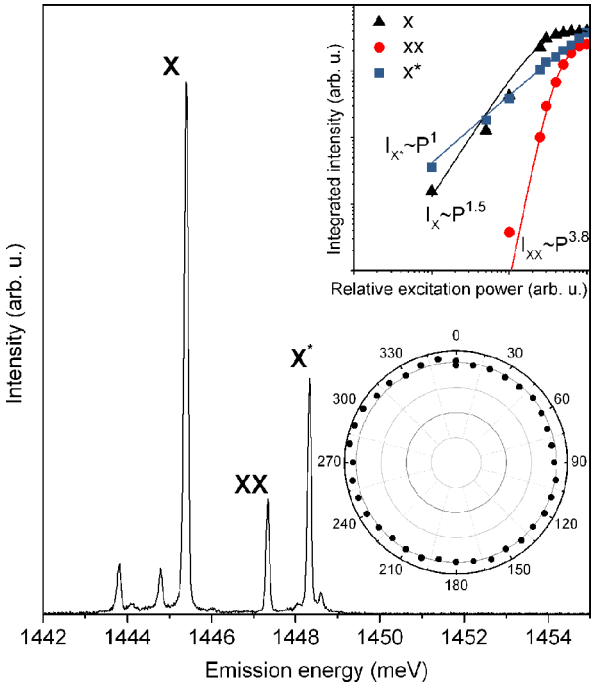


Figure 5.4-1. A typical photoluminescence spectrum of the preselected QDs for the entanglement tests taken at 8K. (Top inset) Power dependence of exciton, biexciton and trion used to select QDs. (Bottom inset) Linear polarization distribution in growth plane.

Figure 5.4-2 illustrates the exciton and biexciton transitions measured at perpendicular linear polarization angles. No visual difference can be identified between the spectra. In the presence of low symmetry (i.e with a FSS), both peaks should be composed of two energetically distinguishable linearly polarized components (typically referred to as *H* and *V*). Here no particular crystallographic direction can consistently be associated with *H* and *V* components, as the origins of the FSS are related to random effects, and not to a shape elongation along certain directions as in self-assembled QDs. *H* and *V* only indicate 0 and 90 deg angles with respect to a linear polarizer. The FSS measurement data presented in the inset confirms that indeed the exciton level splitting is within a 4 μeV error.

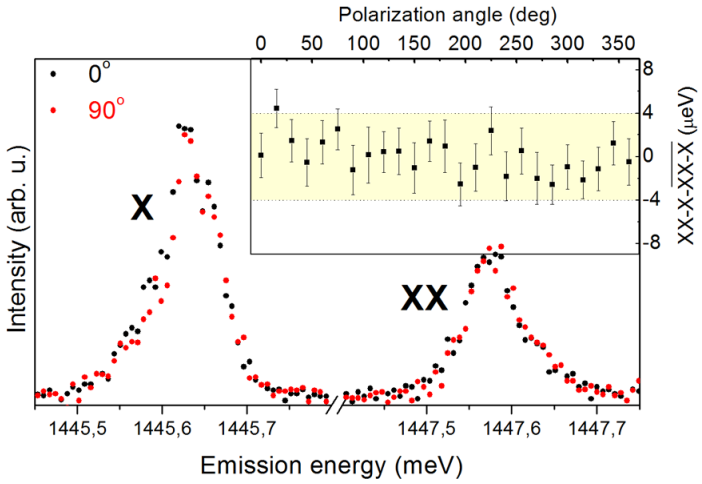


Figure 5.4-2. Representative exciton and biexciton spectra taken at perpendicular linear polarization angles. (Inset) A more precise FSS measurement procedure. Error bars show the standard deviation in the specific measurement, and 4μeV limits (shaded region) represent the typical FSS detection range.

5.4.1 Polarization-resolved second-order correlation functions

A high symmetry of the representative QD was confirmed by polarization-resolved second order correlation measurements. Figure 5.4-3 presents $g^{(2)}(\tau)$ curves measured in linear, diagonal and circular bases. As described in the section 5.1, an expected result is a polarization correlation in linear and diagonal bases between parallel polarization photons, while in circular polarization basis pronounced bunching should be observed between counter-circularly polarized photons. Indeed, these correlations are confirmed by the obtained experimental data. These three measurements are sufficient to calculate fidelity of the expected maximally entangled state $\frac{1}{\sqrt{2}}\left(|HH\rangle+|VV\rangle\right)$, as discussed in the section 5.6. The calculated fidelity value of 0.670±0.035 in this example exceeds the maximum limit of classically correlated light (0.5) by nearly five standard deviations indicating the entangled nature of the emitted photons.

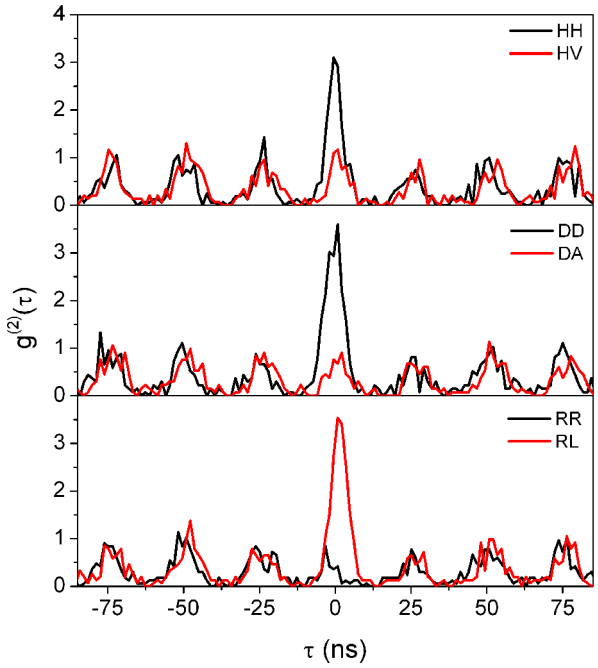


Figure 5.4-3. Polarization-sensitive cross-correlations between biexciton and exciton taken in linear, diagonal and circular polarization bases.

5.4.2 Linear polarization correlations

The entangled nature of photons was confirmed measuring the degree of correlation dependence on a linear polarization basis rotation angle. In contrast to the data presented in Figure 5.2-1, here the degree of correlation does not drop below 0.5 – the top limit for classically correlated photons. The limit value is obtained by averaging all the degree of correlation values over the full rotation period. An average value of 0.56±0.04 is higher than 0.5 in the same range and only possible if the photons are entangled. There might be a number of contributions why it deviates from the ideal case of unity. A slight sinusoidal trend suggests that exciton spin scattering events and a small residual FSS could be responsible for the reduction of degree of correlation values[4].

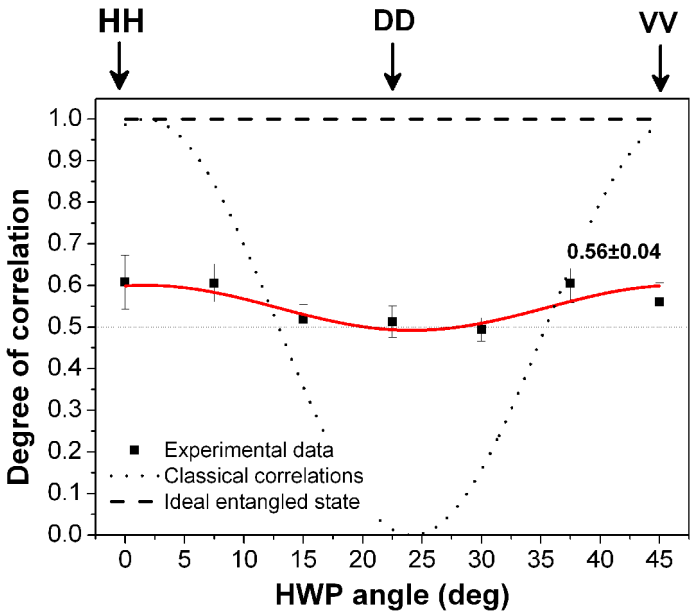


Figure 5.4-4. The degree of correlation as a function of linear polarization detection angle obtained from a QD which does not suffer from FSS related issues.

5.5 Quantum-state tomography

A quantum state tomography procedure is meant to reconstruct the state/ wavefunction of a quantum system in an unknown state. Due to the quantum mechanical nature, a single measurement would give a random result and the wavefunction would be altered, making further measurements useless or impossible. Thus an ensemble of particles prepared in the identical way is required to reconstruct its wavefunction with an acceptable precision. While the state of each particle in the ensemble can be pure, individually they might be very different from each other. The overall state is then not pure, as it is composed of a variety of non-identical states and is referred to as a mixed state. A mixed state can be represented by a density matrix – an incoherent sum of pure states $|\psi_i\rangle$:

$$\rho = \sum_i P_i |\psi_i\rangle\langle\psi_i|, \tag{5.3}$$

where P_i is the probability that the system is in the state $|\psi_i\rangle$ ($\sum_i P_i = 1$).

A two photon state emitted during the biexciton-exciton recombination cascade, in general, is given by[7]:

$$|\psi\rangle = \frac{1}{\sqrt{2}}\left(|HH\rangle + e^{i\cdot FSS\cdot t/\hbar}|VV\rangle\right) . \tag{5.4}$$

The density matrix in *HH*, *HV*, *VH* and *VV* basis is then expressed:

$$\rho = \frac{1}{2}\begin{array}{c} \\ |HH\rangle \\ |HV\rangle \\ |VH\rangle \\ |VV\rangle \end{array}\begin{array}{c} \begin{array}{cccc} \langle HH| & \langle HV| & \langle VH| & \langle VV| \end{array} \\ \begin{pmatrix} 1 & 0 & 0 & e^{-i\cdot FSS\cdot t/\hbar} \\ 0 & 0 & 0 & 0 \\ 0 & 0 & 0 & 0 \\ e^{i\cdot FSS\cdot t/\hbar} & 0 & 0 & 1 \end{pmatrix} \end{array} . \tag{5.5}$$

In the absence of a fine-structure splitting (*FSS*=0), the state is pure, one of the Bell's states. The off-diagonal elements $|HH\rangle\langle VV|$ and $|VV\rangle\langle HH|$ of the density matrix are equal to 0.5 and are indicators of polarization entanglement. On the other hand, if the FSS is big, the overall state would be composed of non-identical pure states with equal probabilities because of the evolving phase term. The off-diagonal elements would be cancelled out in the sum of such states and the density matrix would have an expression equivalent to the one which represents a statistical mixture of $|HH\rangle$ and $|VV\rangle$.

While the quantum state tomography procedure is valid for multiple-qubit systems, the simplest case is a single-photon ensemble polarization state. It is a classic example based on measuring Stokes parameters which can be used to reconstruct a density matrix. The result is achieved by measuring the intensity of 4 polarization projections which are directly related to the Stokes parameters. The procedure to measure a two-qubit (two-photon) polarization state is related. Similarly, the two-qubit state can be obtained from a set of 16 measurements (related to two-photon Stokes vectors). In general, the selection of polarization projections is arbitrary but a well described and documented case[8] was used as a model to build two-photon polarization state density matrix. The selection of polarization bases is achieved by choosing an appropriate combination of a polarizer, half-(quarter-) waveplates oriented at particular angles (see the Table 1).

Table 1. The orientation of half- and quarter-wave plates used to obtain state intensities used for quantum state tomography procedure (bold). Redundant measurements were used for normalization.

	BASIS	HWP1	HWP2	QWP
1.	**HH**, **HV**,**VV**, **VH**	0	0	X
2.	**DD**, DA, AA, AD	22.5	22.5	X
3.	RR, **RL**, LL, LR	X	X	-45
4.	**RD**, RA, LA, LD	0	22.5	-45
5.	**DR**, DL, AL, AR	22.5	0	-45
6.	**RH**, **RV**, LV, LH	22.5	0	0
7.	**HL**, HR, VR, **VL**	0	-22.5	0
8.	**DH**, **DV**, AV, AH	22.5	0	X
9.	**HD**, HA, VA, **VD**	0	22.5	X

In principle, the measured second order correlation values could be used directly as the intensity of each corresponding state. However, measuring redundant correlations simultaneously (a full polarization basis, such as *DD, DA, AA* and *AD*) can be beneficial tracking experimental errors and thus making the experiment more precise. If only total 16 measurements are used, the sum of the state intensities in linear basis is used to normalize (convert to probabilities) the states in other bases. It comes from the fact that the total intensity in all the bases ideally must be the same (e.g., *HH+HV+VV+VH = RD+RA+LA+AR*). However, the measurements are long and sample drifting along with excitation intensity fluctuations can take place. Without taking a full polarization basis simultaneously (or at least half, if the source is unpolarized) there is no way to tell if the change of the state intensity is an intrinsic property or caused by the experimental imperfections. Measuring each basis simultaneously helps to track these changes and reduce the effects caused[9]. The redundant measurements are used to normalise the state by expressing it in the form of a probability (e.g., $P_{DD} = g^{(2)}_{DD} / \left(g^{(2)}_{DD} + g^{(2)}_{DA} + g^{(2)}_{AA} + g^{(2)}_{AD} \right)$). The measured state intensities are shown in the Table 2.

Table 2. State intensities used in quantum state tomography procedure.

HH	0.364008	**DR**	0.284365
HV	0.135992	**DD**	0.345358
VV	0.352098	**RD**	0.204577
VH	0.147902	**HD**	0.310238
RH	0.164326	**VD**	0.184296
RV	0.335674	**VL**	0.331001
DV	0.293546	**HL**	0.183921
DH	0.206454	**RL**	0.383645

The obtained density matrix (the equation 5.6) is plotted in Figure 5.5-1. The presence of non-zero outer elements $|HH\rangle\langle VV|$ and $|VV\rangle\langle HH|$ in the minor diagonal exceeding $|HV\rangle\langle HV|$ and $|VH\rangle\langle VH|$ is a signature of entanglement. The presence of $|HV\rangle\langle HV|$ and $|VH\rangle\langle VH|$ elements is mainly because of the exciton spin-scattering events[2].

$$\rho = \begin{pmatrix} 0.364 & 0.060 & -0.05 & 0.224 \\ 0.060 & 0.136 & -0.028 & 0.05 \\ -0.050 & -0.028 & 0.148 & -0.066 \\ 0.224 & 0.05 & -0.066 & 0.352 \end{pmatrix} + i \begin{pmatrix} 0 & -0.066 & 0.092 & 0.001 \\ 0.066 & 0 & 0.085 & -0.092 \\ -0.092 & -0.085 & 0 & 0.081 \\ -0.001 & 0.092 & -0.081 & 0 \end{pmatrix} \quad (5.6)$$

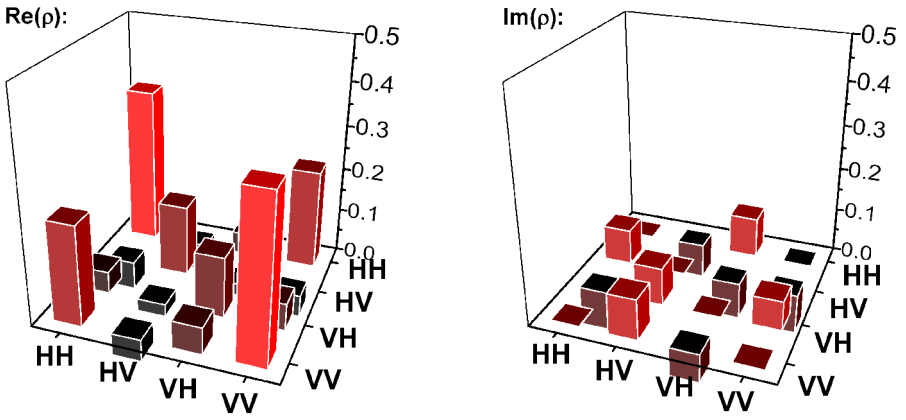


Figure 5.5-1. The density matrix reconstructed by a quantum state tomography procedure.

The density matrix can be used to evaluate entanglement of the source by calculating the specific parameters, such as fidelity F, concurrence C (Ref. 10), tangle $T=C^2$ (Ref. 11), the Peres criterion[12] and linear entropy[13]. QLIB (Quantum Information computation library, v1.0) software packet was used to calculate the parameters. The obtained values confirmed the entanglement: F=0.582±0.031 (>0.5), C=0.158±0.020 (>0), T=0.025±0.020 (>0), Peres criterion -0.119±0.035 (<0) and linear entropy 0.674 (1 is a totally mixed state).

5.6 Fidelity

The state overlap (closeness to the ideal entangled state $|\psi\rangle$) is measured by the fidelity:

$$F = \langle\psi|\rho|\psi\rangle. \tag{5.3}$$

The fidelity can vary from 0 to 1 – the value of maximally entangled state. The top limit of classically correlated light is 0.5 and the value above that indicates non-classical state.

If the state is $|\psi\rangle = \frac{1}{\sqrt{2}}(|HH\rangle + |VV\rangle)$, then $F = (a_{11} + a_{44})/2 + \mathrm{Re}(a_{14})$, where $a_{x,y}$ is the density matrix element from the *x*-th row and *y*-th column. When the source is non-polarized, $a_{11} = a_{44}$ and the expression of fidelity can be simplified to $F = a_{11} + \mathrm{Re}(a_{14})$. The two density matrix elements can be expressed by three degrees of correlation C_{basis} measured only in three polarization bases (linear, diagonal and circular)[14,15]:

$$F = (1 + C_L + C_D - C_C)/4, \tag{5.4}$$

where $C_{basis} = (g^{(2)}_{xx,x} - g^{(2)}_{xx,\bar{x}})/(g^{(2)}_{xx,x} + g^{(2)}_{xx,\bar{x}})$. The fact that measurements only in three bases are required to test entanglement greatly simplifies the whole procedure.

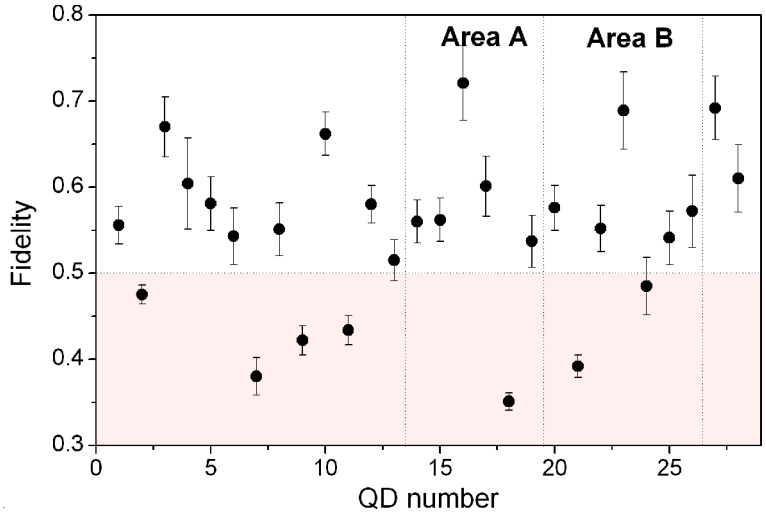


Figure 5.6-1. Fidelity distribution of all pre-selected QDs.

Figure 5.6-1 shows the distribution of measured fidelity values of 28 QDs. 75% of the dots passed the limit of 0.5 imposed by classically correlated light. The highest obtained value was 0.721±0.043. The QDs were preselected by the criterion of the PL spectrum which indeed appeared as a very good indicator of entangled photon emitters. Closer analysis of these QDs showed that there is no other correlation between the fidelity value and other properties such as emission energy (Figure 5.6-2) or biexciton binding energy of QDs from this sample.

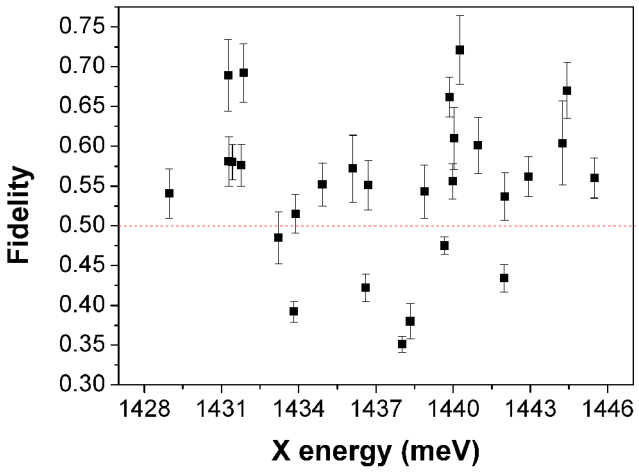


Figure 5.6-2. Fidelity dependence on exciton ground state emission energy.

5.7 High density of emitters

Selection of naturally 'good' entangled photon emitters even in the best self-assembled QD systems usually is a complicated task. While some particular pre-selection rules can be applied (e.g., emission energy[16,17]), eventually, only one in a few hundred or thousand candidates are found as suitable. Such low density is in a great contrast with the results obtained in this work. Figure 5.7-1 consists of the two images obtained by the sample surface imaging system of two randomly selected areas (noted as A and B). Green spots indicate QDs that have fidelity of the entangled state >0.5, while the red ones ≤0.5. In the both cases, the percentage of QDs with fidelity >0.5 is at least 15% of the overall QD field. Such high concentration of QDs emitting entangled photons corresponds mostly to those sample areas where the substrate was not fully removed during the back-etching procedure. The density of QDs emitting polarization-entangled photons drops in the

central areas (where the full substrate removal procedure was more effective), probably due to the prolonged etching which might have degraded the QD quality. This assumption is supported by the fact that better statistics of entangled photon emitters' distribution in the central area was achieved in a successful reproduction of the sample.

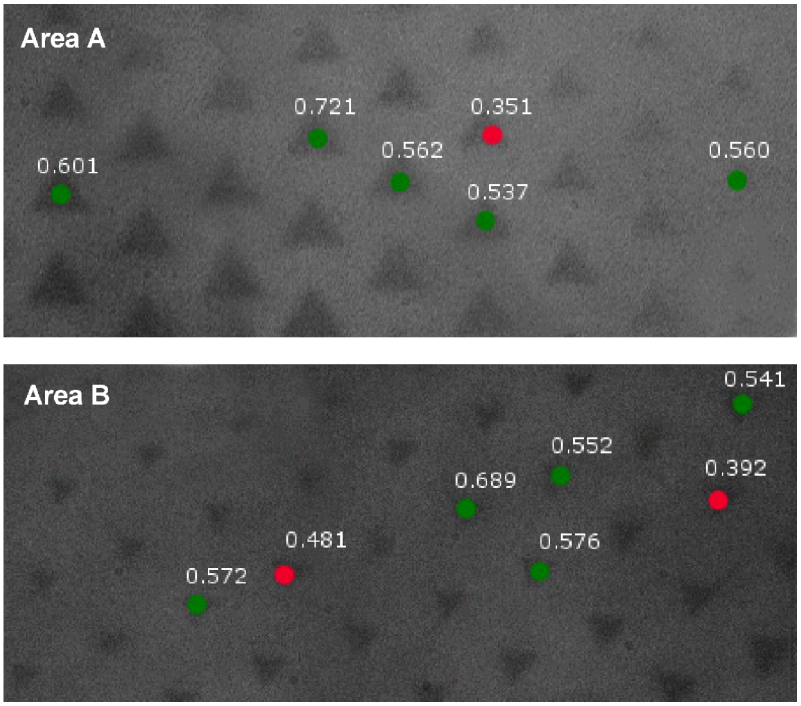


Figure 5.7-1. Mapping of entangled photon emitters on two randomly selected areas of the sample. Green spots indicate entangled photon emitters with fidelity values.

5.8 Entangled photon emitters grown at different conditions.

The presented results were achieved with QDs exposed to U-DMHy by exploiting the surfactant effects. A number of $In_{0.25}Ga_{0.75}As$ QD samples were grown in order to test the necessity of this growth step. The growth conditions (nominal thickness, growth temperature) are presented in Table 3. The spectral purity is identified by the best found linewidth *w* of the exciton transition (the best linewidth in QDs exposed to UDMHy was found to be 60 μeV).

Table 3. Growth parameters and conditions of the studied samples with $In_{0.25}Ga_{0.75}As$ QDs emitting entangled photons

#	h, nm	T, ˚C	w, μeV	Sample notation
1	0.5	640	62	S#25
2	0.5	700	92	S#23
3	0.5	730	115	S#16
4	0.57	730	75	S#14
5	0.8	730	70	S#18

QD photoluminescence was tuned in the range of ~80 meV because of the various growth conditions. Most importantly, it was possible to find QDs with the excitonic pattern used as the pre-selection criterion for entanglement tests. It should be said that, in all cases, all found QDs emitting entangled photons represent the minority of overall QDs, and none of these samples reach the high density of good emitters as in the samples exposed to UDMHy. The representative spectra of all five samples are shown in Figure 5.8-1. All but the sample #1 showed a clear excitonic pattern, with an antibinding exciton and an intense charged exciton line at higher energies (X* in the figure), i.e. the biexciton (XX) is in-between the exciton (X) and charged exciton (X*) lines. This is less evident in the sample #1, grown at low(er) temperature, where the charged exciton line is not so intense and binding energies span a broader interval than in the other samples. Nevertheless, the search for good entangled emitters was facilitated exactly because of this peculiar excitonic pattern.

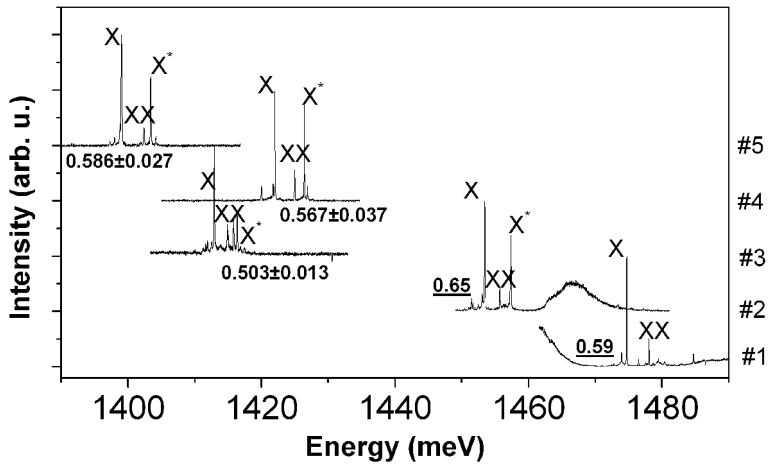


Figure 5.8-1. Spectra of QDs emitting entangled photons from five different samples grown at the conditions and with parameters specified in table 1. Numbers below/aside the spectra represent fidelity values of the expected maximally entangled state for the samples #3-5, and the maximum fidelity value measures in continuous wave for samples #1-2.

The fidelity values of the expected maximally entangled state are presented below the corresponding spectra of samples #3, #4 and #5. The highest value was found to be 0.586±0.027. The samples #1 and #2 in pulsed excitation mode have been revealed to be more troublesome, because of the pronounced QD repopulation effects which caused broadening and merging of the correlation peaks. Continuous-wave excitation allows to avoid these effects, however, true deterministic (on demand) entangled photon generation is not possible anymore. The measurements obtained in *cw* excitation mode are presented in Figure 5.8-2. Here transient fidelity $F(\tau)=(1+C_L(\tau)+C_D(\tau)-C_C(\tau))/4$ is presented. The maximum obtained value was 0.59.

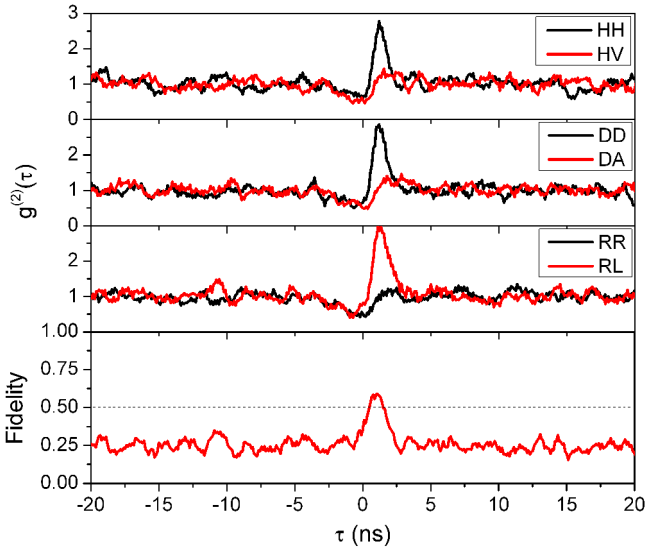


Figure 5.8-2. Continuous wave polarization resolved second-order correlation curves taken in linear, diagonal and circular bases. Fidelity vas calculated using these curves and the maximum value was found to be 0.59, indicating polarization entanglement (>0.5).

It can be noted that the FSS of a few μeV started to be measurable in thicker QDs, particularly in the sample #5. This could be related to the changes in the confinement. The dots emitting at higher energy are thought to be weaker confined, and the excitonic wavefunctions can leak more easily into the barriers. The electron-hole exchange interaction in such QDs is smaller and thus the FSS. This is one of the arguments explaining the correlation between reduced FSS and emission energy in SK QDs[17,18], even though the phenomena is not that highly pronounced in an already intrinsically highly symmetrical pyramidal QD system.

5.9 Summary

Pyramidal QDs were found as sources of polarization-entangled photons. This is the first time that entangled photon emission has been demonstrated from site-controlled QDs in general. The highest fidelity of the expected maximally entangled state was found to be 0.721±0.043. The density of entangled photon emitters in some regions was as high as 15%. This is a substantial improvement compared to any other QD system. The best results in the terms of fidelity values and QD density were achieved from the samples exposed to unsymmetrical dimethylhydrazine which probably acted as a surfactant improving QD alloy uniformity. Entangled photon emission was measured from regular InGaAs QDs grown at various different conditions (growth temperature, QD thickness) as well. This result confirms that the production of entangled photon emitters is not limited to a single set of growth parameters and conditions.

Bibliography

[1] R. J. Young, R. M. Stevenson, P. Atkinson, K. Cooper, D. A. Ritchie, and A. J. Shields, New Journal of Physics 8, 29 (2006).

[2] A. J. Hudson, R. M. Stevenson, A. J. Bennett, R. J. Young, C. A. Nicoll, P. Atkinson, K. Cooper, D. A. Ritchie, and A. J. Shields, Phys. Rev. Lett. **99**, 266802 (2007).

[3] R. M. Stevenson, R. J. Young, P. Atkinson, K. Cooper, D. A. Ritchie, and A. J. Shields, Nature 439, 179 (2006).

[4] L. Q. Yuan and S. Das, Physical Review A 83, 063819 (2011).

[5] J. B. Altepeter, E. R. Jeffrey, and P. G. Kwiat, "Photonic State Tomography," Advances In Atomic, Molecular, and Optical Physics 52, 105 (2005).

[6] A. Gilchrist, K. J. Resch, and A. G. White, Nature 445, E4 (2007).

[7] R. M. Stevenson, A. J. Hudson, A. J. Bennett, R. J. Young, C. A. Nicoll, D. A. Ritchie, and A. J. Shields, Phys. Rev. Lett. 101, 170501 (2008).

[8] D. F. V. James, P. G. Kwiat, W. J. Munro, and A. G. White, Physical Review A 64, 052312 (2001).

[9] T. Kuroda, et al., Phys. Rev. B 88, 041306 (2013), supplementary material.

[10] S. Hill and W. K. Wootters, Phys. Rev. Lett. 78, 5022 (1997).

[11] R. Hafenbrak, S. M. Ulrich, P. Michler, L. Wang, A. Rastelli, and O. G. Schmidt, New Journal of Physics 9, 315 (2007).

[12] A. Peres, Phys. Rev. Lett. 77, 1413 (1996).

[13] E. Santos and M. Ferrero, Physical Review A 62, 024101 (2000).

[14] A. J. Hudson, thesis 'Polarisation-entangled photon pairs from the quantum dot biexciton cascade', (2008).

[15] A. Shields, R. M. Stevenson, and R. Young, in Single Semiconductor Quantum Dots, edited by P. Michler (Springer Berlin Heidelberg, 2009), p. 227.

[16] R. Seguin, A. Schliwa, S. Rodt, K. Potschke, U. W. Pohl, and D. Bimberg, Phys. Rev. Lett. 95, 257402 (2005).

[17] R. J. Young, R. M. Stevenson, A. J. Shields, P. Atkinson, K. Cooper, D. A. Ritchie, K. M. Groom, A. I. Tartakovskii, and M. S. Skolnick, Phys. Rev. B 72, 113305 (2005).

[18] R. M. Stevenson, R. J. Young, P. See, D. G. Gevaux, K. Cooper, P. Atkinson, I. Farrer, D. A. Ritchie, and A. J. Shields, Phys. Rev. B 73, 033306 (2006).

Chapter 6

6 Magneto-photoluminescence

The magneto-optical properties of quantum dot structures present in pyramidal recesses were measured in Cambridge Cavendish Laboratory using the magneto-photoluminescence set-up described in Chapter 2. The Interpretation of the results is consistent with the existence of lateral quantum dots. Moreover, an unusual, however, theoretically expected and, in some cases, already observed excitonic state splitting of the main QD in the magnetic field is presented.

6.1 Nanostructures in the magnetic field

The properties of excitons in nanostructures can be probed by an external perturbations such as magnetic field. There are two main, simultaneously present effects on the energetic structure of a nanostructure placed in a magnetic field: (1) the splitting of energy levels which depends on the configuration of particle spins, magnetic field orientation, etc. (spin or Zeeman splitting) and (2) the diamagnetic shift – the energy increase of the split lines which is quadratic with the magnetic field. The ground state exciton energy can be usually approximated at low magnetic field as

$$E(B) = E_0 \pm \tfrac{1}{2} g_{ex} \mu_B B + \gamma_d B^2, \tag{6.1}$$

where E_0 is the energy of exciton at zero field, g_{ex} is the g-factor of exciton, μ_B is the constant of Bohr magneton and γ_d is the diamagnetic coefficient. The second term represents Zeeman splitting, while the last one – the diamagnetic shift.

The diamagnetic shift is the result of the interaction between the external magnetic field and the orbital momentum of an electron or a hole orbiting in the crystal. The diamagnetic shift can be approximated to

$$\gamma_d \sim \frac{\langle r^2 \rangle}{m^*}, \tag{6.2}$$

where $\langle r^2 \rangle$ is the lateral extension of the wavefunction in the direction perpendicular to the magnetic field, and m^* is the effective mass[1]. The relation suggests that γ_d is

the most prominent for flat structures[2]. Such sensitivity of γ_d to the extension of the wavefunction can be used to map it with the type of the setup used in this work.

The second phenomenon, Zeeman effect, occurs when the magnetic moment μ_s of the particle spin interacts with the external magnetic field. The interaction causes the splitting between spin-up and spin-down particle states. In general, the magnetic moment of a free particle with the charge of q is:

$$\overrightarrow{\mu_s} = g\frac{q}{2m}\vec{S}, \tag{6.3}$$

where g is the gyromagnetic factor (g-factor) – the dimensionless magnetic moment. Zeeman Hamiltonian is expressed as

$$H_{Zeeman} = -\vec{\mu}_s \vec{B}. \tag{6.4}$$

Zeeman interaction affects both, electrons and holes, present in the crystal[3]. The contribution of the Zeeman interaction to the fine-structure of an exciton in a QD with the symmetry of D_{2d} and lower can be shown by following the theoretical framework presented by Bayer *et al.*[4]. There are two main configurations of the QD growth plane orientation and the magnetic field. The first one, Faraday configuration, is when the magnetic field is perpendicular to the QD growth plane. The second one, Voigt configuration, is achieved when the magnetic field is parallel to the growth plane.

Using exciton states $|+1\rangle, |-1\rangle, |+2\rangle, |-2\rangle$ as basis, The Hamiltonian describing the Zeeman interaction in Faraday configuration is expressed as

$$H_{Zeeman}^{F} = \frac{\mu_B B_z}{2}\begin{pmatrix} (g_{e,z}+g_{h,z}) & 0 & 0 & 0 \\ 0 & -(g_{e,z}+g_{h,z}) & 0 & 0 \\ 0 & 0 & -(g_{e,z}-g_{h,z}) & 0 \\ 0 & 0 & 0 & (g_{e,z}-g_{h,z}) \end{pmatrix}, \tag{6.5}$$

where $g_{e,z}$ and $g_{h,z}$ are electron and hole g-factors along the growth axis z. The total Hamiltonian of the system is obtained by adding the exchange Hamiltonian H_{ex} (Equation 1.1) to H_{Zeeman}^{F}. If the system is symmetric ($|+1\rangle, |-1\rangle$ are the eigenstates at zero magnetic field), the spin splitting between the bright states increases linearly with the magnetic field (the second term in the equation 6.1). If the system has lower

symmetry than D_{2d}, the bright states are mixed and off-diagonal elements in the bright state subblock (Equation 1.7) are present. This causes a quadratic spin-splitting dependence of the bright states at low fields and a linear one at high fields as the elements of H^{F}_{Zeeman} become dominant. The dark states are not predicted to be observed in QDs with the symmetry of D_{2d} and lower, unless the symmetry is very strongly broken. However, the theoretical analysis of QDs with the high rotational symmetry of C_{3v} (in fact, any threefold symmetry which lacks mirror-reflection symmetry in *z*-direction) confirmed by experimental observations showed that even at small magnetic fields the hole states $\left|+\tfrac{3}{2}\right\rangle$ and $\left|-\tfrac{3}{2}\right\rangle$ are mixed[5,6]. The hole mixing causes mixing of the dark and bright states which, all four, are visible in Faraday geometry: it is not the consequence of very low symmetry but an intrinsic property of C_{3v} symmetry. It was shown that the spin splitting can be strongly nonlinear.

The Hamiltonian in Voigt configuration when the magnetic field is oriented along *x* axis is expressed as

$$H^{V}_{Zeeman,x} = \frac{\mu_B B_x}{2}\begin{pmatrix} 0 & 0 & g_{e,x} & g_{h,x} \\ 0 & 0 & g_{h,x} & g_{e,x} \\ g_{e,x} & g_{h,x} & 0 & 0 \\ g_{h,x} & g_{e,x} & 0 & 0 \end{pmatrix}. \tag{6.6}$$

The matrix has off-diagonal elements which indicate that previously bright and dark states are mixed because of the in-plane magnetic field and four optically active transitions are observed in the spectrum. Initially dark and bright states are observed in the PL of C_{3v} symmetry QDs[6], however, both transitions are composed of overlapping linearly co-polarized components.

6.2 Probing lateral quantum dots

Both quantum dot features, lateral QDs and highly symmetrical central QDs, were studied in the magnetic field. To study LQDs, the same sample S#3 ($In_{0.25}Ga_{0.75}As$, 0.5 nm thickness) as in the Section 3.9 was selected. Figure 6.2-1 presents the evolution of the LQD exciton and biexciton peaks with magnetic field at the angles of 0˚ (Faraday geometry), 54˚ and 90˚ (Voigt geometry). In both, Faraday and Voigt, geometries, due to the Zeeman effect, the transition lines split into four

lines at higher field, while at 54˚ only a doublet was visible up to 10 T. The result can be explained, if the previous observations about LQDs are taken into account. According to the theoretical analysis established for QDs with D_{2d} (or lower) symmetry and the experimental observations, the optical transitions typically split into counter-circularly polarized doublet in Faraday geometry, while in Voigt geometry, due to mixing of the two bright and the two dark states (the latter become optically active) four states are visible in the optical spectra. Observing four peaks in Faraday geometry in this theoretical framework is only possible if a QD is highly asymmetric or if its plane is tilted to the respect of the magnetic field. The latter is the case for LQDs which are located along LQWRs.

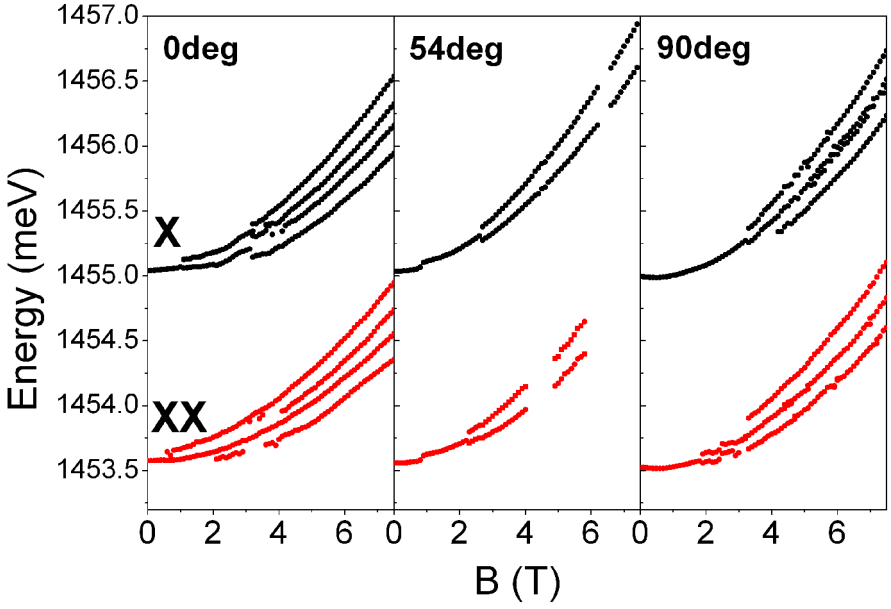


Figure 6.2-1. Evolution of LQD exciton and biexciton photoluminescence splitting in the magnetic field taken at different angles between magnetic field and growth direction (0˚, 54˚ and 90˚).

Ideally, there exist two particular combinations of a pyramid orientation and location of a LQD in the measurement set-up, when a LQD plane can be oriented either perpendicular to the magnetic field (Faraday geometry) or along it (Voigt geometry), provided that the rotation is in the plane perpendicular to the growth plane and a LQWR with a LQD of interest is in that plane (see Figure 6.2-2 (a) and (b)). To choose an appropriate combination, one needs to know the exact location of a LQD, which unfortunately could not be the case during the measurements. Due to the complexity of the system, the optical visualization of the sample was not

available. However, by interpreting Zeeman splitting and diamagnetic shift results (see Figure 6.2-3), it can be assumed that at least in two cases both configurations were achieved. Observing the doublet at 54˚, would match conventional Faraday geometry as presented in Figure 6.2-2 (a). This assumption is supported by analyzing the tilt angle dependent diamagnetic coefficient data (Figure 6.2-3(c)).

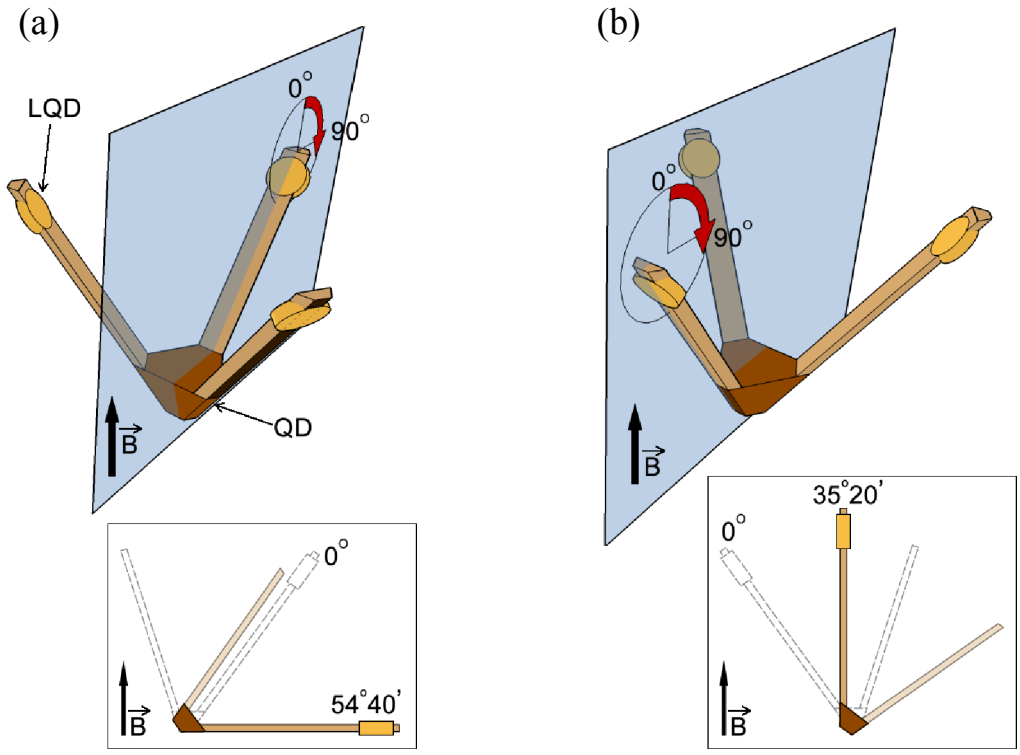


Figure 6.2-2. The sketches of possible orientations of the ensemble of nanostructures in the experimental set-up to place a particular LQD in a conventional (a) Faraday or (b) Voigt geometries.

Since the diamagnetic coefficient is proportional to the normal extension of the exciton wavefunction (Equation 6.2), the highest diamagnetic shift values for the flattened QDs are expected at Faraday geometry. Indeed, the highest diamagnetic coefficient (32.9 μeV/T^2) in the LQD presented in Figure 6.2-1 was obtained at 54˚ when it split into a doublet. Another representative LQD demonstrated an opposite results – splitting to four lines was observed at all tilt angles and the minimum of diamagnetic coefficient (15.1 μeV/T^2) was obtained at ~40˚, suggesting orientation of Voigt geometry as depicted in Figure 6.2-2 (b). The large values of the diamagnetic coefficient observed could be related to a significant extension of the

exciton wavefunction, thus it is not surprising that due to a weak electron-hole exchange interaction fine-structure splitting values were typically small and the "dark" states were observed emerging virtually from the same energetic point.

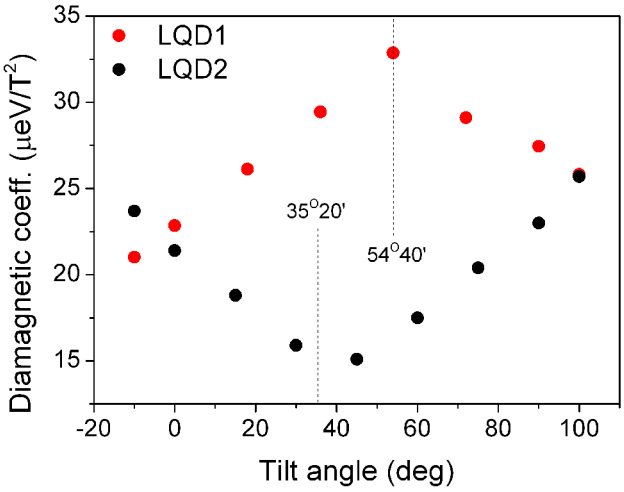


Figure 6.2-3. Diamagnetic coefficient dependence on rotation (tilt) angle obtained for two LQDs. Both trends presumably match situations shown in Figure 6.2-2 (a) and (b).

6.3 Probing central QDs

The magneto-optical properties of highly symmetric central QDs were studied as well. A replica of the sample containing high density of entangled photon emitters presented in the Chapter 5 ($In_{0.75}Ga_{0.25}As_{1-\delta}N_{\delta}$ QDs, the sample S#27) was chosen. The selection of the representative QD was based on the excitonic pattern criterion (X, XX, X+) as discussed previously. Magneto-photoluminescence was collected at 5 different tilt angles: 0°, 30°, 54°, 72° and 90°, in the range of the magnetic field between 0 and 10 T. Figure 6.3-1 shows the set of spectra taken at 0° and 90°, which conventionally correspond to Faraday and Voigt configurations. A clear spin-splitting to four spectral lines of exciton, biexciton and trion was observed in all but the Voigt configurations. The biexciton is spin neutral and its Zeeman interaction with the magnetic field is absent[7,8]. The splitting of biexciton reflects only the spin-splitting of its ground state which is an exciton. Thus in the further representation of the results and discussion, the concentration is mainly on the neutral exciton transition.

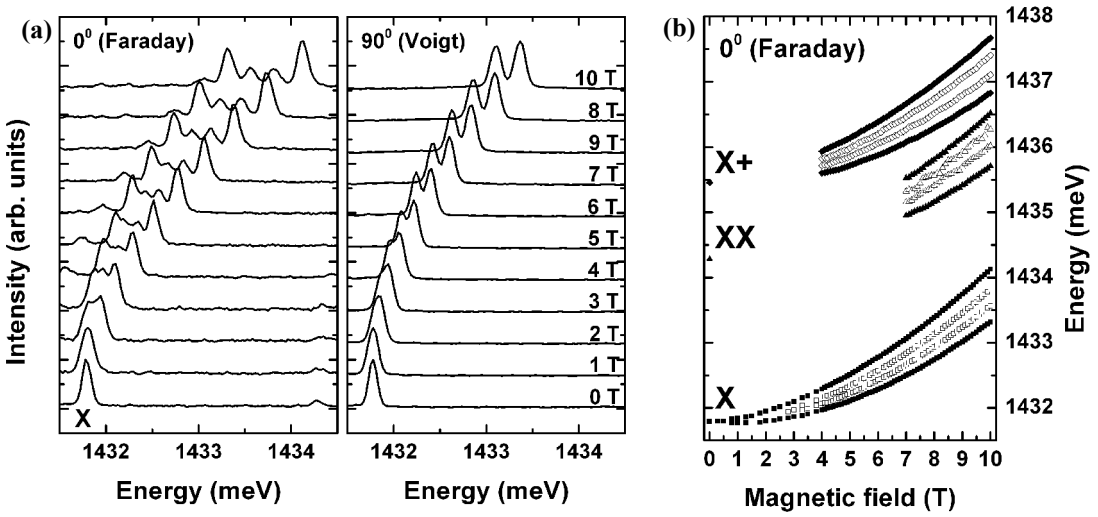


Figure 6.3-1. (a) Zeeman splitting of exciton in Faraday and Voigt configurations. (b) Zeeman splitting of exciton, biexciton and trion.

A splitting to four lines in the magnetic field oriented along the growth axis is an unusual phenomenon in QD physics which typically deals with QDs grown on (001) oriented surfaces and have the symmetry of D_{2d} or lower. On the other hand, a very similar spin-splitting scenario was already observed in QDs grown by droplet epitaxy on (111) oriented surfaces and which can have the threefold rotational symmetry C_{3v} (Refs. 5,6). The atypical splitting to four lines was explained by the mixing of the hole states $\left|+\tfrac{3}{2}\right\rangle$ and $\left|-\tfrac{3}{2}\right\rangle$ in the magnetic field along [111] direction, and splitting to two lines in Voigt geometry as a consequence of the absence of this mixing. Such Zeeman splitting was concluded to be the intrinsic property of QDs with the C_{3v} symmetry grown along [111] direction. Indeed, the observed results are in agreement with these conclusions. A reliable confirmation and comparison could be made with polarization resolved measurements which could reveal optical selection rules valid for particular spin configurations[4]. Unfortunately, such option was not available during the measurement session, thus the attribution of the spectral lines to dark and bright exciton states are based on other arguments. Typically the dark states are at lower energy separated by the electron-hole exchange interaction splitting δ_0 which is typically in the order of a few hundred μeV in self-assembled QDs. When the magnetic field mixes bright and dark states, the latter emerge as a doublet below the doublet of the bright states. However, this argument without any

data analysis with theoretical fittings was not obvious, as all four transitions were emerging from the close energy points. It is an expected result in trions where e-h exchange interaction is not present at all. On the other hand, a strong reduction of e-h exchange interaction was observed and predicted theoretically in large QDs[4] – for example, in a self-assembled QD of $In_{0.60}Ga_{0.4}As$ alloy composition and 70 nm diameter (value close to the one of the studied pyramidal QDs), δ_0 was estimated to be ~20 μeV. The other argument to distinguish between dark and bright states is their intensity. The initially dark states tend to be less intense. It was observed that the lifetime of a neutral exciton dark states is a few times longer and decreases with the increasing magnetic field, while the bright states tend to decay slower with increasing magnetic field[9]. Naturally, the states which have higher contribution from the dark states are less intense in the continuous-wave excitation spectra. Because of this, the less intense inner doublet in Faraday configuration (Figure 6.3-1) was attributed to the dark states. They are marked by open symbols in Figure 6.3-2. In Voigt geometry, the attribution of the lower energy line to the dark states was solely based on the model proposed by Durnev *et al*.[6] where both spin states of the dark and bright levels are nearly degenerate.

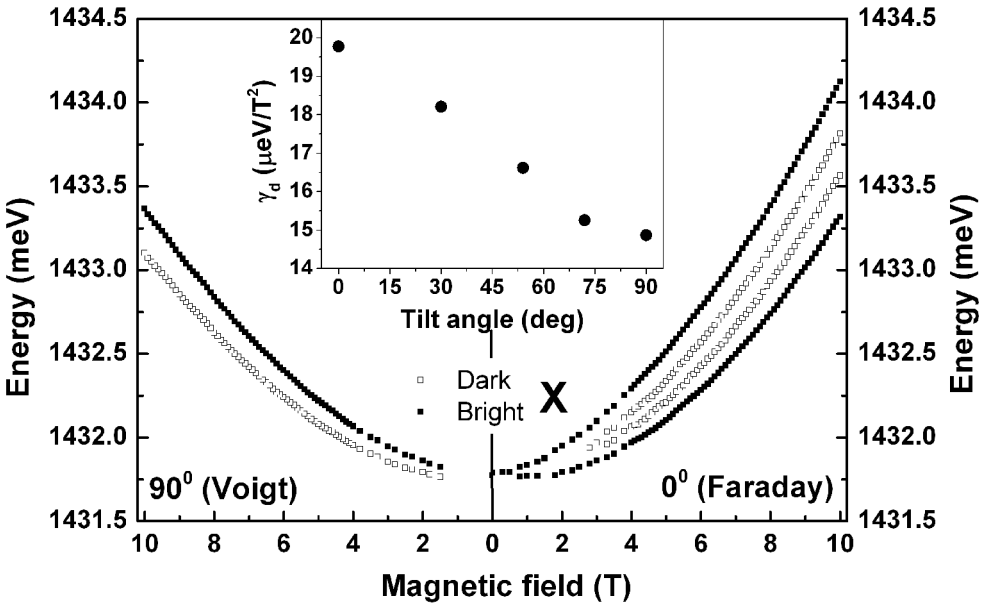


Figure 6.3-2. Exciton transition energies parallel and perpendicular magnetic field. (Inset) Diamagnetic coefficient as function of the tilt angle.

The spin splitting (the difference between the peaks of each doublet) dependence on the magnetic field in Faraday geometry is shown in the inset of Figure 6.3-3. Very clear linear behaviour was obtained which suggests that the equation 6.1 is a good approximation of the emission energy. Exciton g-factors g_{ex} and diamagnetic shift γ_d values were obtained from the fittings (an example is shown in Figure 6.3-3). The diamagnetic shift trend is shown in the inset of Figure 6.3-2. As expected, the highest value (19.8 μeV/T^2) was obtained at 0° when the lateral extension of the exciton wavefunction is the biggest. It gradually decreases and reaches minimum (14.9 μeV/T^2) in Voigt geometry. The diamagnetic coefficient values obtained from both, bright and dark, transitions are nearly identical.

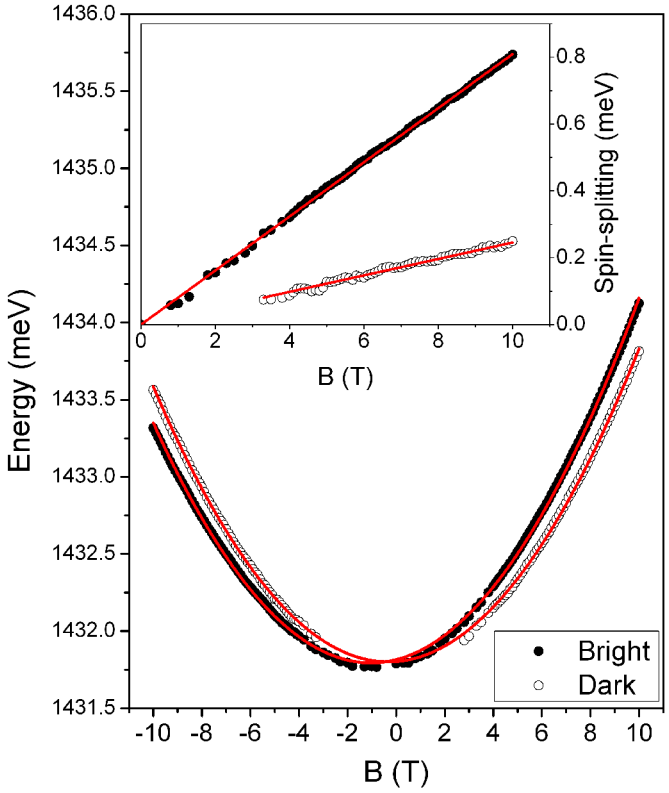


Figure 6.3-3. Analysis of exciton dark and bright states by fitting equation 6.1. (Inset) Magnetic-field dependence of the exciton spin-splitting.

The absolute value of exciton g-factor in Faraday configuration was found to be $|g_{ex}|_{M=\pm1} = 1.4$ and $|g_{ex}|_{M=\pm2} = 0.42$. g_{ex} can be defined by the relation given as[10,11]

$$g_{ex} = \frac{E(\sigma^+) - E(\sigma^-)}{\mu_B B}, \tag{6.7}$$

where σ^+ and σ^- are right- and left-hand circularly polarized light. The measurements were not polarization resolved, thus only absolute values could be obtained. In general, g_{ex} is composed of g-factors of electron and hole – g_e, g_h [12]:

$$\begin{aligned} g_{ex}\big|_{M=\pm1} &= |g_e + g_h| \\ g_{ex}\big|_{M=\pm2} &= |g_e - g_h| \end{aligned}. \tag{6.8}$$

The calculated g-factor values were found to be $|g_e| = 0.49$ and $|g_h| = 0.91$.

While exchange interaction splitting δ_0 is not obvious from the spectra, its value was obtained from the fittings: $\delta_0 = E_0\big|_{M=\pm1} - E_0\big|_{M=\pm2}$. The measured value of this representative QD was found to be ~35 μeV – 5-10 times smaller than in self-assembled QDs. Typically the fine-structure splitting values of bright and dark states are significantly smaller than e-h exchange interaction[4]. This explains why the fine-structure splitting values bigger than 4 μeV consistently were not measured in an absolute majority of QDs from different samples. Indeed, very long QD base (~70 nm) could be an important factor which positively contributes to the intrinsic high rotational symmetry properties.

Other central QDs (with different excitonic patterns) from this sample and from the sample with lateral QDs were studied in magnetic field as well. They all split into four lines in Faraday geometry and in two lines in Voigt. The estimated exchange interaction splitting values were found very similar: a few tens of μeV. These consistent results confirmed that the observed magneto-optical properties are the intrinsic properties of pyramidal InGaAs/GaAs QDs.

6.4 Summary

Magneto-optical properties of lateral and central QDs were studied. The ability of the set-up to probe properties at arbitrary QD and magnetic field orientations allowed an independent identification of lateral QDs. Their presence in the lateral quantum wires was confirmed Zeeman splitting and the diamagnetic shift coefficient dependence on a QD orientation. Moreover, highly symmetric central QDs were studied. Unusual Zeeman splitting of an exciton transition to four and two spectral

lines was observed when QD growth plane was oriented perpendicular and parallel to the magnetic field, respectively. The result is in good agreement with some previous experimental and theoretical studies of QDs with C_{3V} symmetry, and confirms the observed splitting as an intrinsic property of pyramidal QDs.

Bibliography

[1] K. J. Nash, M. S. Skolnick, P. A. Claxton, and J. S. Roberts, Phys. Rev. B 39, 10943 (1989).

[2] M. Bayer, S. N. Walck, T. L. Reinecke, and A. Forchel, Phys. Rev. B 57, 6584 (1998).

[3] H. W. van Kesteren, E. C. Cosman, W. A. J. A. van der Poel, and C. T. Foxon, Phys. Rev. B 41, 5283 (1990).

[4] M. Bayer, G. Ortner, O. Stern, A. Kuther, A. A. Gorbunov, A. Forchel, P. Hawrylak, S. Fafard, K. Hinzer, T. L. Reinecke, S. N. Walck, J. P. Reithmaier, F. Klopf, and F. Schafer, Phys. Rev. B 65, 195315 (2002).

[5] G. Sallen, et al., Phys. Rev. Lett. 107, 166604 (2011).

[6] M. V. Durnev, et al., Phys. Rev. B 87, 085315 (2013).

[7] V. D. Kulakovskii, G. Bacher, R. Weigand, T. Kümmell, A. Forchel, E. Borovitskaya, K. Leonardi, and D. Hommel, Phys. Rev. Lett. 82, 1780 (1999).

[8] R. M. Stevenson, R. J. Young, P. See, D. G. Gevaux, K. Cooper, P. Atkinson, I. Farrer, D. A. Ritchie, and A. J. Shields, Phys. Rev. B 73, 033306 (2006).

[9] R. J. Young, thesis 'Controlling the fine structure splitting in single InAs quantum dots' (2006).

[10] N. A. J. M. Kleemans, J. van Bree, M. Bozkurt, P. J. van Veldhoven, P. A. Nouwens, R. Nötzel, A. Y. Silov, P. M. Koenraad, and M. E. Flatté, Phys. Rev. B 79, 045311 (2009).

[11] D. Kim, W. Sheng, P. J. Poole, D. Dalacu, J. Lefebvre, J. Lapointe, M. E. Reimer, G. C. Aers, and R. L. Williams, Phys. Rev. B 79, 045310 (2009).

[12] M. Bayer, A. Kuther, A. Forchel, A. Gorbunov, V. B. Timofeev, F. Schafer, J. P. Reithmaier, T. L. Reinecke, and S. N. Walck, Phys. Rev. Lett. 82, 1748 (1999).

Conclusions and outlook

The aim of this work was to develop a bright and efficient source of single and polarization-entangled photons on demand and study the associated physical processes. Site-controlled InGaAs quantum dots (QDs) grown in 7.5 μm pitch tetrahedrons etched in (111)B oriented GaAs substrates were selected as possible candidates. It was shown that choosing GaAs as QD confinement barrier material instead of the previously widely studied AlGaAs substantially affects the structural and optical properties of the QDs which were studied in detail.

A detailed study of the whole spectra composed of the photoluminescence of a number of InGaAs nanostructures self-formed in each pyramidal recess revealed that more than one QD-like feature exists, contrary to what has been previously accepted. The presence of previously over-looked three QDs (lateral QDs) close to the top corners of the recess was shown by several methods: side-view photoluminescence, fine-structure splitting characterization and magneto-optical photoluminescence. The finding was not only interesting fundamentally but helped to correct some previous imprecise interpretations of the experimental data.

The study of the main central QD showed for the first time that InGaAs QDs confined by GaAs have a characteristic feature of the excitonic pattern never observed from the counterpart QDs confined by AlGaAs: a biexciton present at higher energy than the exciton. The presence of at least two types of the over-all excitonic patterns distinguished by the energetic order of neutral and charged transitions was identified. The particular pattern (which was found as a reliable fingerprint of highly symmetric QDs emitting entangled photons) was studied by photon correlation spectroscopy. Not only was single photon emission proven, but various multiexcitonic transitions (e.g., positively charged biexciton, ground and excited charged excitons) were named for the first time.

Correlation measurements helped to point out some currently present issues related to the population of a QD by charge carriers. Re-capture of carriers from a QD vicinity in a pulsed excitation mode was suggested as the main source of the reduced single photon emission quality.

The large majority of QDs were found to be highly symmetric when characterized by the value of the fine-structure splitting, which usually was lower

than a few microelectronvolts. The high symmetry was confirmed by the detection of polarization-entangled photons for the first time from any epitaxially grown site-controlled QD family. The highest fidelity of the expected maximally entangled state was found to be 0.72. It was shown that the best results in the terms of fidelity values and the density of entangled photon emitters was achieved from the samples exposed to unsymmetrical dimethylhydrazine (the precursor of nitrogen) which possibly acts as a surfactant improving the alloy uniformity. In these samples, areas containing at least 15% of entangled photon emitters were found: the density much higher than in any other QD system. The samples grown without exploiting the surfactant effect still contained QDs emitting entangled photons, however, the density and fidelity values were found to be lower.

Moreover, the optical response to magnetic field of QD features was studied in Cambridge Cavendish Laboratory, again for the first time. Unusual properties (e.g., splitting to four lines when QD growth plane is perpendicular to the crossing magnetic field) peculiar to QDs with the rotational symmetry C_{3V} were found, supporting some experimental observations in other studies, and better clarifying the involved physics.

The results of this work show that pyramidal QDs are potential units of quantum information processing devices. However, the practical realization of such integrated photonic systems would require very high standards of all the composing elements. Future goals should involve tasks that would help pyramidal QDs to meet these standards. As a large number of QDs most likely will be present on a single chip, improving emission energy uniformity and spectral purity characteristics are the first goals. While the nature of the pyramidal QD system offers uniformity of a few meV, achieving a nearly ideal uniformity only by optimizing the epitaxial growth and processing would be a very difficult task (if not impossible). Clearly some kind of tuning strategy is required. Our group and the author of this thesis have already started to investigate these possibilities: for example the emission energy of pyramidal QDs integrated on a piezoelectric crystal was tuned through the strain in the range of a few meV during our initial attempts. By applying such tuning strategy locally, each QD on a sample could be tuned to the same energy. Improved spectral purity most likely should be achieved by optimizing growth and processing

conditions. While resonant or quasi-resonant optical excitation could solve spectral broadening problems, this QD population method is not optimal and difficult to implement if the array of QDs is densely packed. Electric injection should be used instead. This is one of the ongoing and future work programs. The final goal is to develop a procedure which would enable placing electrodes on individual pyramids. Electric gates would enable at least two functions: electric injection and (or) manipulation of excitonic wavefunctions (particularly the fine-structure splitting of exciton) with locally applied electric field.

All this achieved, a major step towards an effective quantum information device would have been made.

Appendix

Epitaxial layers and growth conditions

AlGaAs barriers:

Layer	Material	Thickness [nm]	Temperature [^{o}C]	V/III ratio
Buffer	GaAs	190	770	600
Etch stop ramp	$Al_{0.4\rightarrow0.8}Ga_{0.6\rightarrow0.2}As$	45	800	800
Etch stop layer	$Al_{0.8}Ga_{0.2}As$	90	800	800
Barrier 2	$Al_{0.55}Ga_{0.45}As$	85	730	750
Barrier 1	$Al_{0.3}Ga_{0.7}As$	120	730	750
QD	The list below.			
Barrier1	$Al_{0.3}Ga_{0.7}As$	70	730	750
Barrier 2	$Al_{0.55}Ga_{0.45}As$	160	730	750
Cap	GaAs	1	730	750

GaAs barriers:

Layer	Material	Thickness [nm]	Temperature [^{o}C]	V/III ratio
Buffer	GaAs	230	770	600
Etch stop ramp	$Al_{0.3\rightarrow0.75}Ga_{0.7\rightarrow0.25}As$	45	800	800
Etch stop layer	$Al_{0.75}Ga_{0.25}As$	90	800	800
Barrier 2	$Al_{0.55}Ga_{0.45}As$	150	730	750
Barrier 1	GaAs	100	730	750
QD	The list below.			
Barrier1	GaAs	70	730	750
Barrier 2	$Al_{0.55}Ga_{0.45}As$	150	730	750
Cap	GaAs	1	730	750

The list of the studied samples and growth properties and conditions of a QD layer.

Within AlGaAs barriers:

Text ref. S#	**Material**	**Thickness [nm]**	**Temperature [^{o}C]**	**Database ref. #**
1	$In_{0.25}Ga_{0.75}As$	0.5	730	A1378

Within GaAs barriers:

Text ref. S#	**Material**	**Thickness [nm]**	**Temperature [^{o}C]**	**Database ref. #**
2	$In_{0.25}Ga_{0.75}As(N)$	1.2	655	A0770
3	$In_{0.25}Ga_{0.75}As$	0.5	730	A0128
4	$In_{0.15}Ga_{0.85}As$	0.5	730	A0102
5	$In_{0.25}Ga_{0.75}As$	0.5	730	A0530
6	$In_{0.35}Ga_{0.65}As$	0.5	730	A0147
7	$In_{0.45}Ga_{0.55}As$	0.5	730	A0167
8	$In_{0.55}Ga_{0.45}As$	0.5	730	A0178
9	$In_{0.65}Ga_{0.35}As$	0.5	730	A0190
10	$In_{0.25}Ga_{0.75}As$	0.5	730	A0293
11	$In_{0.25}Ga_{0.75}As$	1.0	730	A0364
12	$In_{0.25}Ga_{0.75}As$	1.0	730	A1012
13	$In_{0.25}Ga_{0.75}As$	0.62	730	A1096
14	$In_{0.25}Ga_{0.75}As$	0.57	730	A1175
15	$In_{0.25}Ga_{0.75}As$	0.53	730	A1186
16	$In_{0.25}Ga_{0.75}As$	0.5	730	A1187
17	$In_{0.25}Ga_{0.75}As$	0.45	730	A1199
18	$In_{0.25}Ga_{0.75}As$	0.8	730	A1208
19	$In_{0.25}Ga_{0.75}As$	1.2	730	A1224
20	$In_{0.25}Ga_{0.75}As(N)$	0.5	730	A0366
21	$In_{0.25}Ga_{0.75}As(N)$	0.5	730	A0448
22	$In_{0.25}Ga_{0.75}As(N)$	0.5	730	A0474
23	$In_{0.25}Ga_{0.75}As$	0.5	700	A0536
24	$In_{0.25}Ga_{0.75}As$	0.5	670	A0537
25	$In_{0.25}Ga_{0.75}As$	0.5	640	A0538
26	$In_{0.25}Ga_{0.75}As(N)$	0.85	730	A1008
27	$In_{0.25}Ga_{0.75}As(N)$	0.75	730	A1047